Doctoral Dissertation

博士論文

Cryogenic measurements of the absorption coefficient of CdZnTe as a candidate material for an immersion grating

（イマージョングレーティング候補材料 CdZnTe の極低温吸収係数の測定）

A Dissertation Submitted for the Degree of Doctor of Philosophy

December 2020

令和 2 年 12 月博士（理学）申請

Department of Physics, Graduate School of Science,
The University of Tokyo
東京大学大学院理学系研究科
物理学専攻

Hiroshi Maeshima
前嶋　宏志

Abstract

In this thesis, we measure the absorption coefficient of CdZnTe with different resistivities at 5–20 μm at 8.5–300 K to study the factors causing absorption in CdZnTe and to reveal if CdZnTe is suitable for cryogenic immersion gratings.

High dispersion spectroscopy in the mid-infrared wavelength range (λ =10–18 μm) is expected to provide chemical and kinematic information on astronomical objects. Although this wavelength range contains valuable information, observation on the ground is difficult due to severe atmospheric absorption. Therefore, observations from space are needed for high-resolution spectroscopy in the mid-infrared wavelength.

A high dispersion spectrograph in the mid-infrared wavelength (SMI/HR; 10–18 μm , $R = \lambda/\Delta\lambda = 29,000$) is planned to be on-board on SPICA (SPace Infrared telescope for Cosmology and Astrophysics). SPICA is an international infrared astronomical satellite mission[*1].

A conventional grating with a size of 290 mm is needed to achieve the required resolution. However, such a large grating is hard to be installed on a satellite instrument. To reduce the size of the grating, a 10–18 μm immersion grating (IG) operating at $T = 4.8$ K for SPICA SMI/HR has been under development. An IG is a diffraction grating immersed with a high-refractive-index (n) medium. Since light passes through the medium, an IG is downsized to $1/n$ in length L compared to a conventional grating (L: 290 $\rightarrow$ 110 mm for CdZnTe case).

An IG material is required to have a low absorption coefficient of $\alpha < 0.01$ cm^{-1}. Previous studies revealed that high-resistivity CdZnTe meets the absorption coefficient requirement for the IG at room temperature (Kaji et al. 2014; Sarugaku et al. 2017). On the other hand, low-resistivity CdZnTe, the availability of which is higher than that of high-resistivity one, does not meet the IG absorption coefficient requirement at room temperature. The absorption of the low-resistivity CdZnTe is considered to be due to free carriers. Therefore, at cryogenic temperature, the absorption coefficient of low-resistivity CdZnTe may decrease due to carrier freeze-out. Thus, not only high-resistivity but also low-resistivity CdZnTe may be candidate materials for the cryogenic IG. The absorption coefficient of CdZnTe has not been measured at cryogenic temperature, although it was measured at room temperature. Therefore, what causes absorption in cryogenic CdZnTe at 10–18 μm has not been revealed, and there is no guideline on how to tune CdZnTe properties suitable for the cryogenic IG.

[*1] SPICA was canceled in 2020.

The purpose of this thesis is to determine whether CdZnTe is suitable for cryogenic IG material and to determine what causes the mid-infrared absorption in CdZnTe. To measure the absorption coefficient of these IG candidate materials, we need to measure the transmittance of the CdZnTe substrates with different thickness at cryogenic temperature. Also, to research the resistivity dependence of the absorption, we need CdZnTe with different resistivity. Therefore, we prepare four CdZnTe samples: with two different thickness ($\sim t1, t10$ mm) with two different resistivities ($\sim 10^2$, $> 10^{10}$ Ωcm). To check the absorption coefficient at IG operational temperature, samples are required to be cooled down to cryogenic temperature (4.8 K). To check whether materials meet the IG requirement ($\alpha < 0.01$ cm^{-1}), the uncertainty of absorption coefficient is required to be $\Delta\alpha < 3 \times 10^{-3}$ cm^{-1}.

Infrared transmittance is usually measured by a Fourier Transform Spectrometer (FTS) with an uncollimated beam. However, transmittance measurement of CdZnTe with a typical FTS yields large systematic errors because such a thick and high-refractive-index sample extends the optical length of the uncollimated beam and displaces the focus position from the detector position. Therefore, this defocus error prevents accurate absorption coefficient measurement. To correct the defocus error, we conduct two types of experiments aiming at evaluating absorption coefficient with high precision ($\Delta\alpha < 3 \times 10^{-3}$ cm^{-1}).

One of the experiments is (1) the transmittance measurement with an FTS and a cryostat cooled with liquid helium. We can obtain wavenumber dependence of the absorption coefficient with this experiment, although installing a thick and high-refractive-index CdZnTe sample provides systematic uncertainty due to the defocus.

In experiment (1), the lowest temperature ($T_{\rm min} = 8.5 \pm 0.5$ K) is achieved lower than the previous study (29 K;Kaji et al. 2016). The measured 10–18 μm absorption coefficient of the low-resistivity CdZnTe is α =0.4–0.6 cm^{-1} at 300 K and becomes larger (α =0.5–1.4 cm^{-1}) at 8.5 K. On the other hand, the absorption coefficient of the high-resistivity CdZnTe is < 0.1 cm^{-1} both at 300 K and at 8.5 K.

The other experiment is (2) the transmittance measurement with an originally developed system of a collimated globar lamp beam, four bandpass filters (6.45, 10.6, 11.6 and 15.1 μm) and a cryostat with a Gifford-Mcmahon (GM) type cooler. This system measures the absolute absorption coefficient without defocusing effect, although the wavelength is limited to the four bands.

In experiment (2), the lowest temperature ($T_{\rm min} = 8.6 \pm 0.1$ K) is achieved lower than the previous study (29 K;Kaji et al. 2016). The absorption coefficient of the low-resistivity CdZnTe is α =0.3–0.9 cm^{-1} and becomes larger at cryogenic temperature. On the other hand, we obtain the upper limit of the absorption coefficient of high-resistivity CdZnTe ($\alpha < 0.11$ cm^{-1}).

By correcting (1) the result of the FTS experiment with (2) that of the collimated beam experiment, we obtain wavenumber dependence of the absorption coefficient of the low-resistivity CdZnTe without the defocus error. We can estimate the absorption coefficients at 4.8 K is the same those at 8.5 K since the temperature dependence of the absorption coefficient is negligible

at < 50 K. The 10–18 μm absorption coefficient of the low-resistivity CdZnTe is α =0.4–0.6 cm^{-1} at 300 K and α =0.5–1.3 cm^{-1} at 8.5 K. From our results, the low-resistivity CdZnTe is not suitable as an IG material even at cryogenic temperature due to its large absorption coefficient. At 10–18 μm, the statistical uncertainty of the corrected absorption coefficient is $\Delta\alpha$ =0.01–0.02 cm^{-1}, and the systematic uncertainty due to the calculation method is $\Delta\alpha_{\rm calc}$ = 0.03 cm^{-1}. This uncertainty is improved from the FTS measurements (statistical uncertainty: $\Delta\alpha_{\rm stat}$ = 0.03 cm^{-1}+ uncertainty due to the defocus: $\Delta\alpha_{\rm defocus} \sim 0.06$ cm^{-1} + systematic uncertainty due to the calculation method $\alpha_{\rm calc} = 0.03$ cm^{-1}).

To determine factors causing absorption in the low-resistivity CdZnTe, we fit the measured results with a model of absorption coefficient including intra-valence band absorption, inter-valence band absorption, and trapped-hole absorption. The absorption coefficient is well-fitted with the model with physical parameters: the energy separation between acceptor level and top level of the valence band $E_a = 63 \pm 1$ meV, the effective mass ratio of heavy and light holes m_h/m_l =6–8, the acceptor density $N_A = (4.1 \pm 0.7) \times 10^{14}$ cm^{-3}. The parameters are consistent with those from previous studies or predicted values. Our result suggests that the dominant absorption term in the low-resistivity CdZnTe is the inter-valence band absorption due to free-holes at 150–300 K and the absorption due to trapped-holes at < 50 K.

The upper limit of the corrected absorption coefficient of the high-resistivity CdZnTe at a broad wavelength range is estimated from the results of the two experiments. We obtain the upper limit of 10–18 μm absorption coefficient of the high-resistivity CdZnTe ($\alpha < 0.11$ cm^{-1} at 300 K and $\alpha < 0.16$ cm^{-1} at 8.5 K). We confirm that the absorption coefficient of the high-resistivity CdZnTe is lower than those of the low-resistivity CdZnTe ($\alpha > 0.4$ cm^{-1}) at 300 K and at 8.5 K.

We can estimate the required resistivity at 300 K to meet the IG absorption coefficient requirement ($\alpha < 0.01$ cm^{-1}) at cryogenic temperature. The resistivity at 300 K is proportional to free carrier density at 300 K, which is roughly the same as trapped-carrier density at $T < 50$ K. The absorption is dominated by the trapped-carrier absorption in low/medium-resistivity CdZnTe at cryogenic temperature since other possible absorption factors are $\alpha \leq 0.0025$ cm^{-1}. We estimate the required resistivity as $\rho \geq 3 \times 10^4$ Ωcm from our result. Therefore, the high-resistivity CdZnTe ($> 10^{10}$ Ωcm) is expected to be suitable for the cryogenic IG since it meets this resistivity requirement ($\rho \geq 3 \times 10^4$ Ωcm).

In this thesis, we measured absorption coefficient of low/high-resistivity CdZnTe at 5–20 μm at 8.5–300 K to study the factors causing absorption in CdZnTe and to reveal whether CdZnTe is suitable for the cryogenic IG. Our results show that the low-resistivity CdZnTe is not suitable for the cryogenic IG material because of its large absorption ($\alpha > 0.4$ cm^{-1}) and that the dominant absorption factors of the low-resistivity CdZnTe are absorption due to free holes at 300 K and absorption due to holes trapped at acceptor states at < 50 K. For the high-resistivity CdZnTe, we obtain only the upper limit of the absorption coefficient ($\alpha < 0.16$ cm^{-1}). However, the high-resistivity CdZnTe is expected to meet the absorption requirement at cryogenic temperature

because it meets the room temperature resistivity requirement ($\rho \geq 3 \times 10^4$ Ωcm) estimated to meet the required absorption coefficient for the cryogenic IG.

Contents

§1

Introduction

In this section, we describe the introduction of our research. Section 1.1 describes the benefit of high-dispersion spectroscopy in infrared astronomy. We describe the next-generation space telescope mission SPICA in section 1.2. In section 1.3, we discuss the reasons why we need an immersion grating, a new type of grating suitable for the spaceborne application. Section 1.4 describes the development of an immersion grating for SPCIA and the problem. We describe the purpose of our research in section 1.5.

1.1 High dispersion spectroscopy in infrared astronomy

High dispersion spectroscopy ($R \equiv \lambda/\Delta\lambda \sim 30,000$) in the mid-infrared wavelength range (about 10–20 μm) is expected to provide molecular-line information that has been buried in complex line forests so far. For example, Figure 1.1 shows synthetic emission spectra of several molecules in a T Tauri disk model (Greenwood et al. submitted). A T Tauri disk is a gas and dust disk around a T Tauri star, which is a low-mass pre-main sequence star. Line complexes are fully blended in $R = 600$ case, which is the resolution of Spitzer Space Telescope launched in 2006 (Houck et al. 2004). Spectroscopic observation with $R \sim 2,800$ will be realized by Mid-Infrared Instrument (MIRI) mounted on James Webb Space Telescope (JWST), which will be launched in 2021 (Gardner et al. 2006). For the $R = 2,800$ cases, several features of line complexes can be deblended, although individual lines cannot be resolved. High-resolution spectroscopy ($R = \lambda/\Delta\lambda = 28,000$) can disentangle most of the line complex features and is expected to provide chemical information in the disk (e.g., Nomura et al. 2019).

If molecular lines are velocity-resolved, kinematic information can be obtained. Figure 1.2 shows a calculated velocity profile of H_2O line at 17.75 μm from a T Tauri disk model (Notsu et al. 2016). An H_2O snowline is the outer edge position of H_2O ice sublimation by central star heating and affect the planet formation theories (Hayashi et al. 1985). The line of 17.75 μm H_2O is a suitable line for tracing snowlines since the line is optically thin due to its small Einstein A coefficient (Notsu et al. 2016). The double-shoulder shape shown in Figure 1.2 (A) suggests that the snowline exists in a position where the Kepler rotation velocity is equivalent

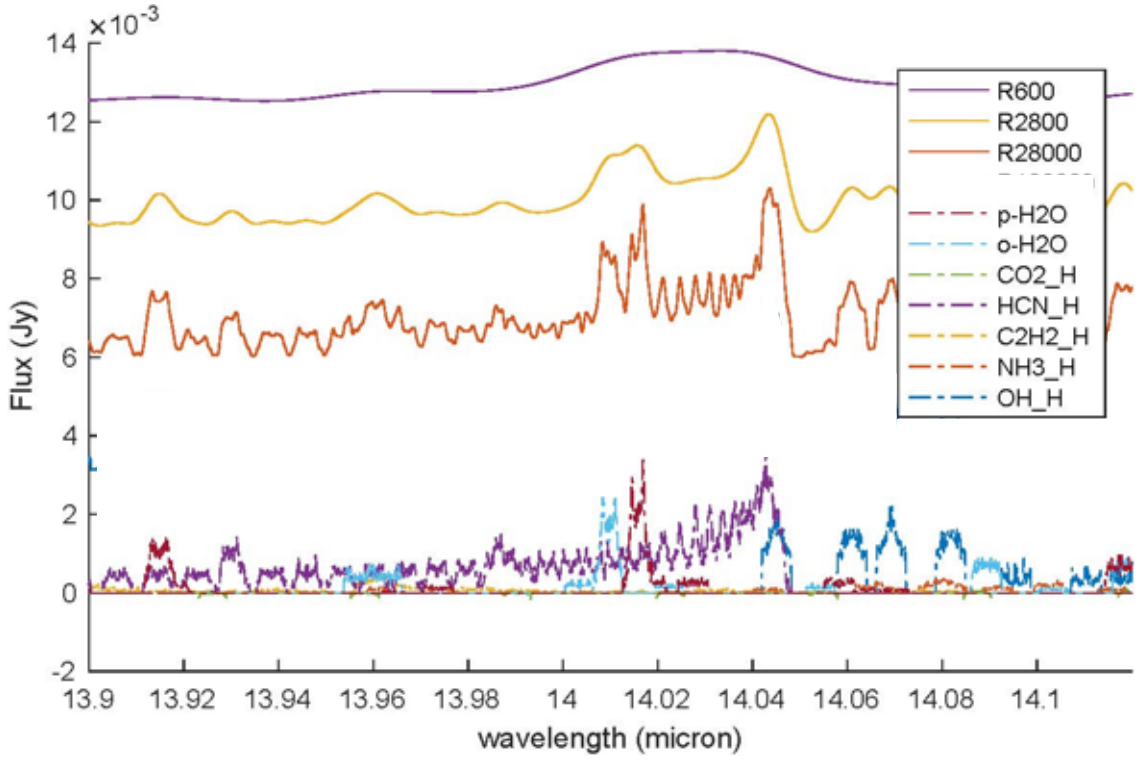

Figure. 1.1 Synthetic emission spectra of an T Tauri disk model (Greenwood et al. submitted; partially changed). The purple, yellow and orange lines show synthetic spectra with resolution $R = 600, 2800$ and 28000, respectively. The other lines show the spectra of individual molecules. The "_H" in the legend means rotational-vibrational data taken from HITRAN database (Rothman et al. 2009).

to ~ 20 km/s (~ 2 au). As shown in Figure 1.2 (B), we cannot resolve this double peak shape with medium resolution ($R \sim 10,000$). High-resolution spectroscopy ($R \sim 30,000$) is required to detect the snowline feature. Locating the H_2O snowline directly is difficult because of insufficient spatial resolution (e.g., Honda et al. 2016). Therefore, high-resolution spectroscopy is the only promising method for locating the H_2O snowline in the near future.

The mid-infrared wavelength range includes ranges where ground-based observation is difficult due to large atmospheric absorption. Figure 1.3 shows the atmospheric transmission calculated with ATRAN software (Sarugaku et al. 2012; Lord 1992). The strong absorption band at ~ 15 μm remains even at the altitude of the Stratospheric Observatory for Infrared Astronomy (SOFIA; Young et al. 2012), which is an aircraft carrying a 2.7 m telescope. Therefore, an astronomical satellite is needed to observe objects in the mid-infrared wavelength.

Astronomical satellites with high-sensitivity and high-dispersion ($R \sim 30,000$) mid-infrared spectrometer has never been realized. Spitzer Space Telescope launched in 2003 was equipped with the Infrared Spectrograph (IRS) Short-High (SH) mode with a resolution of $R \sim 600$ (Houck et al. 2004). James Webb Space Telescope (JWST), which will be launched in 2021, has the Mid-Infrared Instrument (MIRI) with a resolution of $R \sim 3,000$ (Gardner et al. 2006), not reaching $R \sim 30,000$.

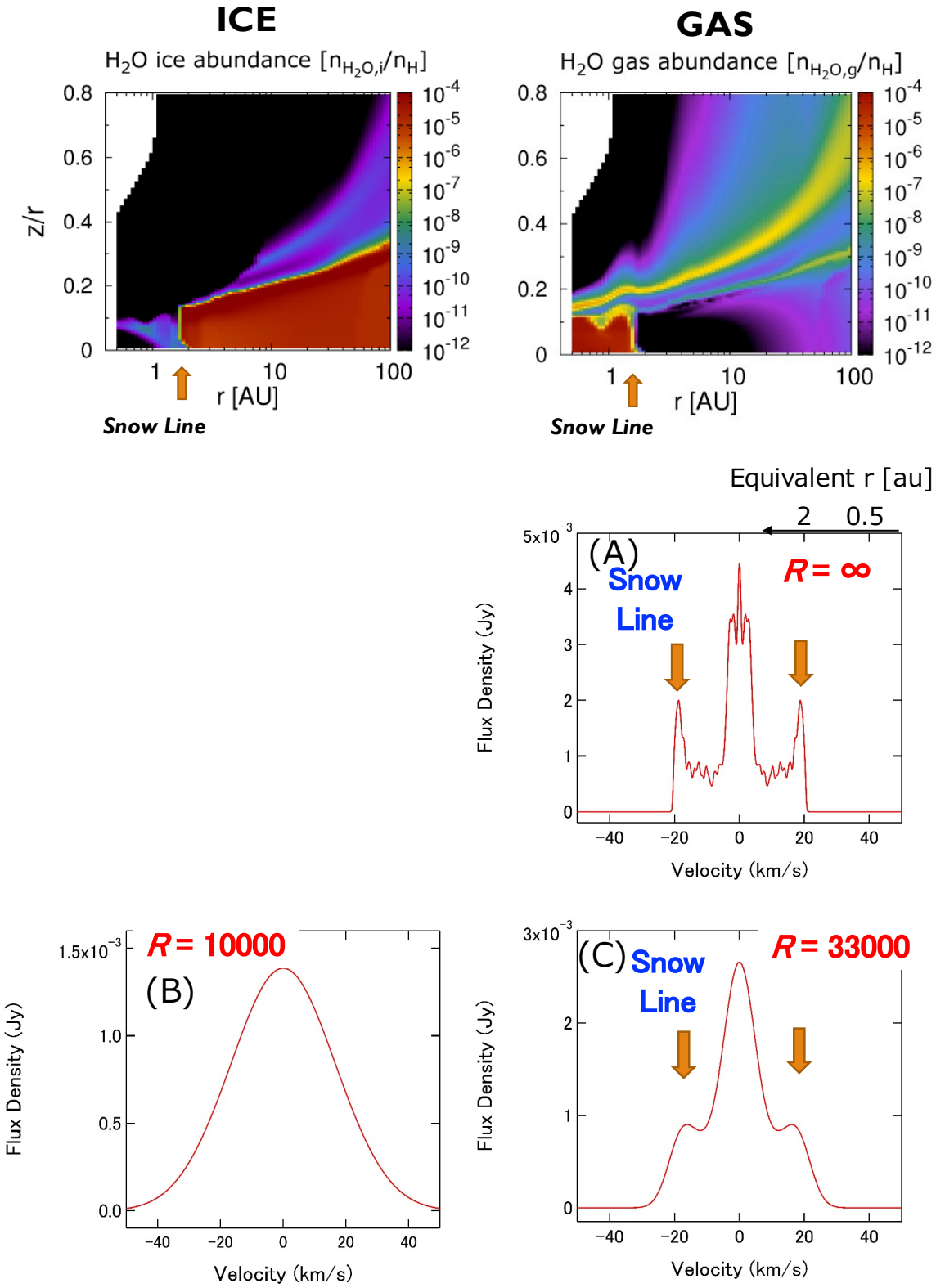

Figure. 1.2 Snow line simulations for a T Tauri star (Notsu et al. 2016; Nakagawa in prep, partial change). (Top) Simulated H_2O gas and ice abundance distribution in a model of a disk around a T Tauri star. (Bottom) velocity profile of the 17.75μm H_2O line of the disk model with infinite S/N (signal to noise) ratio with each resolution case: (A) $R = \infty$ case. (B) $R = 10,000$ case. (C) $R = 33,000$ case. The flux density around 0 km/s comes from vapor gas on the disk surface.

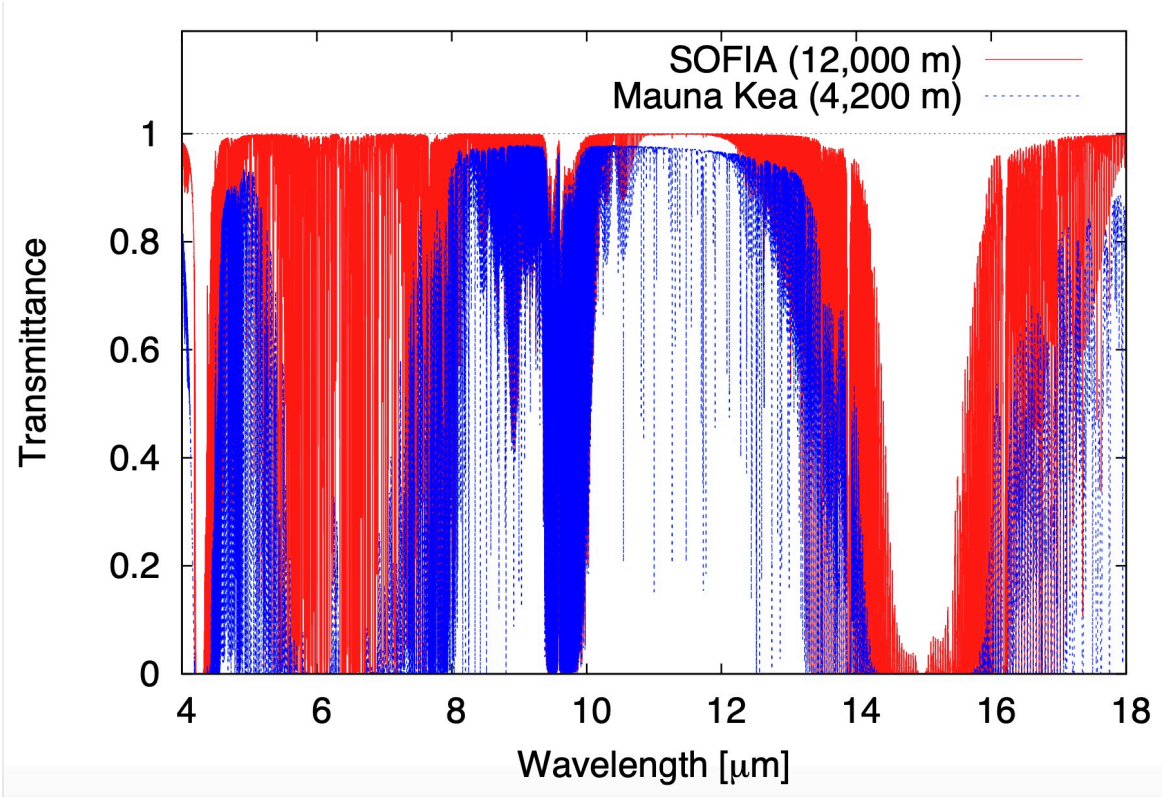

Figure. 1.3 Calculated atmospheric transmittance in the mid-infrared region at Mauna Kea Observatories altitude (4,200m) and at the SOFIA altitude(12,000 m)(Sarugaku et al. 2012; Lord 1992).

1.2 SPICA

SPICA[*1] (SPace Infrared telescope for Cosmology and Astrophysics; Figure 1.4) is international mission developed jointly by Japan and Europe (Roelfsema et al. 2020). The scientific purpose of this space observatory is to unravel "the process that enriched the universe with metal and dust and led to the formation of habitable worlds" by observing "metal and dust enrichment through galaxy evolution" and "planetary system formation of habitable systems." With an actively cooled 2.5m-diameter telescope, SPICA is planned to be equipped with three instruments (SAFARI – SpicA FAR-infrared Instrument, SMI – SPICA Mid-Infrared Instrument and B-BOP – magnetic field (B) explorer with BOlometric Polarimeter). Figure 1.5 shows the comparison of radiant intensity from telescopes and intensity from the astronomical backgrounds. To reduce thermal noise from the telescope below the background at 10–350 μm, SPICA is cooled to below 8 K.

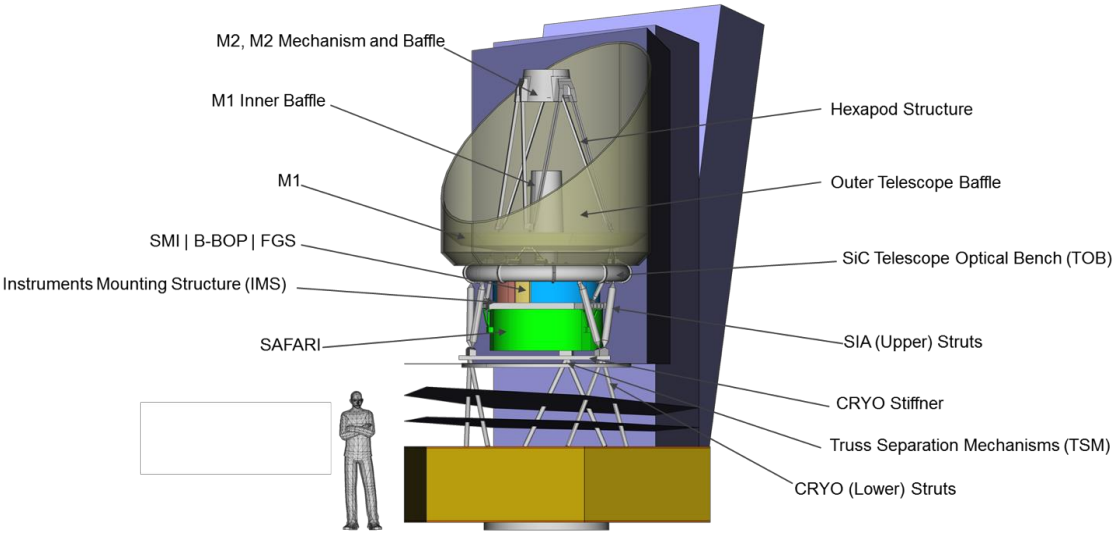

Figure. 1.4 The configuration of SPICA (Archer et al. 2020). SPICA has a 2.5 m primary mirror. The total mass is about 3,500 kg. The telescope is cooled to below 8 K with mechanical cryocoolers.

SMI is an instrument that can perform spectroscopy and imaging with high sensitivity at 10–38 μm (Wada et al. 2020), being developed primarily by Japanese universities and ISAS (Institute of Space and Astronautical Science). SMI has four channels, SMI/CAM, /LR, /MR and /HR. Table 1.2 summarizes the specification of the four channels. SMI/CAM was $10' \times 12'$ slit viewer camera, SMI/LR is the low-resolution (R =60–160, 17–36 μm), SMI/MR is the mid-resolution (R =1,400–2,600, 18–36 μm) and SMI/HR is the high-resolution spectrometer ($R = 29,000$, 10–18 μm). Especially HR channel has a ten-times higher resolution than JWST ($R \sim 3,000$)

[*1] SPICA was canceled in 2020 on financial grounds.

Table. 1.1 Specifications of SPICA (Roelfsema et al. 2018).

Launch	target year	2027–2028
Spacecraft	mass	3,500 kg
	height	5.3 m
Instruments		·Mid-infrared instrument (SMI; 10–36 μm)
		·Far-infrared instrument (SAFARI; 34–230 μm)
		·magnetic field explorer
		with BOlometric Polarimeter (B-BOP; 100, 200, 350 μm)
Telescope	Aperture	2.5 m
	Temperature	< 8 K
Cooling system		Cryocoolers and radiative cooling

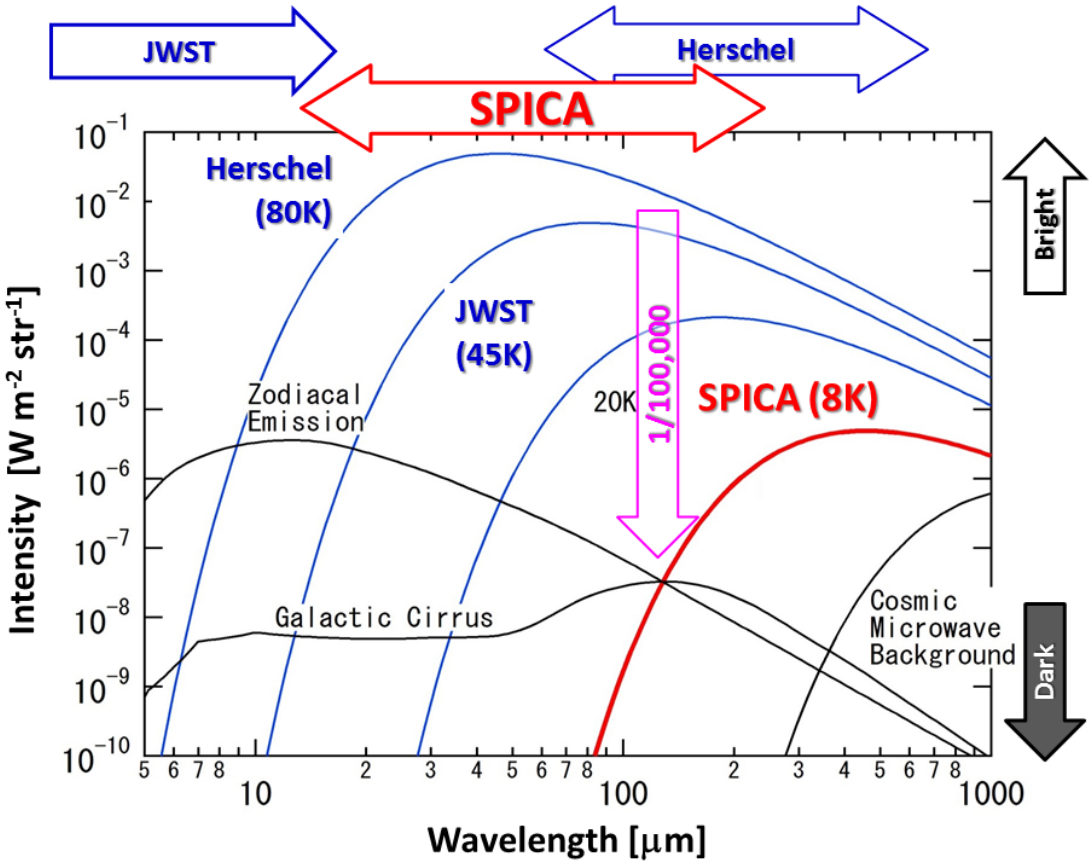

Figure. 1.5 Telescope temperatures and astronomical emissions (`https://www.ir.isas.jaxa.jp/SPICA/SPICA_HP/feature-en.html`). Herschel was an infrared space observatory of ESA launched on 2009 (Pilbratt et al. 2010).

to be launched in recent years.

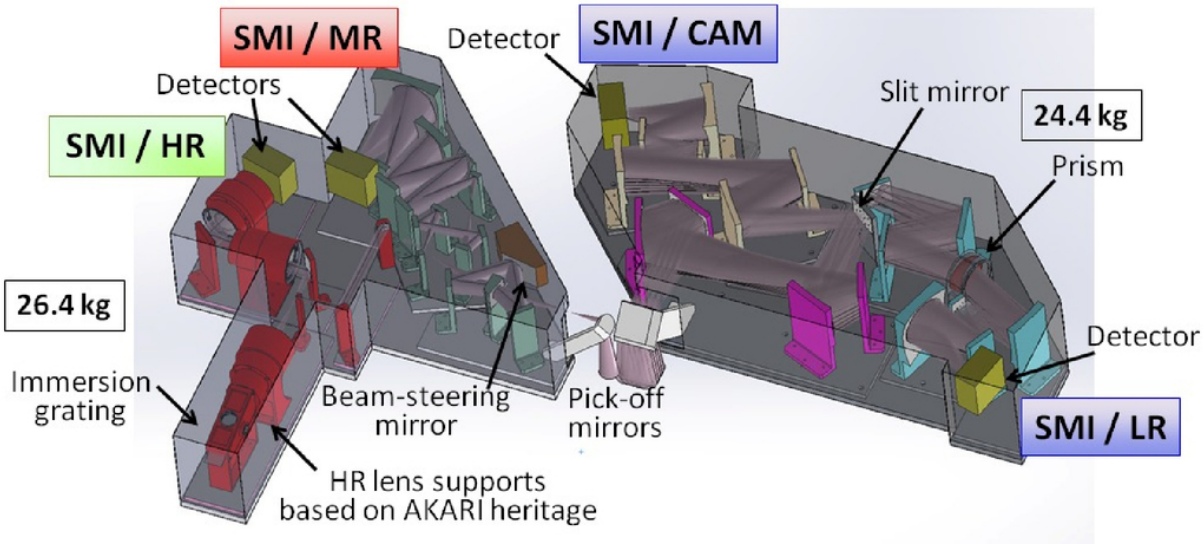

Figure. 1.6 SMI design (Kaneda et al. 2018). The physical size of SMI/MR-HR part is $1040 \times 790 \times 230$ mm^3 AKARI written in the figure was a Japanese satellite launched in 2006 (Murakami et al. 2007).

Table. 1.2 SMI specification (Wada et al. 2020).

channel	LR	CAM	MR	HR
wavelength [μm]	17–36	34	18–36	10–18
spectral resolution R	60–160	5	1400–2600	$29,000^a$
Point source sensitivity (5σ/1hour)				
Continuum [μJy]	23	11	200	0.7
Line [10^{-20} W/m^2]	5		1.9	0.5

a: designed for $\lambda 20$ μm diffraction limited point spread function.

1.3 Immersion grating

Here we describe the size problem of a conventional grating and what is an immersion grating.

We evaluate the required size of a conventional blazed grating for SMI HR ($R = 29,000$) to check whether it can be installed on SMI. First, we derive the formula of the maximum resolution of a conventional grating. Figure 1.7 shows a schematic view of an optical path through a blazed grating in the Littrow condition, where the incident angle is the same as the blaze angle θ_B. The ideal angular resolution $\Delta\beta_{\rm limit}$ can be determined by a monochromatic diffraction-limit point spread function, which is equivalent to the ratio of wavelength λ and collimated beam diameter ϕ at the pupil:

$$\Delta\beta_{\rm limit} \simeq \frac{\lambda}{\phi}. \tag{1.1}$$

The interference condition can be written as follows:

$$d(\sin\theta_B + \sin\beta) = m\lambda \quad (m = 1, 2, 3...), \tag{1.2}$$

where d is grating pitch, β is exit angle and m is diffraction order. In the Littrow condition, the exit angle is the same as the incident angle ($\beta \simeq \theta_B$). From the interference condition, $\frac{d\beta}{d\lambda}$ can be expressed as

$$\frac{\mathrm{d}\beta}{\mathrm{d}\lambda} = \frac{\lambda\cos\beta}{2\sin\theta_B} \simeq \frac{\lambda}{2\tan\theta_B} \quad (\beta \simeq \theta_B). \tag{1.3}$$

Therefore, the ideal wavelength resolution of a blazed grating $R_{\rm max}$ can be expressed as follows:

$$R_{\rm max} \equiv \frac{\lambda}{\Delta\lambda_{\rm max}} = \lambda\frac{d\beta}{d\lambda}\frac{1}{\Delta\beta_{\rm limit}} = \frac{2\phi\tan\theta_B}{\lambda}. \tag{1.4}$$

The required size of a grating L is derived as

$$L = \phi\tan\theta_B = 290\left(\frac{R_{\rm max}}{29,000}\right)\left(\frac{\lambda}{20\mu\mathrm{m}}\right)[\mathrm{mm}]. \tag{1.5}$$

The required size of grating for $R_{\rm max} = 29,000$ at 20 μm is $L \sim 290$ mm. A blazed grating with $L \sim 290$ mm is hard to mount on SMI-HR part ($1040 \times 790 \times 230$ mm^3, Figure 1.6).

An immersion grating (IG) is an immersed diffraction grating and is filled with a high-refractive-index (n) medium in its optical path. Figure 1.8 shows a schematic view of a conventional blazed grating and an IG. When light enters the medium from a vacuum, the wavelength becomes shorter ($\lambda \to \lambda/n$). By modifying equation 1.4, the maximum spectral resolution $R_{\rm max}$ of an IG can be calculated as follows:

$$R_{\rm max} \equiv \frac{\lambda}{\Delta\lambda_{\rm max}} = \frac{2n\phi\tan\theta_B}{\lambda}. \tag{1.6}$$

Since the resolution is proportional to the refractive index (n), IG can be downsized to $1/n$ in length. For example, to realize $R = 29,000$ spectroscopy at 20 μm, the required size of an IG with $n = 2.7$ (e.g. CdZnTe; Ikeda et al. 2015) is $L \sim 110$ mm . Since the size of SMI-HR part is $1040 \times 790 \times 230$ mm^3 (Figure 1.6), The $1/n$-downsizing of a grating ($L : 290 \to 110$ mm) makes a large impact on the design of a compact optical system on the astronomical satellite.

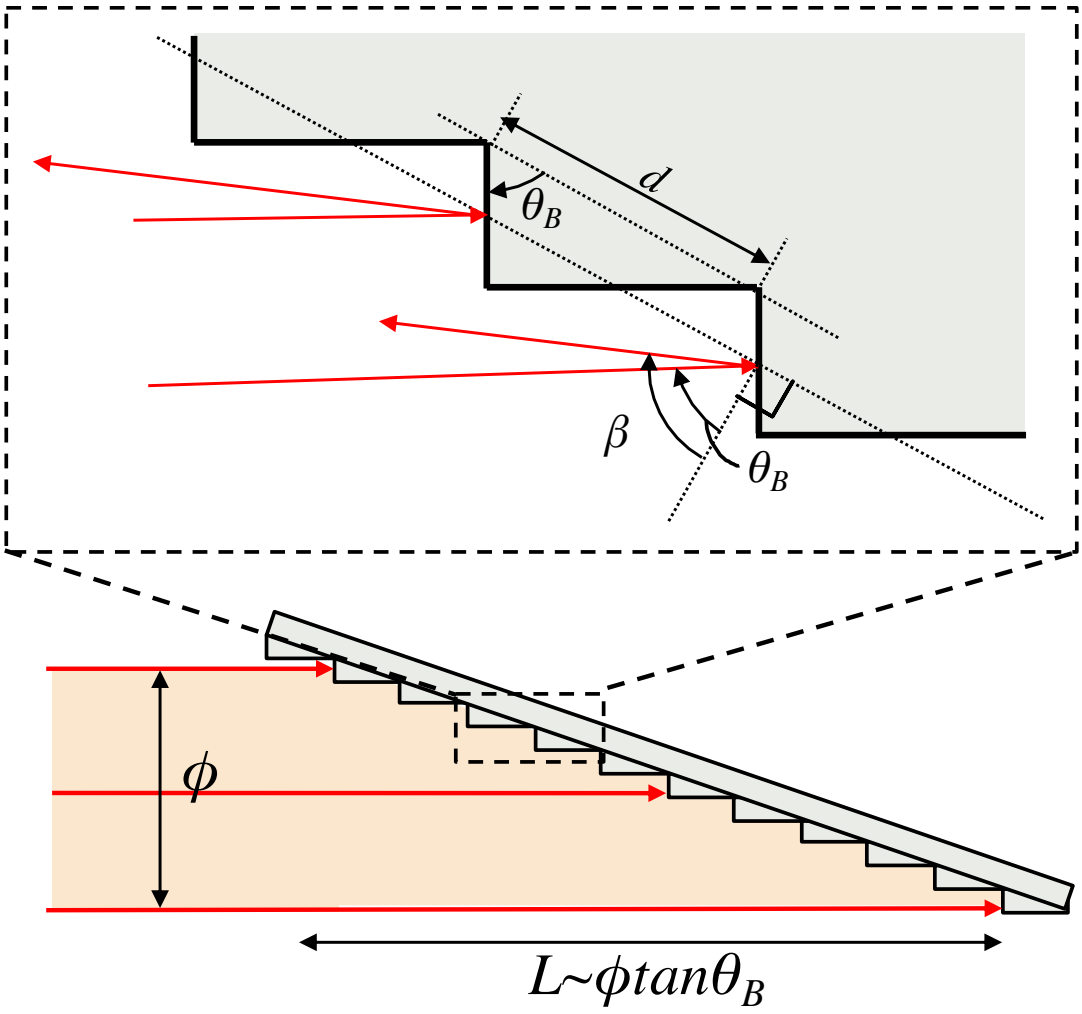

Figure. 1.7 Optical path in a conventional blazed grating in the Littrow condition.

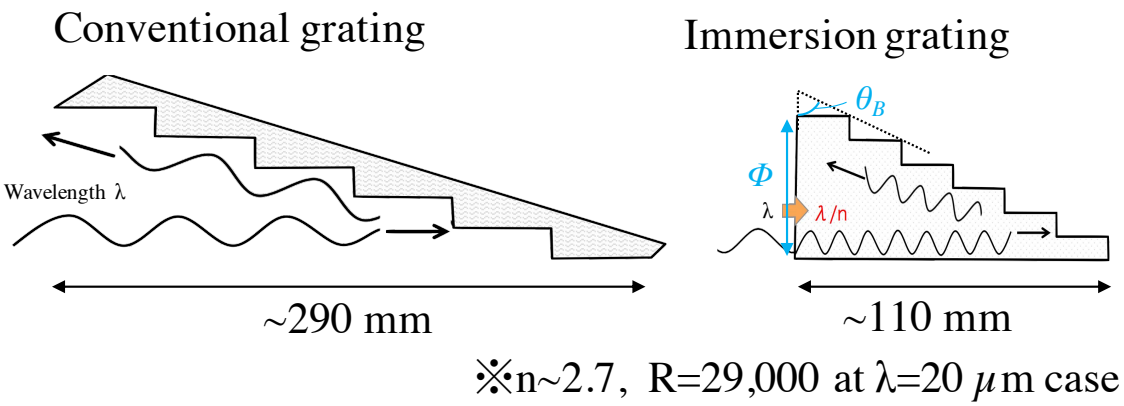

Figure. 1.8 A conventional grating and an immersion grating . The size is derived in the case of $n = 2.7$ and $R = 29,000$ at 20 μm. The blazed angle is denoted by θ_B and the size of the incident beam is denoted by ϕ.

1.4 Development of 10–18 μm IG for SPICA SMI/HR

In this section, we describe the development of the 10–18 μm IG for SPICA.

IGs with various materials have already been developed. At 1.45–2.5 μm, a Si-IG was applied to astronomical observations (Marsh et al. 2007). A Ge-IG (2–11 μm, $n = 4$) and an InP-IG (1.4–8 μm, $n = 3.2$) were developed (Sukegawa et al. 2016; Sukegawa & Okura 2017; Ebizuka et al. 2003). The first light observation of spectrograph with a cryogenic Ge-IG has already been conducted (8–13 μm, $R = 50,000$; Hirahara et al. 2012). Another Ge-IG was demonstrated high efficiency (70–80%) at cryogenic temperature (2–5 μm, $R = 80,000$; Sarugaku et al. 2016). Mid-infrared IGs have also been developed, but they are demonstrated only at room temperature (Ikeda et al. 2015; Sukegawa 2018). On the other hand, spectrograph instruments should be cooled down to cryogenic temperature to reduce the thermal noise from the instrument itself in the case of astronomical observation. Although various IGs have been developed, a cryogenic IG for SPICA SMI/HR has not been realized yet.

To develop the cryogenic IG, we need to select candidate materials. First, we describe the absorption coefficient requirement for IG material. To reduce the absorption loss in a L mm IG to $A_{\rm abs} < 10\%$, the absorption coefficient is required to be

$$\alpha = -\frac{\ln(1 - A_{\rm abs})}{L} < 0.01 \left(\frac{L}{110 \text{ mm}} \right)^{-1} \text{ cm}^{-1} \text{ (at operating temperature)}. \quad (1.7)$$

Therefore, the α requirement for $L = 110$ mm IG for SMI/HR is $\alpha < 0.01$ cm^{-1}.

To select candidate material for the cryogenic 10–18 μm IG, we describe previous room temperature studies by Kaji et al. (2014) and Sarugaku et al. (2017). Kaji et al. (2014) and Sarugaku et al. (2017) researched absorption coefficients of various infrared materials (CdTe, low/high-resistivity CdZnTe, Ge, Si, ZnSe and ZnS) at 295 K. These infrared materials meet the requirements for a candidate material of immersion gratings, such as the high refractive index ($n > 2$), the high homogeneity of the refractive index ($\Delta n < 10^{-4}$), the machinability, the commercial availability of a large crystal and little internal absorption. Figure 1.9 shows the 295 K absorption coefficient of low/high-resistivity CdZnTe measured by Kaji et al. (2014). Kaji et al. (2014) revealed that the high-resistivity CdZnTe meets the absorption coefficient requirement for 10–18 μm IG at room temperature. On the other hand, the low-resistivity CdZnTe, the availability of which is higher than the high-resistivity one, does not meet the requirement. As shown in Figure 1.9, the absorption coefficient of the low-resistivity CdZnTe increases with wavelength at 5–20 μm. This absorption is considered to be due to free-carrier absorption[*2]. If the low-resistivity CdZnTe is cooled down to cryogenic temperature, we expect that free carriers should be frozen-out and that free-carrier absorption becomes smaller than the IG requirement. Therefore, not only the high-resistivity but also the low-resistivity CdZnTe may be candidate material for the cryogenic IG.

[*2] Photon energy is absorbed by a free carrier and scattered by phonons or ionized impurities (Kudo 1996).

Although CdZnTe is the candidate material, the absorption coefficient at the mid-infrared wavelength has not been measured at cryogenic temperature. Kaji et al. (2016) reported the development status of the system of high precision absorption coefficient measurement at low temperatures. The system can cool samples down to 29 K. On the other hand, samples need to be cooled down to ≤ 4.8 K, which is the operating temperature of IG for SPCIA SMI/HR, for our purpose. To research the suitability of materials for cryogenic IG, we need to construct an absorption coefficient measurement system at cryogenic temperature.

In addition to no data of the cryogenic absorption coefficient, what causes absorption in CdZnTe at the mid-infrared wavelength has not been studied. Therefore, we cannot determine what physical parameter should be controlled to make CdZnTe suitable for cryogenic IG material.

In addition to the promise as IG material, CdZnTe is promising for infrared materials in terms of its transparency and commercial availability of large and high-quality transparent ingots. For example, a 5-inch diameter CdZnTe ingot is the current maximum, and a 6-inch diameter one is at the experimental stage (Noda et al. 2011). The infrared performance of CdZnTe is less studied compared to that of CdTe. Especially, cryogenic absorption coefficient of CdZnTe has not been researched yet, although infrared optics and cryogenic techniques are sometimes used together as in astronomical observations (e.g., SPICA). This study is important to research the properties of CdZnTe not only as an IG material but also as general infrared material.

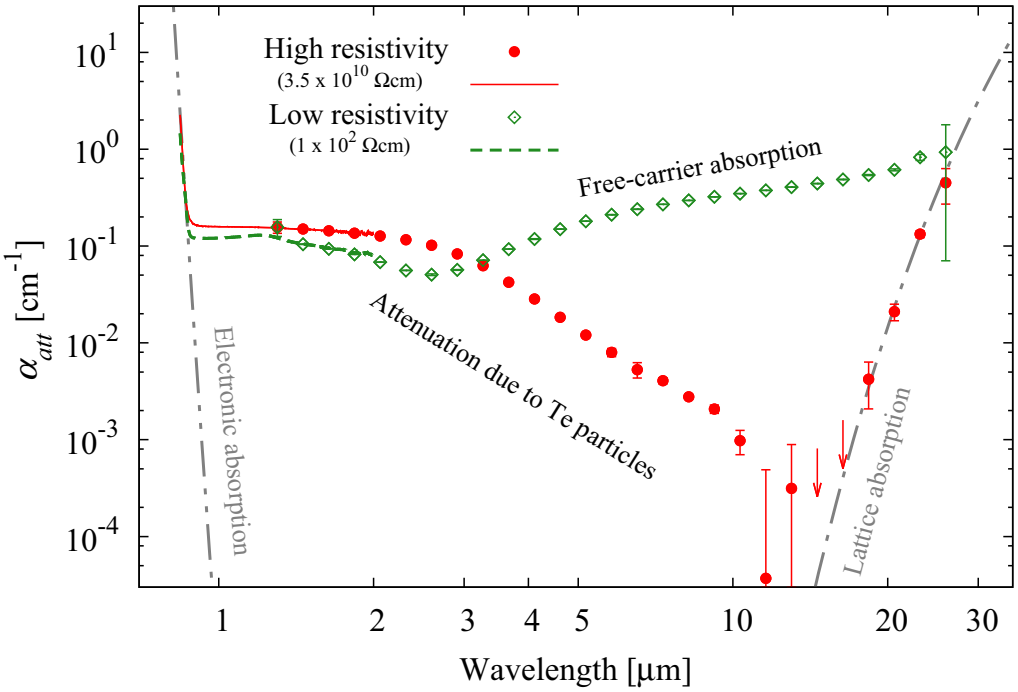

Figure. 1.9 Infrared absorption coefficients α_{att} of the high/low-resistivity CdZnTe at 295 K (Sarugaku et al. 2017). Grey lines show electronic absorption and lattice absorption, respectively. The electronic absorption is the absorption due to the electronic transition between the valence band and the conduction band. The lattice absorption is the absorption due to lattice vibrations. In the high-resistivity CdZnTe, the dominant absorption source is considered to be Mie scattering attenuation by Te precipitates at 1–12 μm.

1.5 The purpose and outline of this thesis

We have been developing the cryogenic 10–18 μm IG for SPICA SMI/HR. Current problems of material selection of the IG are as follows:

- The 5–20 μm absorption coefficient of CdZnTe has not been measured at cryogenic temperature.
- What causes absorption in CdZnTe at 5–20 μm has not been studied. Therefore, there is no guideline on how to tune the CdZnTe properties suitable for cryogenic IG.

The purposes of this thesis are as follows:

- to reveal what causes 5–20 μm absorption in CdZnTe at room and cryogenic temperatures
- to determine whether CdZnTe is suitable as a material for the 10–18 μm cryogenic IG

To achieve the purposes, we measure the absorption coefficient of the low/high-resistivity CdZnTe at 5–20 μm at 4.8–300 K with high precision ($\Delta\alpha < 0.003$ cm^{-1}). We have to solve the following two problems to conduct this measurement:

- We need to measure the absorption coefficient of the low/high-resistivity CdZnTe at 5–20 μm with an uncertainty $\Delta\alpha < 0.003$ cm^{-1} (See section 2.1). To achieve the high-accuracy measurement, we combine two types of transmittance measurements: (1) FTS measurements with an uncollimated beam and (2) measurements with a collimated beam and bandpass filters. (1) The FTS measurement provides a wavenumber dependence of the absorption coefficient, although the measurement yields systematic uncertainty of the absorption coefficient due to the defocus effect (See section 2.2). On the other hand, (2) an originally developed measurement system with a collimated beam provides absorption coefficients without the defocus error at specified wavelength bands. The combination of the two experiments is expected to give a wavenumber dependence of the absorption coefficient without the defocus uncertainty.
- CdZnTe samples should be cooled down to 4.8 K. To cool the samples to 4.8 K, we place the samples at a position close to the cold-head at < 4.8 K in a compact cryostat and secure thermal contact area.

New points of the current thesis improved from past studies (Kaji et al. 2014, 2016; Sarugaku et al. 2017) are as follows:

- Sarugaku et al. (2017) showed the Mie scattering attenuation due to Te precipitates by using a scattering model. However, Sarugaku et al. (2017) did not discuss other absorption factors at 5–20 μm. We aim to reveal what causes absorption in CdZnTe at 5–20 μm by comparing the temperature dependence of the absorption coefficient and an absorption model.

- Kaji et al. (2014) and Sarugaku et al. (2017) measured the absorption coefficient of CdZnTe at 295 K. Kaji et al. (2016) constructed an absorption coefficient measurement system at $\sim$ 29 K. We aim to measure the absorption coefficient over a wider temperature range (4.8–300 K). On the basis of the temperature dependence of the absorption coefficient at a wider temperature range than the past studies, we aim to discuss the factor causing absorption more clearly and to determine the suitability as an IG material at cryogenic temperature.

The research in this thesis includes joint research with Nagoya University. We conducted two types of experiments (chapter 3 and chapter 4), and the author of the thesis made the following main contributions:

- The author primarily developed and constructed an original optical system (section 4.1).
- The author acquired and analyzed data from both experiments.
- The results from both experiments were discussed mainly by the author.

The thesis consists of six sections. Following the introduction in section 1, section 2 describes the samples and an overview of the method. Sections 3 and 4 describe the method and result of each experiment. We combine the results of the two experiments and discuss the absorption factors and the suitability for IG in section 5. The conclusions are summarized in section 6.

§2

Method

In this section, we describe our method to measure the absorption coefficient of CdZnTe. Section 2.1 describes the total requirement to achieve our purpose. Section 2.2 describes the overview of the method and the individual requirement of each experiment. Section 2.3 describes the target samples.

2.1 Requirements

Firstly, we evaluate the total required uncertainty of the absorption coefficient measurement for our purpose. Our purpose is to determine whether the CdZnTe meets the absorption coefficient requirement or not. From the IG requirement $\alpha < \alpha_{\mathrm{IGreqd}} \equiv 0.01$ cm^{-1}, we set the required total uncertainty as $\Delta\alpha_{\mathrm{tot}} < \alpha_{\mathrm{IGreqd}}/3 = 0.003$ cm^{-1}.

We set the required lowest temperature as 4.8 K, which is the operating temperature of the IG on SPICA SMI/HR (Roelfsema et al. 2018). We discuss whether the required temperature also meets the other aim to determine what causes the absorption. The dominant absorption source in low-resistivity CdZnTe is considered to be free-carriers in previous studies (Sarugaku et al. 2017). In the ionization temperature regime, where the carriers are ionized moderately from donor or acceptor level, the carrier density is proportional to $f(T) = \exp(-\frac{E_a}{2k_BT})$, where E_a is the energy separation of donor/acceptor level from the conduction/valence band (Kittel 2005). If we assume that E_a of CdZnTe is the same as that of CdTe ($E_a = 60$ meV; Ahmad 2015), the free-carrier density will be reduced by $< f(50\ \mathrm{K})/f(300\ \mathrm{K}) = 1/300$ by cooling from 300 K to < 50 K. Since the free carrier absorption coefficient is proportional to free-carrier density, we can confirm the temperature dependence of α by cooling to 4.8 K. Therefore, the temperature requirement of 4.8 K is reasonable to achieve the purposes.

2.2 Overview of the methods

In this section, we discuss the overview of the methods. Section 2.2.1 describes the derivation method of absorption coefficient. Section 2.2.2 discusses systematic uncertainty due to defocus. The individual requirement of each measurement is described in section 2.2.3.

2.2.1 Measurement of absorption coefficient

By measuring the transmittance of samples with different thickness, we can derive absorption coefficient. The transmittance τ of a flat substrate at 0° incidence angle including multiple reflections in the sample can be expressed as

$$\begin{aligned}\tau &= (1-R)^2\exp(-\alpha t) + (1-R)^2R^2\exp(-3\alpha t) + (1-E)^2R^4\exp(-5\alpha t) + \cdots \\ &= (1-R)^2\exp(-\alpha t)\sum_{i=0}^{\infty}\left(R^2\exp(-2\alpha t)\right)^i \\ &= \frac{(1-R)^2\exp(-\alpha t)}{1-R^2\exp(-2\alpha t)},\end{aligned} \tag{2.1}$$

where R is the Fresnel reflectivity of a surface, α is absorption coefficient and t is the thickness of the sample. When the incident angle is 0°, Fresnel reflectivity is expressed with refractive index n as

$$R = \frac{(n-1)^2}{(n+1)^2}. \tag{2.2}$$

By measuring the transmittance of two samples (τ_1, τ_2) with the same material with different thickness (t_1, t_2), we can derive the absorption coefficient α as follows:

$$\frac{\tau_1}{\tau_2} = \frac{1-R^2\exp(-2\alpha t_2)}{1-R^2\exp(-2\alpha t_1)}\exp(-\alpha(t_1-t_2)) \tag{2.3}$$

$$\begin{aligned}\alpha &= -\frac{\ln(\tau_1/\tau_2)}{t_1-t_2} + \frac{1}{t_1-t_2}\ln\left[\frac{1-R^2\exp(-2\alpha t_2)}{1-R^2\exp(-2\alpha t_1)}\right] \\ &= -\frac{\ln(\tau_1/\tau_2)}{t_1-t_2} + \Delta\alpha_{\rm calc}\end{aligned} \tag{2.4}$$

$$\Delta\alpha_{\rm calc} \equiv \frac{1}{t_1-t_2}\ln\left[\frac{1-R^2\exp(-2\alpha t_2)}{1-R^2\exp(-2\alpha t_1)}\right]. \tag{2.5}$$

Here, we assume that R and α are common to the two samples. Figure 2.1 shows the ratio of $\Delta\alpha_{\rm calc}$ to α in the case of $t_1 = 1$ mm and $t_2 = 10$ mm (See section 2.3). We estimate three case of a refractive index n =2.65, 2.70 and 2.75 (c.f. n(CdZnTe) = 2.7; Ikeda et al. 2015). The contribution of $\Delta\alpha_{\rm calc}$ is at most 10% of total absorption coefficient. If we include the $\Delta\alpha_{\rm calc}$ to systematic error, we can approximate α as follows:

$$\alpha = -\frac{\ln(\tau_1/\tau_2)}{t_1-t_2}. \tag{2.6}$$

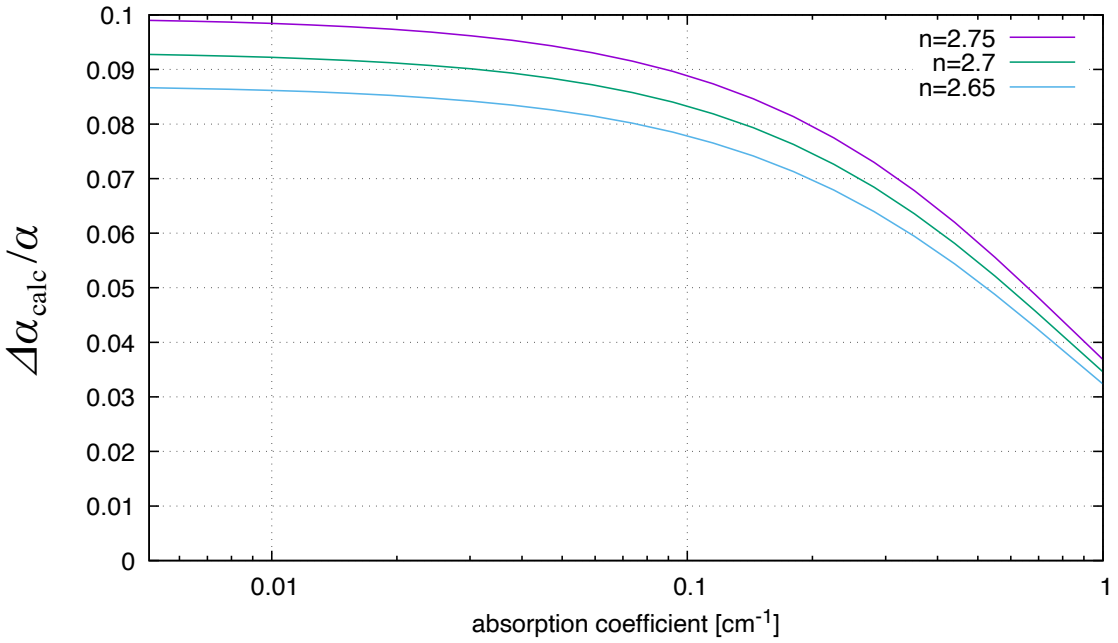

Figure. 2.1 The contribution of $\Delta\alpha_{\mathrm{calc}}$ to the total absorption coefficient α in the case of $n = 2.65,\ 2.70,\ 2.75$.

Therefore, we can derive α without the assumption of the value of the surface reflectivity R. In actual measurements, the multiple-reflected beams within samples shift from the main optical path as the number of reflections increases. Therefore, $\Delta\alpha_{\mathrm{calc}}$ derived in equation 2.5 is the maximum value of the systematic uncertainty due to calculation.

2.2.2 Systematic uncertainty due to defocus and the correction method

Here, we describe the systematic uncertainty due to defocus in transmittance measurement and the method to correct this uncertainty.

For thick and high-refractive-index sample cases, there may be large systematic uncertainty by defocus loss in a transmittance measurement with a typical Fourier Transform Spectrometer (FTS). FTS is a typical transmittance measurement system, where an interference light with a time-changing optical path difference passes through a sample. Transmittance is derived by an inverse Fourier transform of optical-path-difference dependence of the synthesized transmitted light power (interferogram). Figure 2.2 shows a schematic view of defocus loss. By placing a high-refractive-index sample in the sample compartment, the optical path is extended, and the focus position on the detector shifts backward. The defocus effect changes an illumination pattern on the detector causes light loss and yields a large uncertainty of a measured value.

To achieve the high precision measurement of the absorption coefficient, we have to solve the defocus problem described above. To solve the defocus problem, we combine two types of experiments. One is (1) an experiment with an uncollimated light FTS. The experiment

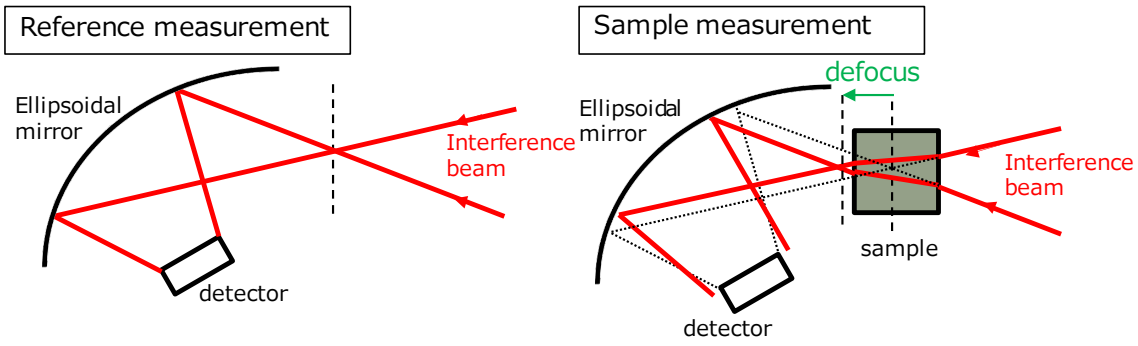

Figure. 2.2 A schematic view of the defocus effect with a FTS. (Right) Reference measurement case. (Left) Sample measurement case.

yields wavenumber dependences of relative absorption coefficient α, although there may be large systematic error by the defocus. The other is (2) an experiment with a collimated globar lamp light and bandpass filters. Experiment (2) yields the absolute value of α at some wavelength band. By combining experiments (1) and (2), we can correct the systematic error of (1) and gain the absolute wavenumber dependence of the α. Details of the two measurements are described in chapter 3 and chapter 4.

Next, we discuss how we perform the correction. We assume the measured transmittance $\tau_{\mathrm{FTS},i}$ of sample-i with an uncollimated FTS is given by

$$\tau_{\mathrm{FTS},i} = k_i \tau_{0,i}, \tag{2.7}$$

where $\tau_{0,i}$ is the transmittance without the defocus error, and k_i is a factor to express this error. From equation 2.6, the α measured with FTS (α_{FTS}) is expressed as

$$\begin{aligned} \alpha_{\mathrm{FTS}}(\tilde{\nu}) &= \alpha_0(\tilde{\nu}) + \frac{\ln(k_1/k_2)}{t_1 - t_2} \\ &= \alpha_0(\tilde{\nu}) + C(\tilde{\nu}), \end{aligned} \tag{2.8}$$

where α_0 is the absorption coefficient without defocusing loss and C is a correction term of the defocus error. We assume that the absorption coefficient measured with the collimated beam (α_{col}) shows α_0 since the α_{col} is free from the defocus error. Therefore, the C at the wavelength band ($\tilde{\nu}_k$) can be expressed as

$$C(\tilde{\nu}_k) = \overline{\alpha_{\mathrm{FTS}}(\tilde{\nu}_k)} - \alpha_{\mathrm{col}}(\tilde{\nu}_k), \tag{2.9}$$

where $\overline{\alpha_{\mathrm{FTS}}(\tilde{\nu}_k)}$ is the averaged value of α_{FTS} among the wavelength band. The corrected absorption coefficient α_0 is expressed as

$$\alpha_0(\tilde{\nu}) = \alpha_{\mathrm{FTS}}(\tilde{\nu}) - C(\tilde{\nu}). \tag{2.10}$$

Assuming the correction factor $C(\tilde{\nu})$, we can correct the uncertainty due to the defocus.

2.2.3 Requirements of each measurement

Here we discuss the requirements of each measurement. Table 2.1 summarizes the requirements of each measurement. The derivation of the value is described below.

Table. 2.1 The requirement of each measurement

total uncertainty		$\Delta\alpha_{\rm tot} :< 0.003$ cm^{-1}
experiment 1	statistical uncertainty	$\Delta\alpha_{\rm FTS,stat} :< 0.0025$ cm^{-1}
		$\rightarrow \Delta\tau_{\rm FTS,stat}/\tau :< 0.001$
	wavelength range	$\tilde{\nu}$: 2000–500 cm^{-1} (5–20 μm)
	temperature range	T: 4.8–300 K
experiment 2	statistical uncertainty	$\Delta\alpha_{\rm col,stat} :< 0.0025$ cm^{-1}
		$\rightarrow \Delta\tau_{\rm col,stat}/\tau : < 0.001$
	wavelength	2 or more bands within 5–20 μm
	temperature range	T: 4.8–300 K
calculation[a]	systematic uncertainty	$\Delta\alpha_{\rm calc} :< 0.1\alpha$ cm^{-1}
		(< 0.001 at $\alpha = 0.01$)
samples	thickness	$\sim t1, \sim t10$ mm

a: systematic uncertainty due to calculation as $\Delta\alpha_{\rm calc} \lesssim 0.1\alpha$ in equation 2.5.

First, we estimate the uncertainty of C. We assume that the absorption coefficient differences $\alpha_{\rm FTS} - \alpha_{\rm col}$ are randomly distributed around the correction factor C. The uncertainty of C can be evaluated from equation 2.9 by the error propagation law as follows:

$$\Delta C^2 = \frac{1}{N_{\rm band}} \sum_i^{N_{\rm band}} \left(\left[\Delta(\overline{\alpha_{\rm FTS}(\tilde{\nu}_i)}) \right]^2 + (\Delta\alpha_{\rm col}(\tilde{\nu}_i))^2 \right) \tag{2.11}$$

$$\Delta C = \sqrt{\frac{(\Delta\alpha_{\rm FTS,stat}/\sqrt{N_{\rm FTS}})^2 + (\Delta\alpha_{\rm col,stat})^2}{N_{\rm band}}}, \tag{2.12}$$

where $N_{\rm band}$ is the number of wavelength bands with a collimated beam ($N_{\rm band} = 4$. See section 4) and $N_{\rm FTS}$ is the number of $\alpha_{\rm FTS}$ data points within the band ($N_{\rm FTS}$ =7–66, depends on bandwidths. See section 3). Statistical uncertainties of the FTS and the collimated beam measurement are denoted as $\Delta\alpha_{\rm FTS,stat}$ and $\Delta\alpha_{\rm col,stat}$, respectively. The total uncertainty is expressed as

$$\begin{aligned}
\Delta\alpha_{\rm tot} &= \sqrt{\Delta\alpha_{\rm FTS,stat}^2 + \Delta C^2} + \Delta\alpha_{\rm calc} \\
&= \sqrt{\left(1 + \frac{1}{N_{\rm FTS}N_{\rm band}}\right)\Delta\alpha_{\rm FTS,stat}^2 + \frac{1}{N_{\rm band}}\Delta\alpha_{\rm col,stat}^2} + \Delta\alpha_{\rm calc} \\
&\simeq \sqrt{\Delta\alpha_{\rm FTS,stat}^2 + \frac{1}{4}\Delta\alpha_{\rm col,stat}^2} + \Delta\alpha_{\rm calc},
\end{aligned} \tag{2.13}$$

where $\Delta\alpha_{\rm calc}$ is uncertainty due to calculation as $\Delta\alpha_{\rm calc} \lesssim 0.1\alpha$ in equation 2.5. Here we approximate that $1 + 1/(N_{\rm FTS}N_{\rm band}) \simeq 1$.

From the absorption coefficient requirement, the required statistical uncertainty of transmittance $\Delta\tau_{\rm stat}$ can be derived from the error propagation law:

$$\Delta\alpha_{\rm stat} = \frac{\Delta\tau_{\rm stat}}{t_1 - t_2}\sqrt{1/\tau_1^2 + 1/\tau_2^2} + \Delta\alpha_{\rm calc} \tag{2.14}$$

$$\Delta\tau_{\rm stat}/\tau = \frac{(\Delta\alpha_{\rm stat})(t_1 - t_2)}{\sqrt{2}} \simeq 0.001 \left(\frac{t_1 - t_2}{9\ {\rm mm}}\right)\left(\frac{\Delta\alpha_{\rm stat}}{0.0025\ {\rm cm}^{-1}}\right) \quad (\tau_1 \simeq \tau_2), \tag{2.15}$$

We set $t_2 \sim 1$ mm, which is a minimum thickness that can be manually handled. Cooling a thicker sample is more difficult, although the $\Delta\tau_{\rm stat}/\tau$ requirements can be more relaxed. Then, we set the requirement of $\Delta\tau_{\rm stat}/\tau < 0.001$, which is challenging but feasible, and t_1 is required to be ~ 10mm.

We set the required wavenumber range in experiment 1 as 2000–500 cm^{-1} (5–20 μm). This range covers the wavelength range of SPICA SMI/HR (10–18 μm; Wada et al. 2020). Furthermore, there is a more than tenfold difference of the absorption coefficient between the low- and high-resistivity CdZnTe measured by Sarugaku et al. (2017). If free-carrier absorption is dominant absorbance in the low-resistivity CdZnTe, the absorption coefficient at 5–20 μm may clearly change with temperature (See Figure 1.9; Sarugaku et al. 2017). To research the factors causing absorption in CdZnTe, we need to measure the absorption coefficient at this wavelength range from room temperature to cryogenic temperature.

To summarize the above discussion, we plan to combine two types of experiments to correct the uncertainty due to the defocus error. One is (1) transmittance measurements with an FTS, and the other is (2) those with a collimated beam and bandpass filters. We set the total uncertainty requirement of absorption coefficient as $\Delta\alpha < 0.003$ cm^{-1}. Then we set the transmittance uncertainty requirement of each measurement as described in Table 2.1. We set the target temperature as < 4.8 K, which is the IG operating temperature on SMI/HR. If these requirements of the measurements are met, the absorption coefficient can be measured with high precision ($\Delta\alpha < 0.003$ cm^{-1}) at 4.8–300 K and we can determine whether the CdZnTe is suitable as a cryogenic IG material.

2.3 Sample

In this section, we describe the target samples. To compare transmittance difference by the thickness and by the resistivity, we prepared four different samples with two different resistivities and two different thicknesses (Figure 2.3). Specifications of the samples are listed in Table 2.2. Measured samples are $Cd_{0.96}Zn_{0.04}Te$ ($n \sim 2.7$) single crystals manufactured by JX Nippon Mining & Metals Corporation. CdZnTe Ingots were made by vertical gradient freezing (VGF) method. The manufacturer controlled the conductivities and cut out substrates from the ingots. The conductivity condition is the same as that studied by Sarugaku et al. (2017) in order to compare our results and this previous study. We note that the conductivity type is different between lowR-t1/t10 and highR-t1/t10: lowR-t1/t10 are p-type and highR-t1/t10 are n-type. The high-resistivity CdZnTe crystals are made by doping with indium for compensation and become n-type conductivity (Sarugaku et al. 2017). Then the ingot was annealed to reduce the size of Te precipitates to less than 2 μm (Noda et al. 2011). By reducing the precipitate size, the attenuation due to Mie scattering with Te precipitates can be reduced (Sarugaku et al. 2017). The thicknesses were set as ~ 1 or ~ 10mm from the requirement (section 2.2.3). To reduce light scattering loss on the sample surface, the incident and exit surfaces were polished with a surface roughness of $Ra < 1$ nm, where Ra is calculated average roughness.

These samples meet the thickness requirement described in section 2.2.3 and suitable for transmittance measurements. By measuring the transmittances of these samples, we expect to obtain thickness dependence of the transmittance to estimate the absorption coefficient of the low/high-resistivity CdZnTe.

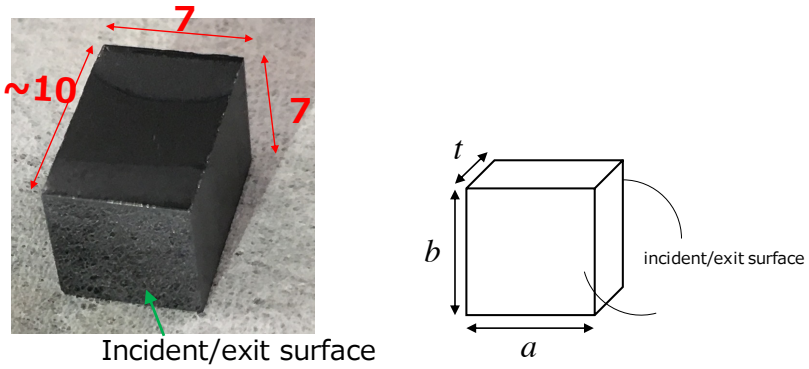

Figure. 2.3 (Left)A photo of lowR-t10 sample. (Right) Schematic view of a sample.

Table. 2.2 Sample list of CdZnTe single crystals. Described values are specified at room temperature. *Ra* is the surface roughness of the incident and exit surface.

name	resistivity [Ω cm]	$a \times b$ [mm^2]	t [mm]	conductivity type	Ra [nm]	Te precipitate size [μm]
lowR-t1	$(0.5 \sim 1.3) \times 10^2$	7.0×7.0	1.01	p	< 1	< 2
lowR-t10	$(0.5 \sim 1.3) \times 10^2$	7.0×7.0	9.91	p	< 1	< 2
highR-t1	$> 10^{10}$	10×10	0.79	n	< 1	< 2
highR-t10	$> 10^{10}$	7.0×7.0	9.94	n	< 1	< 2

2.4 Summary of this chapter

In this chapter, we describe an overview of the methods, their requirements, and samples.

We conduct two types of experiments to measure absorption coefficient with high precision ($\Delta\alpha < 0.003$ cm^{-1}). First, we measure the transmittance of samples with (1) a Fourier transform spectrometer (FTS) with an uncollimated beam. This measurement provides wavenumber dependence of absorption coefficient, although the measurement yields systematic uncertainty due to the defocus effect. To correct this defocus error, we measure the transmittance with (2) an originally developed collimated lamp beam system. This system provides the absorption coefficient free from the defocus error, although we can measure the transmittance at limited wavelengths.

Then, we estimate the uncertainty in order to achieve the required total absorption coefficient uncertainty. We set the transmittance uncertainty requirement of each measurement as $\Delta\tau/\tau < 0.001$. Also, we set the target temperature as $T < 4.8$ K, which is the IG operating temperature on SMI/HR. If these requirements of the measurements are met, the absorption coefficient can be measured with high precision at 4.8–300 K, and we can determine whether the CdZnTe is suitable as a cryogenic IG material.

To compare transmittance difference by the thickness and by the resistivity, we prepared four different samples with two different resistivities ($\sim 10^2, > 10^{10}$ Ωcm) with two different thicknesses ($\sim t1, \sim t10$ mm). Comparing the transmittance of samples with the same resistivity with different thickness, we can estimate the absorption coefficient of the low/high-resistivity CdZnTe.

§3

Experiment1 :Fourier-Transform spectroscopy

In order to measure wavenumber dependences of the absorption coefficients of the samples, we measure transmittance with FTS systems. Measurement with an FTS provides a wavenumber dependence of absorption coefficient, although the measurement yields systematic errors due to the defocus (See section 2.2.2). The experiment for the correction of this defocus error is described in chapter 4. We used an FTS and a cryostat system at Infrared Astronomy Laboratory (Uir-Lab.) in Nagoya University and an FTS at Laboratory of Infrared Astrophysics (LIRA) in Institute of Space and Astronautical Science (ISAS).

Section3.1 describes the measurement method. Section 3.2 describes the results of measurements with the two FTS systems.

3.1 Method

The requirements of this experiment are summarized in table 3.1. The derivation of the requirements is described in section 2.2.3.

Table. 3.1 Requirements of experiment 1.

statistical uncertainty:	$\Delta\tau_{\mathrm{FTS,stat}}/\tau < 0.001$
wavenumber (wavelength):	2000–500 cm^{-1} (5–20 μm)
temperature:	4.8–300 K

Because of lack of measurement time with the FTS and cryostat system at Uir-Lab, instruments for low/highR-t10 cases and that for low/highR-t1 cases are different. Table 3.2 summarizes measurement instruments and temperature ranges for each sample. Details of low/highR-t10 cases are described in section 3.1.1 and those of low/highR-t1 cases in section 3.1.2.

Table. 3.2 Measurement method for each sample.

sample	system	temperature [K]
lowR-t10	FTS (vertex 70v) with cryostat	4.8–300 K
highR-t10	FTS (vertex 70v) with cryostat	4.8–300 K
lowR-t1	FTS (vertex 80v)	300 K
highR-t1	FTS (vertex 80v)	300 K

3.1.1 Measurements of low/highR-t10 at cryogenic and room temperatures

Here we discuss the method of transmittance measurement of low/highR-t10.

First, we describe the optical system. We use a benchtop vacuum FTS (Vertex 70v; Bruker optics inc.). Figure 3.1 shows the optical system of the Vertex 70v. The settings of the FTS are summarized in Table 3.3. To measure transmittance at 2000–500 cm^{-1}, we set a U-shaped silicon carbide globar lamp, a KBr beam splitter, and a DLaTGS detector, which are suitable for this wavenumber range. The incident beam on the samples is convergent, and its F-number is F/3.73. The pressure in the sample compartment is reduced to < 0.1 Pa in order to reduce absorption by H_2O and CO_2 in the air.

Next, we describe the cryostat which we use to cool the samples. To cool the samples to < 4.8 K, we use a continuous liquid helium flow type cryostat (Optistat CF-V; Oxford instruments). Figure 3.2 (a) (b) shows the installation position of the cryostat and the structure of the cryostat. The lowest temperature in the specification is 4.2 K by continuous helium flow, which meets the required temperature. The flow speed of liquid helium is controlled by a transfer tube and a pump at 0.5-1.4 L(liquid He)/hour. To transmit mid-infrared beam, ϕ40 mm polyethylene

Table. 3.3 Setting parameters of the FTS.

parts	settings
light source	globar (8,000–50 cm^{-1})
beam splitter	KBr (33,000–280 cm^{-1})
detector	DLATGS (12,000–250 cm^{-1})
wavenumber range	2000–500 cm^{-1} (=5–20 μm)
aperture	2 mm
apodization function	Blackman-Harris 3-Term
resolution (after apodization)	1 cm^{-1}
pressure in the sample compartment	< 0.1 Pa
pressure in the cryostat	< 0.01 Pa

windows are equipped. To reduce radiative heat inflow, ϕ23 mm black-polyethylene[*1] sheets are equipped on the radiation shield. Figure 3.3 shows the total transmittance of the windows and sheets. The pressure in the cryostat is reduced to < 0.01 Pa in order to reduce convective heat inflow by the air. The temperature on the cold head is measured using a calibrated rhodium-iron temperature sensor equipped in the cryostat.

Then, we discuss the sample holder. Figure 3.2 (c) shows the structure of the sample holder. The top surface of the holder is fixed to the cold head surface with screws to secure thermal contact. The holder has a ϕ6 mm hole through which the incident beam passes. With screws, samples are clamped between the holder and the holding plate. Indium sheets and varnish (GE7031) are inserted between the sample and the holder and between the sample and the plate to secure enough thermal contact[*2]. A temperature sensor calibrated at 1.4–325 K (CX-1030-

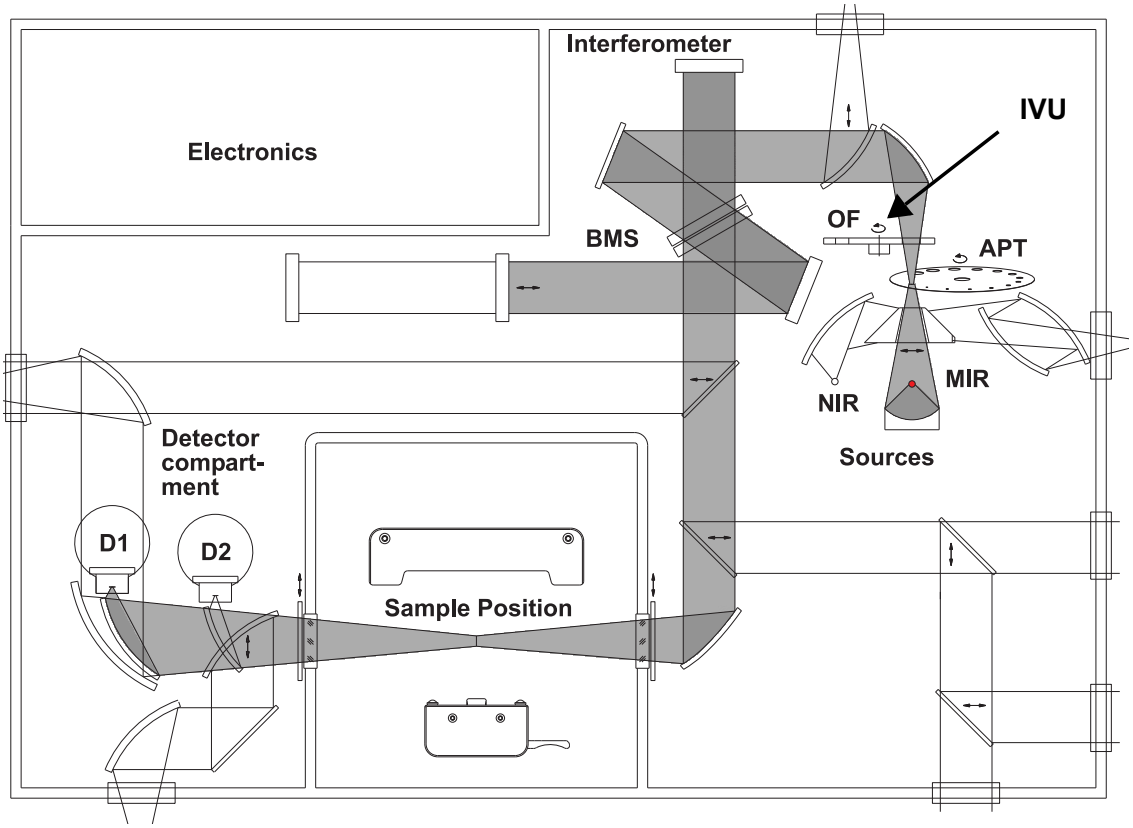

Figure. 3.1 Optical beam path of Vertex 70v cited from the user manual (https://www.bruker.com). NIR, MIR, APT and BMS denote a near-infrared source, mid-infrared source, an aperture and a beam splitter, respectively. IVU and OF denote an internal validation unit and a standard optical filter equipped with IVU. An internal validation unit is a filter wheel to check operational and performance qualification of the FTS by standard filters. D1 and D2 show standard and optional detectors. We use the standard detector (D1).

[*1] Black-polyethylene is a composite of polyethylene and carbon powder (Wakaki et al. 2007).

[*2] GE7031 varnish is a commonly used cryogenic adhesive with low electrical conductivity with relatively high thermal conductivity.

CU-HT-1.4L; Lakeshore inc.) is attached to the holder with varnish (GE7031) to monitor the temperature of the holder.

We now describe the measurement process. We measure the transmittance of lowR-t10 and highR-t10 based on the ratio of transmitted light power with and without the sample. We conduct the transmittance measurement at 300 K and at the lowest temperature. During the cooling and the heating process, we control a heater on the cold-head and the helium flow pump so that the cooling rate is lower than 6 K/min to limit thermal stress on the sample.

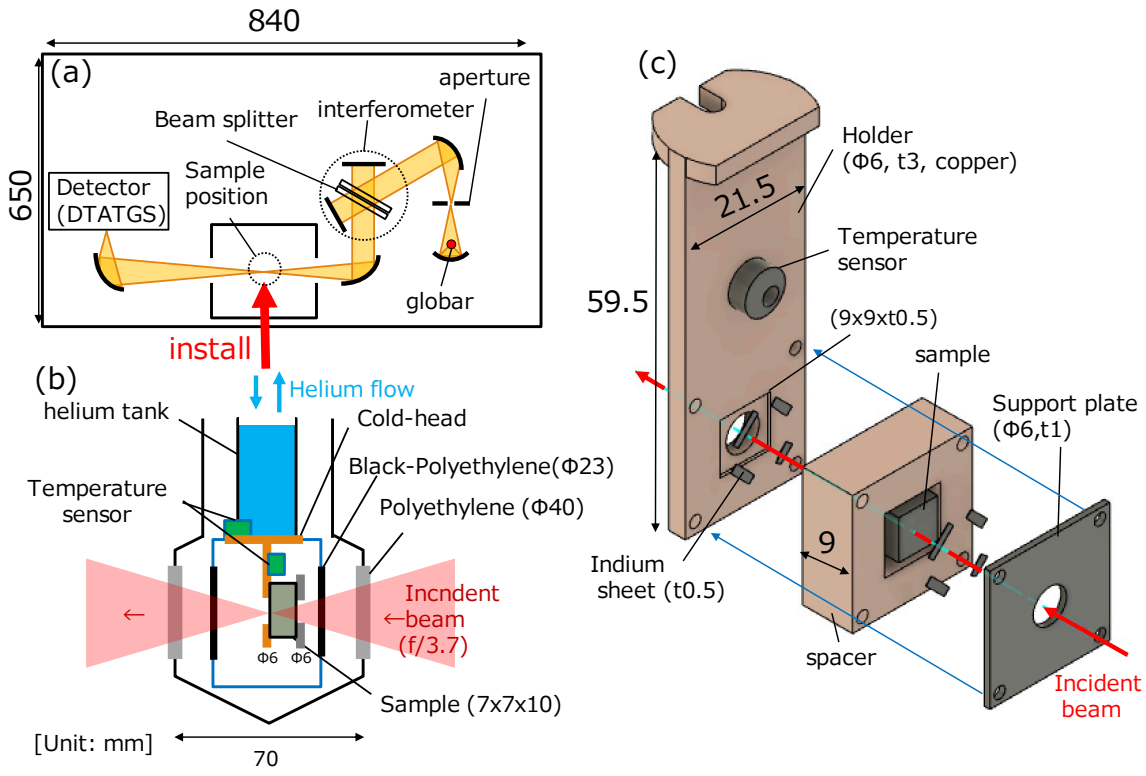

Figure. 3.2 (a) Optical system of Vertex 70v. (b) Structure of the cryostat. (c) Structure of the sample holder for thick samples (low/highR-t10).

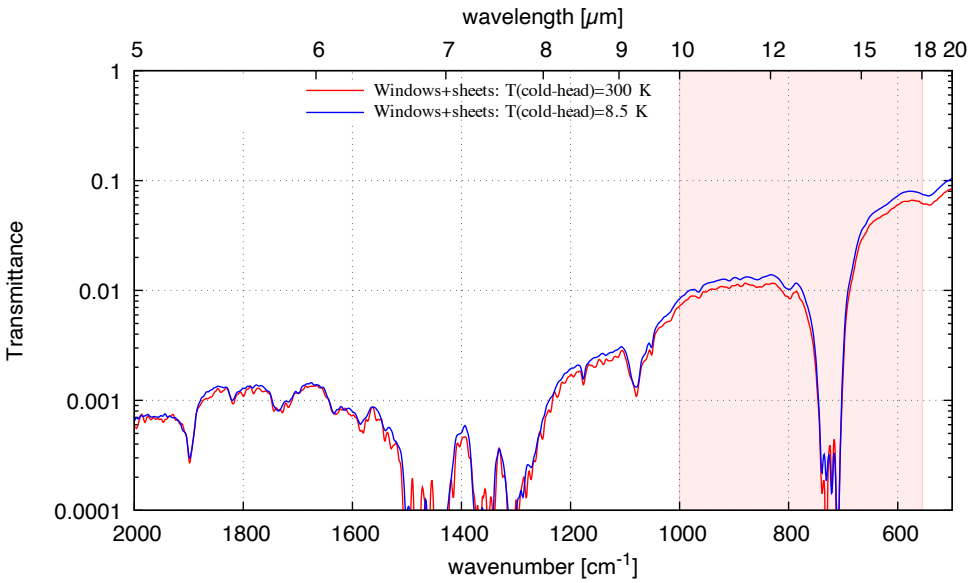

Figure. 3.3 The total transmittance of the windows and sheets on the cryostat (two polyethylene windows and two black-polyethylene sheets) measured at room temperature and when the cold-head is cooled down to cryogenic temperature. When the cold-head is cooled, the black-polyethylene sheets are cooled to cryogenic temperature, although the polyethylene windows are at room temperature. Therefore, the total transmittance changes when the cold-head is cooled. Absorption features at 6.8, 7.5 and 13.8 μm are consistent with the literature feature of black-polyethylene (Wakaki et al. 2007). The pink region is SPICA SMI/HR wavelength range.

3.1.2 Measurement of low/highR-t1 at room temperature

To measure the thickness dependence of the transmittance, we measure the transmittance of lowR-t1 and highR-t1 at room temperature. Another FTS (Vertex 80v; Bruker Optics. inc.) is used in the measurements at LIRA in ISAS. The cryostat is not used since the measurement is performed only at room temperature. Another holder with the same-size aperture (ϕ6 mm) as that for thick samples is used. Other settings and the measurement procedure are the same as those for low/highR-t10 to make the measurement condition as close as possible to each other.

By measuring the transmittance of the low/high-resistivity CdZnTe with the above FTS systems described in section 3.1.1 and 3.1.2, we expect to obtain wavenumber dependences of transmittances of low/highR-t10 at room and cryogenic temperatures and those of low/highR-t1 at room temperature. Furthermore, we expect to obtain wavenumber dependence of the absorption coefficient of the low/high-resistivity CdZnTe at room and cryogenic temperature from the transmittance results.

3.2 Results

In this section, we describe the measurement results: cooling performance, transmittance and absorption coefficient. The comparisons of requirements and actual results are summarized in table 3.4. Details of the results are described in the following subsections.

Table. 3.4 Requirement and actual result of experiment 1

	requirements	actual results
low/highR-t10 (FTS+cryostat)		
short-term statistical uncertainty ($\Delta\tau_{\mathrm{stat,short}}/\tau$)	< 0.001	≤ 0.01 (at 10–18 μm)
		≤ 0.03 (at 5–20 μm)
long-term statistical uncertainty ($\Delta\tau_{\mathrm{stat,long}}/\tau$)	—	0.03
minimum temperature	< 4.8 K	8.5 ± 0.5 K
low/highR-t1 (FTS only)		
short- term statistical uncertainty ($\Delta\tau_{\mathrm{stat,short}}/\tau$)	< 0.001	2×10^{-4}
long-term statistical uncertainty ($\Delta\tau_{\mathrm{stat,long}}/\tau$)	—	2×10^{-3}
$\Delta\alpha_{\mathrm{FTS,stat}}$ [cm^{-1}]	$< 2.5 \times 10^{-3}$	< 0.01 (at 10–20 μm)
	$< 2.5 \times 10^{-3}$	< 0.03 (at 5–20 μm)

3.2.1 Cooling profiles

Here we describe the achieved cooling profiles to discuss whether the temperature of samples meets the temperature requirement. Figure 3.4 shows the temperature profiles of the cold-head and the holder during the cooling and heating process. As shown in Figure 3.4, the cooling process takes $\sim$ 2 hours and the heating process takes $\sim$ 10 hours. The lowest temperature is 7.3 K and 8.5 K at the cold-head and the holder, respectively.

We discuss the temperature uncertainty. Possible factors causing temperature error are calibration error of the sensors, the uncertainty due to Seebeck effect[*3] and the scattering of the measured value. The calibration error is ignored because the sensor is well-calibrated. At cryogenic temperature, the scattering of the measured value is small. Therefore, the uncertainty of cryogenic temperatures is evaluated from the uncertainty due to the Seebeck effect. The wires connected to the sensor have temperature gradients, which causes voltage due to the Seebeck effect at low temperature. The uncertainty due to the Seebeck effect ΔT_{Se} is evaluated as $\Delta T_{\mathrm{Se}} = \pm 0.5$ K by swapping the polarity of the voltage applied to the sensor. At 300 K, the Seebeck effect is negligible for temperature monitoring. The uncertainty at room temperature is evaluated as $\Delta T = \pm 8$ K from the scattering of the measured resistance value.

The lowest temperatures are 7.3 ± 0.5 K and 8.5 ± 0.5 K at the cold-head and the holder, respectively. We assume the sample temperature is the same as the holder temperature because we secure thermal contact between the holder and the samples. The temperature of our sample reaches lower than that by Kaji et al. (2016) (T_{min} =29 K). We cannot achieve the required temperature (4.8 K), but we can estimate transmittances and absorption coefficients of samples at 4.8 K from results at 8.5 K from the temperature dependence of the absorption coefficient obtained by the experiment with collimated beam and bandpass filters (See chapter 4).

[*3] Seebeck effect is a phenomenon that causes voltage due to temperature difference in a material.

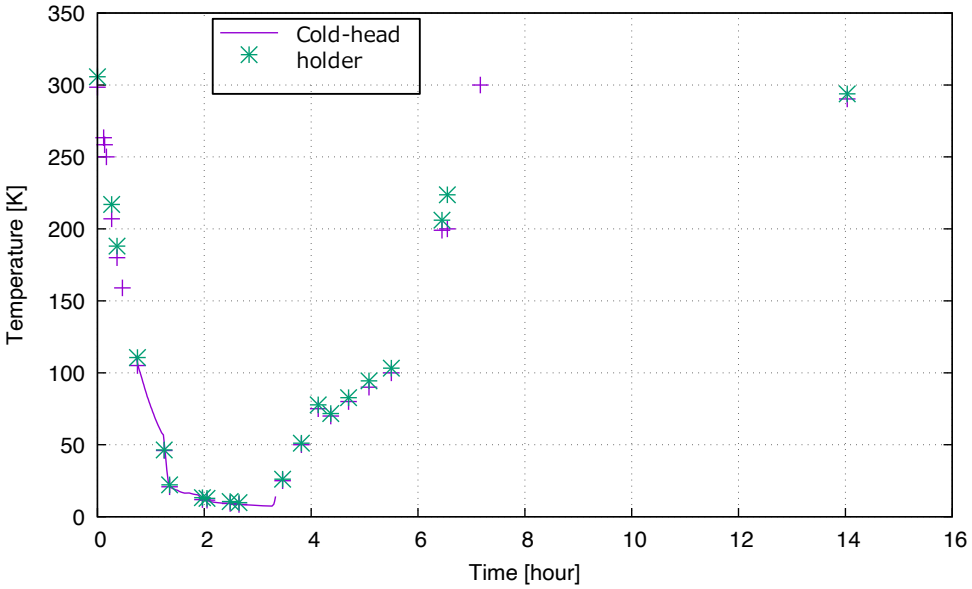

Figure. 3.4 Temperature profiles of the cold-head and the holder at transmittance measurement of lowR-t10. The lowest temperatures are 7.3 ± 0.5 K and 8.5 ± 0.5 K at the cold-head and the holder, respectively.

3.2.2 Transmittance

This section describes the result of transmittance measurement of samples at 300 K and at 8.5 K.

Figure 3.5 shows the transmittance τ of lowR-t10 and lowR-t1 measured with FTS systems. The τ of lowR-t10 is measured at 300 K and 8.5 K, and that of lowR-t1 is measured at 300 K. At the wavenumber range of 1550–1150 and 760–700 cm^{-1}, the reliability of the measured value of lowR-t10 is low because the transmittance of the cryostat windows is low at these wavelengths (See Figure 3.3). The 5–20 μm transmittance of lowR-t10 is $\tau = 0.33 - 0.57$ at 300 K and τ =0.18–0.59 at 8.5 K. We confirm that the lowR-t10 transmittance becomes lower at 10–20 μm with cooling. The lowR-t1 transmittance at 5–20 μm is $\tau = 0.60$–0.61 at all measured wavelengths. The transmittance difference between lowR-t1 and lowR-t10 is larger at the longer wavelength.

We evaluate the short-term statistical uncertainty of the measured transmittance to check whether it meets the requirement. We define short-term statistical uncertainty as the standard error of the measured value in $\lesssim 0.5$ hours. We stack the transmittance in each $\Delta\tilde{\nu} = 20$ cm^{-1} range in order to reduce the statistical uncertainty. The statistical uncertainty of lowR-t10 is $\Delta\tau_{\mathrm{stat,short}}/\tau$ =0.004–0.01 at 10–20 μm and $\Delta\tau_{\mathrm{stat,short}}/\tau$= 0.004–0.03 at 5–20 μm which is larger than the requirement ($\Delta\tau_{\mathrm{stat}}/\tau < 0.001$). The integration time of each measurement is set ~ 0.5 hours. To improve the $\Delta\tau/\tau < 0.001$ with the same system, we need an integration time of $0.5 \times (0.01/0.001)^2 = 50$ hours. This is not feasible from a practical point of view. On the other hand, the short-term statistical uncertainty of lowR-t1 is $\Delta\tau_{\mathrm{stat}}/\tau = 2 \times 10^{-4}$, which meets the requirement. The statistical uncertainty difference between lowR-t10 and lowR-t1 is due to the low transmittance cryostat windows for lowR-t10 case. The total transmittance of the cryostat windows is $\tau_{\mathrm{window}} = 10^{-3}$–0.1 (see Figure 3.3). Therefore, the signal to noise ratios of lowR-t10 case is worse than those of lowR-t1 case.

Next, we describe the long-term statistical uncertainty $\Delta\tau_{\mathrm{FTS,stat,long}}$. The long-term statistical uncertainty $\Delta\tau_{\mathrm{FTS,stat,long}}$ is defined as the standard deviation of several measurements with the same condition in one cycle time of a set of reference and sample measurement. The $\Delta\tau_{\mathrm{stat,long}}/\tau$ is 0.03 for lowR-t10 case, and 0.002 for lowR-t1 case. This long-term uncertainty difference is considered to be due to the time-variation of the light source power. One cycle of lowR-t10 measurement, including cooling and heating, took $\gtrsim 12$ hours, and that of lowR-t1 at room temperature took ~ 0.5 hours. Since one cycle of lowR-t10 measurement took ~ 20 times longer than lowR-t1 measurement, time-variation of the power of the light source affect the long-term uncertainty of lowR-t10 more severely.

Figure 3.6 shows the transmittance of highR-t10 and highR-t1 measured with FTS. The calculation method of uncertainties is the same as the lowR-t10 and lowR-t1 case. The 5–20 μm transmittance of highR-t10 is $\tau = 0.64 - 0.70$ at 8.5 and at 300 K. The 5–20 μm transmittance

of highR-t1 is $\tau = 0.65 - 0.72$ at 300 K and becomes higher at a longer wavelength. Difference between the transmittance of highR-t10 at 8.5 K and 300 K is $(\tau(300\ \mathrm{K}) - \tau(8.5\ \mathrm{K}))/\tau(300\ \mathrm{K}) < 0.05$, which is smaller than 2-σ of the long-term statistical uncertainty ($2 \times \Delta\tau_{\mathrm{stat,long}}/\tau = 0.06$). Therefore, this transmittance difference due to temperature is not significant.

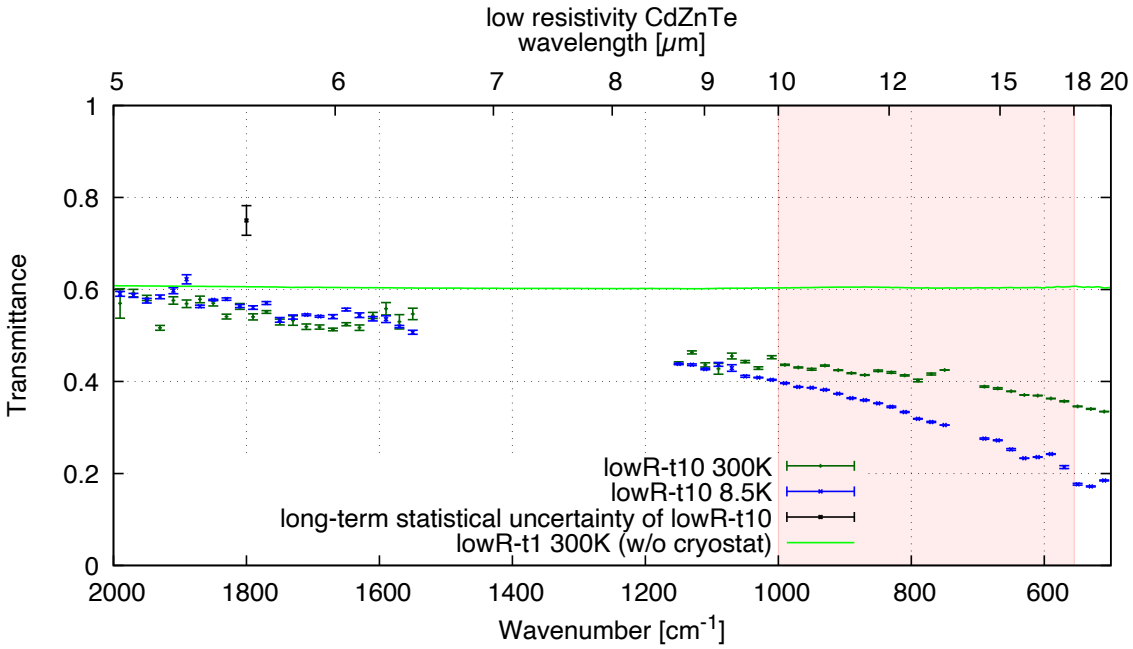

Figure. 3.5 The measured transmittance of the lowR-t10 and lowR-t1. Data in the region of low transmittance in the measurement system are excluded. The error bars on data points show the short-term statistical uncertainty. The black error bar shows long-term statistical uncertainty ($\Delta\tau_{\mathrm{stat,long}}/\tau = 0.03$) for lowR-t10.

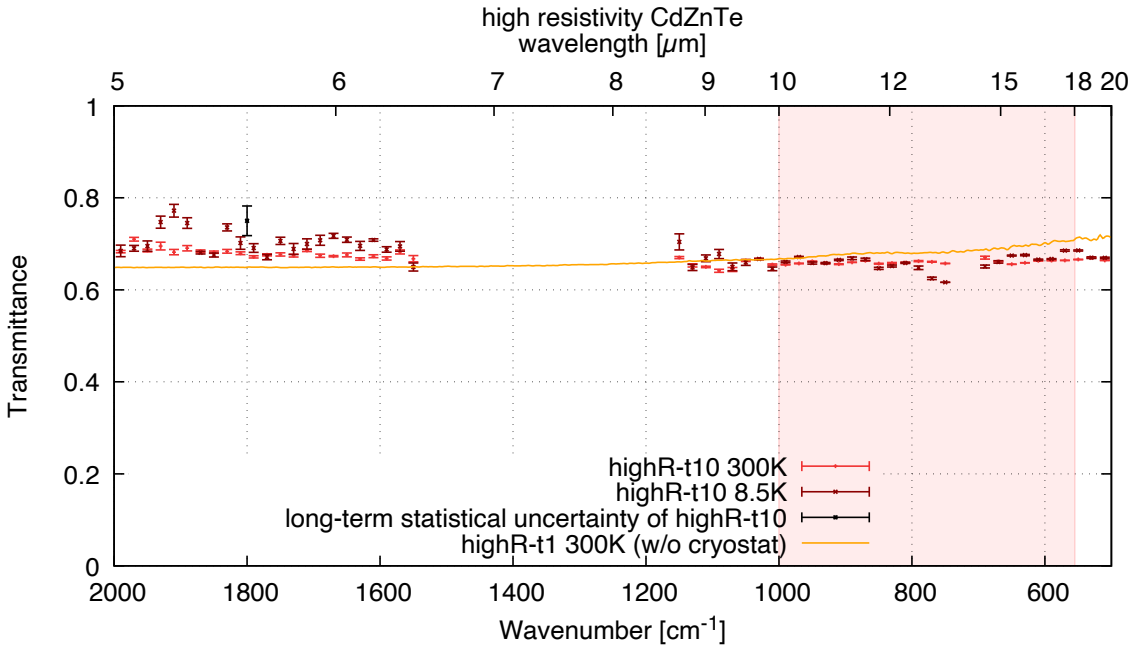

Figure. 3.6 The measured transmittance of the highR-t10 and highR-t1. Data in the region of low transmittance in the measurement system are excluded. The error bars on data points show the short-term statistical uncertainty. The black error bar shows long-term statistical uncertainty ($\Delta\tau_{\mathrm{stat,long}}/\tau = 0.03$) for highR-t10 .

3.2.3 Wavenumber dependence of relative absorption coefficient

We expect to obtain wavenumber dependence of the absolute coefficient without the defocus loss by correcting the results of FTS measurement (described in this section) with the result of collimated beam measurement (described in section 4.2.3). We define "relative" absorption coefficient as the absorption coefficient, including the systematic uncertainty due to the defocus loss. To prepare for the derivation of wavenumber dependence of absolute absorption coefficient α_0 without defocusing loss, we derive wavenumber dependence of relative absorption coefficient (α_{FTS}).

First, we describe the estimation method of α_{FTS} at 300 K. We assume that the surface reflectivity R of samples does not depend on thickness because the R is considered to be Fresnel reflectivity and depends only on the refractive index n for 0° incident angle case. From equation 2.6, we derive α_{FTS} at wavenumber $\tilde{\nu}$ at 300 K as follows:

$$\alpha_{\mathrm{FTS}}(\tilde{\nu}, 300\ \mathrm{K}) = -\frac{\ln[\tau_{\mathrm{t}10}(\tilde{\nu}, 300\ \mathrm{K})/\tau_{\mathrm{t}1}(\tilde{\nu}, 300\ \mathrm{K})]}{\Delta t} \tag{3.1}$$

$$\Delta t \equiv t_1 - t_2, \tag{3.2}$$

where $\tau_{\mathrm{t}10}$ and $\tau_{\mathrm{t}1}$ is the transmittance of low/highR-t10 and low/highR-t1 and t_1, t_2 is the sample thickness. The statistical uncertainty of the absorption coefficient $\Delta\alpha_{\mathrm{FTS,stat}}$ is calculated by the error propagation law:

$$\Delta\alpha_{\mathrm{FTS,stat}}(\tilde{\nu}, 300\ \mathrm{K}) = \frac{1}{\Delta t}\sqrt{\left(\frac{\Delta\tau_{\mathrm{t}10}(\tilde{\nu}, 300\ \mathrm{K})}{\tau_{\mathrm{t}10}(\tilde{\nu}, 300\ \mathrm{K})}\right)^2 + \left(\frac{\Delta\tau_{\mathrm{t}1}(\tilde{\nu}, 300\ \mathrm{K})}{\tau_{\mathrm{t}1}(\tilde{\nu}, 300\ \mathrm{K})}\right)^2}. \tag{3.3}$$

We apply the short-term statistical uncertainty to the transmittance uncertainty $\Delta\tau$. The long-term statistical uncertainty is due to the instability of the light source power and this uncertainty is considered to acts as a proportional factor to the transmittance. Therefore we ignore the long-term statistical uncertainty by including the uncertainty into the correction factor $C(\tilde{\nu})$ as a constant term (The correction method is discussed in section 5.1).

Next, we describe the estimation method of the relative absorption coefficient α_{FTS} at 8.5 K. Wavenumber dependence of the α_{FTS} at 8.5 K is calculated as

$$\alpha_{\mathrm{FTS}}(\tilde{\nu}, 8.5\ \mathrm{K}) = -\frac{\ln[\tau_{\mathrm{t}10}(\tilde{\nu}, 8.5\ \mathrm{K})/\tau_{\mathrm{t}1}(\tilde{\nu}, 8.5\ \mathrm{K})]}{\Delta t}. \tag{3.4}$$

Since $\tau_{\mathrm{t}1}(\tilde{\nu}, 8.5\ K)$ is not measured, we transform the equation to evaluate α_{FTS} with measured value:

$$\alpha_{\mathrm{FTS}}(\tilde{\nu}, 8.5\ \mathrm{K}) = -\frac{\ln[\tau_{\mathrm{t}10}(\tilde{\nu}, 8.5\ \mathrm{K})/\tau_{\mathrm{t}1}(\tilde{\nu}, 300\ \mathrm{K})]}{\Delta t} + \frac{\ln[\tau_{\mathrm{t}1}(\tilde{\nu}, 8.5\ \mathrm{K})/\tau_{\mathrm{t}1}(\tilde{\nu}, 300\ \mathrm{K})]}{\Delta t}. \tag{3.5}$$

The second term $\frac{\ln[\tau_{t1}(\tilde{\nu},8.5\text{ K})/\tau_{t1}(\tilde{\nu},300\text{ K})]}{\Delta t}$ is transformed by equation 2.1 as

$$\frac{1}{\Delta t}\ln\left(\frac{\tau_{c2}}{\tau_{r2}}\right) = \ln\left[\frac{(1-R_{c2})^2 e^{-\alpha_{c2}t_2}}{1-R_{c2}^2 e^{-2\alpha_{c2}t_2}}\frac{1-R_{r2}^2 e^{-2\alpha_{r2}t_2}}{(1-R_{r2})^2 e^{-\alpha_{r2}t}}\right]$$
$$= \frac{2}{\Delta t}\ln\left[\frac{1-R_{c2}}{1-R_{r2}}\right] + \frac{1}{\Delta t}\ln\left[\frac{1-R_{r2}^2 e^{-2\alpha_{r2}t_2}}{1-R_{c2}^2 e^{-2\alpha_{c2}t_2}}\right] + (\alpha_{r2}-\alpha_{c2})\frac{t_2}{\Delta t} \quad (3.6)$$
$$\equiv X_1 + X_2 + X_3, \quad (3.7)$$

where subscript "$c2$" shows the value of a thin sample at 8.5K, and "$r2$" shows the value of at 300K for simplification of notation. The R is the Fresnel reflectivity and is expressed with the refractive index (n) as $R = ((n-1)/(n+1))^2$. We assume that the n of CdTe at 20 K and 300 K measured by DeBell et al. (1979) is the same as that of CdZnTe at 8.5 K and 300 K, respectively, since the abundance ratio of Zn to Cd is only $\sim 4\%$ (see section 2.3) and the effect of the 4% Zn abundance on the refractive index is considered to be small. From the refractive index assumption, the X_1 term is calculated as $X_1 = -(8.84 \pm 0.02) \times 10^{-3}$ cm^{-1} at 5–20 μm. Therefore, we ignore X_1 by including X_1 in the correction factor $C(\tilde{\nu})$ as a constant term. When $\alpha_c \leq 3\alpha_r$, X_2 is less than 0.02α, which are negligible compared to systematic error based on calculation ($\Delta\alpha_{\text{calc}} < 0.1\alpha$). Therefore, we can derive the relative wavenumber dependence of absorption coefficients at 8.5 K as follows:

$$\alpha_{\text{FTS}}(\tilde{\nu}, 8.5\text{ K}) = -\frac{1}{t_1}\ln\left[\frac{\tau_{t10}(\tilde{\nu}, 8.5\text{ K})}{\tau_{t1}(\tilde{\nu}, 300\text{ K})}\right] + \frac{t_2}{t_1}\alpha_{\text{FTS}}(\tilde{\nu}, 300\text{ K}). \quad (3.8)$$

The statistical uncertainty of α_{FTS} is calculated by the error propagation law:

$$\Delta\alpha_{\text{FTS}}(\tilde{\nu}, 8.5\text{ K}) = \frac{1}{t_1}\sqrt{\left(\frac{\Delta\tau_{\text{stat,c1}}}{\tau_{\text{c1}}}\right)^2 + \left(\frac{t_1}{\Delta t}\frac{\Delta\tau_{\text{stat,r2}}}{\tau_{\text{r2}}}\right)^2 + \left(\frac{t_2}{\Delta t}\frac{\Delta\tau_{\text{stat,r1}}}{\tau_{\text{r1}}}\right)^2} \quad (3.9)$$
$$\tau_{\text{c1}} \equiv \tau_{\text{t10}}(\tilde{\nu}, 8.5K), \quad \tau_{\text{r1}} \equiv \tau_{\text{t10}}(\tilde{\nu}, 300K), \quad \tau_{\text{r2}} \equiv \tau_{\text{t1}}(\tilde{\nu}, 300K). \quad (3.10)$$

Here we apply the short-term statistical uncertainty to the error $\Delta\tau_{\text{stat}}$. The long-term statistical uncertainty is ignored for the same reason as the case of the α_{FTS} at 300 K.

Figure 3.7 shows the estimated α_{FTS} of the low-resistivity CdZnTe. The relative absorption coefficients become larger at a longer wavelength at both 300 K and 8.5 K. The 10–18 μm relative absorption coefficients at 8.5 K is 1.2–2.2 times larger than that at 300 K. Also, the wavenumber dependence of the absorption coefficient of the low-resistivity CdZnTe is higher at 8.5 K than that at 300 K.

The uncertainty $\Delta\alpha$ derived by the error propagation law is $\Delta\alpha \leq 0.02$ cm^{-1}. The uncertainty is small enough to discuss the low-resistivity CdZnTe absorption factor, although the uncertainty is larger than the requirement (< 0.0025 cm^{-1}).

Figure 3.8 shows the estimated α_{FTS} of the high-resistivity CdZnTe. Both at 300 K and at 8.5 K, the relative absorption coefficients of the high-resistivity CdZnTe are $\alpha_{\text{FTS}} < 0.1$ cm^{-1} and lower than those of low-resistivity one. The relative absorption coefficients are larger at a longer wavelength at both temperatures. The uncertainty is the same as the case of the low-resistivity one ($\Delta\alpha \leq 0.02$ cm^{-1}).

From the FTS measurements, we obtained wavenumber dependence of the relative absorption coefficient of the low/high-resistivity CdZnTe including the systematic uncertainty due to the defocus. At 10–18 μm, the absorption coefficient of the low-resistivity CdZnTe at 8.5 K is > 1.2 times larger than that at 300 K. On the other hand, the absorption coefficients of the high-resistivity CdZnTe is < 0.1 cm^{-1} and lower than those of the low-resistivity one. Since there may be systematic uncertainty based on defocus effect, correction of $\alpha_{\rm FTS}$ is needed to obtain wavenumber dependence of the absolute absorption coefficient (discussed in section 5.1).

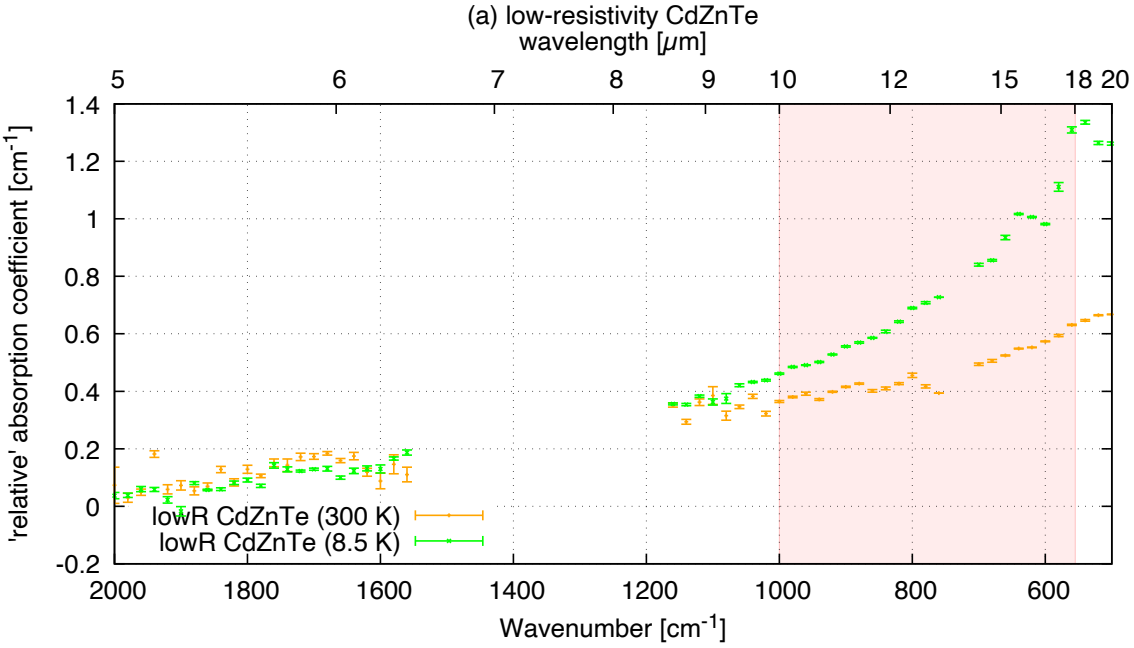

Figure. 3.7 The wavenumber dependence of the relative absorption coefficient of the low-resistivity CdZnTe. We note that there may be systematic uncertainty due to the defocus effect described in section 2.2.2.

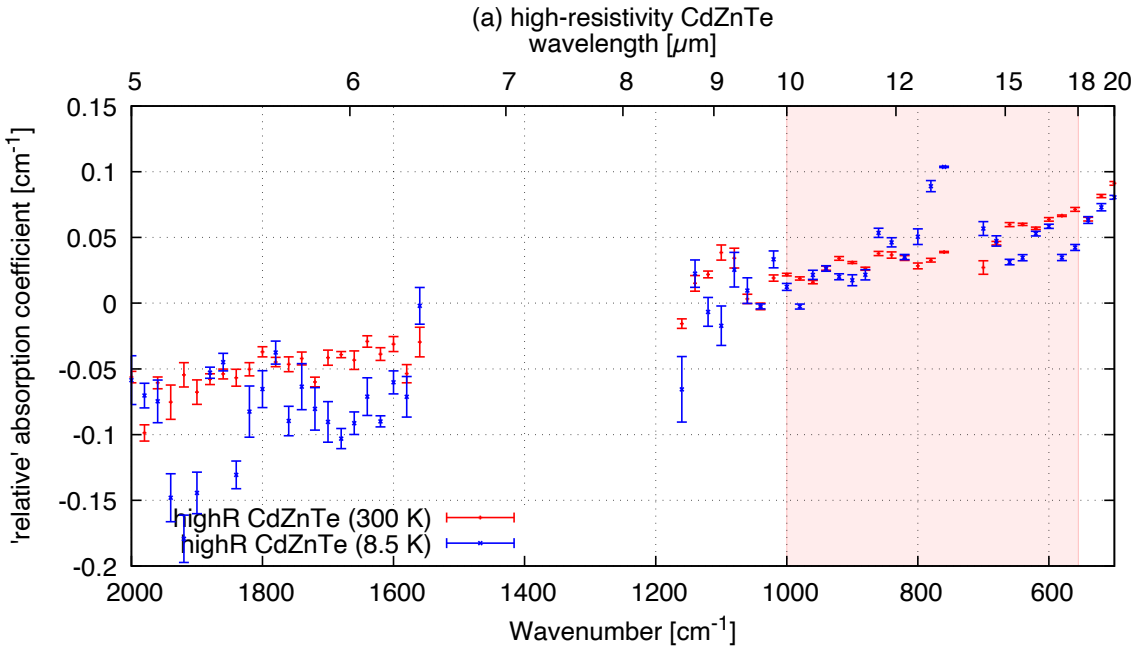

Figure. 3.8 The relative wavenumber dependence of the relative absorption coefficient of the high-resistivity CdZnTe. We note that there may be systematic uncertainty due to the defocus effect described in section 2.2.2.

3.3 Summary of this chapter

In this chapter, we discuss the method of the transmittance measurement with FTSs and the results.

In order to measure the wavenumber dependence of absorption coefficient of CdZnTe at 5–20 μm from room to cryogenic temperature, we measure the transmittance of the four samples with FTS systems. The FTS measurement provides a wavenumber dependence of absorption coefficients, although the measurements yield the defocus error. The cryostat is cooled by continuous liquid helium flow. We measure the transmittance of high/lowR-t10 at cryogenic temperature and at room temperature with an FTS and cryostat system. On the other hand, we measure the transmittance of high/lowR-t1 at room temperature with another FTS in order to measure thickness dependence of the transmittance.

As a cooling result of low/highR-t10, the lowest temperature is 8.5 ± 0.5 K and is lower than the previous study (29 K; Kaji et al. 2016). We can assume that transmittances and absorption coefficients of samples at 4.8 K is the same as the current results at 8.5 K since the transmittance and the absorption coefficient is constant regardless of the temperature at < 50 K (See sections 4.2.2 and 4.2.3), although the temperature does not reach the required temperature (4.8 K).

We derive the transmittance based on the ratio of transmitted light power with and without the sample. The 5–20 μm transmittance of lowR-t10 is $\tau = 0.33$–0.57 and 0.18–0.59 at 300 K and 8.5 K, respectively. We confirm that the lowR-t10 transmittance becomes lower at 10–20 μm with cooling. The 5–20 μm transmittance of lowR-t1 is $\tau = 0.60 - 0.61$. On the other hand, the 5–20 μm transmittance of highR-t10 is $\tau = 0.64 - 0.70$ at both temperatures and that of highR-t1 is $\tau = 0.65 - 0.72$ at 300 K. We confirm that the transmittances of highR-t10/t1 are higher than those of lowR-t10/t1.

From the thickness dependence of the transmittances, we estimate wavenumber dependences of absorption coefficients of the low/high-resistivity CdZnTe. The 10–18 μm absorption coefficient of the low-resistivity CdZnTe is α =0.4–0.6 cm^{-1} at 300 K and become larger (α =0.5–1.4 cm^{-1}) at 8.5 K. On the other hand, the absorption coefficient of the high-resistivity CdZnTe is < 0.1 cm^{-1} both at 300 K and at 8.5 K. The uncertainty $\Delta\alpha$ is estimated as $\Delta\alpha \leq 0.02$ cm^{-1} from the short-term statistical uncertainty. The uncertainty is small enough to discuss the absorption factors in the low-resistivity CdZnTe, although the uncertainty does not meet the requirement.

We note that the absorption coefficient measured with the FTS systems contains systematic uncertainty due to the defocus effect. To correct this uncertainty, we perform another experiment with a collimated beam system (chapter 4).

§4

Experiment 2: Transmittance measurement with a collimated lamp beam and bandpass filters

Since the defocus effect causes systematic errors in the FTS measurements (Section 3), we need absolute calibrations with absolute absorption coefficient measured without the defocus error at several wavelengths. To measure transmittance at several wavelengths without the defocus effect, we construct an original measurement system with a collimated globar lamp and four bandpass filters. Since the beam is well collimated in this system, we expect that the defocus effect is not an issue. Therefore, we can correct the wavenumber dependence of relative absorption coefficient α_{FTS} with the absolute absorption coefficient obtained in this chapter.

Section 4.1 describes the method of measurement with this system. Section 4.2 discusses the results of the measurements.

4.1 Method

The requirement of the experiment is summarized in table 4.1: transmittance measurement with a statistical uncertainty of $\Delta\tau_{\mathrm{col,stat}}/\tau < 0.001$ at 4.8–300 K at two or more bands within 5–20 μm.

Table. 4.1 Requirements of experiment 2

statistical uncertainty	$\Delta\tau_{\mathrm{col,stat}}/\tau < 0.001$
wavelength	two or more bands (within 5–20 μm)
temperature	4.8–300 K

Firstly, we describe an overview of the built measurement system. To measure the transmittance free from the defocus effect, a globar lamp light is collimated and this collimated beam is incident on a sample. The uncertainty due to the defocus effect is negligible since the focus position does not change when the collimated beam is incident on a sample. Also, to measure

the transmittance with high precision, we need to correct the time-variation of the light source power. To correct the instability of the light source, the collimated beam before incidence on a sample is separated into two beams, one of which is incident on the sample and the other is focused on a detector to monitor the power of the incident beam. To cool samples down to cryogenic temperature, Gifford-Mcmahon cryocooler and optical cryostat are used.

We describe details of the optical system to measure transmittance. Figure 4.1 shows the optical path of the measurement system. We used a (1) bench-top stabilized silicon nitride globar light source (SLS303; Thorlabs Inc.), which is 1200 K light source and emit infrared light at 0.55–15 μm. The specifications show that the power fluctuation is $< 0.05\%$/hour and the optical drift is 0.01%/hour and 0.2%/K. The light is focused by an AntiReflective- (AR-) coated ZnSe Lens and (2) an off-axis parabola mirror. We used (3) a polycrystalline infrared (PIR) fiber for two purposes: to limit image size and to make it easier to adjust the position of optics after the fiber. The light from the fiber is collimated by (4) an AR-coated ZnSe lens. To limit wavelength range, (6) a filter wheel with four optical bandpass filters is placed into the optical path. Specifications of the bandpass filters are listed in Table 4.2. The beam is narrowed by (7) an aperture from ϕ10 mm to ϕ2 mm in order to pass through the holder aperture (ϕ5 mm). The beam is relatively faint as $\sim 10^{-5}$ W/cm^2 after the ϕ 2 mm aperture (7). To detect the faint beam, we use (5) an optical chopper with a frequency of $\sim$ 1 kHz (model 300CD; Scitec instruments) and lock-in amplifiers (SR830; Standard Research Systems). Right after the filter wheel, the light is split roughly fifty-fifty by (8) a ZnSe beam splitter. One beam is focused by (12) an AR-coated Ge lens on (13) a Peltier-cooled HgCdTe (MCT) detector (PVMI-4TE-10.6-1x1-TO8-wZnSeAR-35; VIGO system S.A) in order to monitor the time variation of the incident beam power. The other beam passed through a sample and is focused by (16) an AR-coated ZnSe lens on (17) a liquid-nitrogen-cooled (LN_2-cooled) MCT detector (IOH-1064; Bomem inc.) in order to measure the power of the beam through the sample.

Next, we describe the cooling system. To cool a sample at cryogenic temperature, we used a cryostat with a two-stage Gifford-Mcmahon (GM) cryocooler (PS24SS; Nagase & Co., Ltd.). The specification shows that the cooling capability of the cooler is 8.1 W at 20 K and the lowest temperature at no heat load is 4.2 K, which is lower than the requirement (< 4.8 K). In order to reduce radiative heat load from the $\sim$300 K area, (9,10) AR-coated ZnSe windows with thicknesses 5 mm and 1 mm are attached to the vacuum chamber and the radiation shield in the chamber, respectively. The inside of the chamber is pumped with a pressure of $< 10^{-2}$ Pa. A calibrated Si-diode sensor is embedded and monitored the temperature of the cold-head.

Then we discuss prepared sample holders to cool samples at cryogenic temperature. We prepared two types of sample holders, one for thick samples and the other for thin ones (Figure 4.2). A thick sample is held from the side with a slit copper plate and indium sheets to secure a large area of contact between a sample and the holder. The aperture on the incident side is set as ϕ 5 mm. The ϕ8 mm exit-side aperture is wider than the incident-side one to prevent beam-vignetting by the exit aperture. A thin sample is fixed to the holder in the same way as described

in section 3.1. We monitored the temperature of the holders with a Cernox temperature sensor (CX-1030-SD-HT-1.4L; Lakeshore inc.), which is a thin-film resistance sensor calibrated at 1.4–325 K.

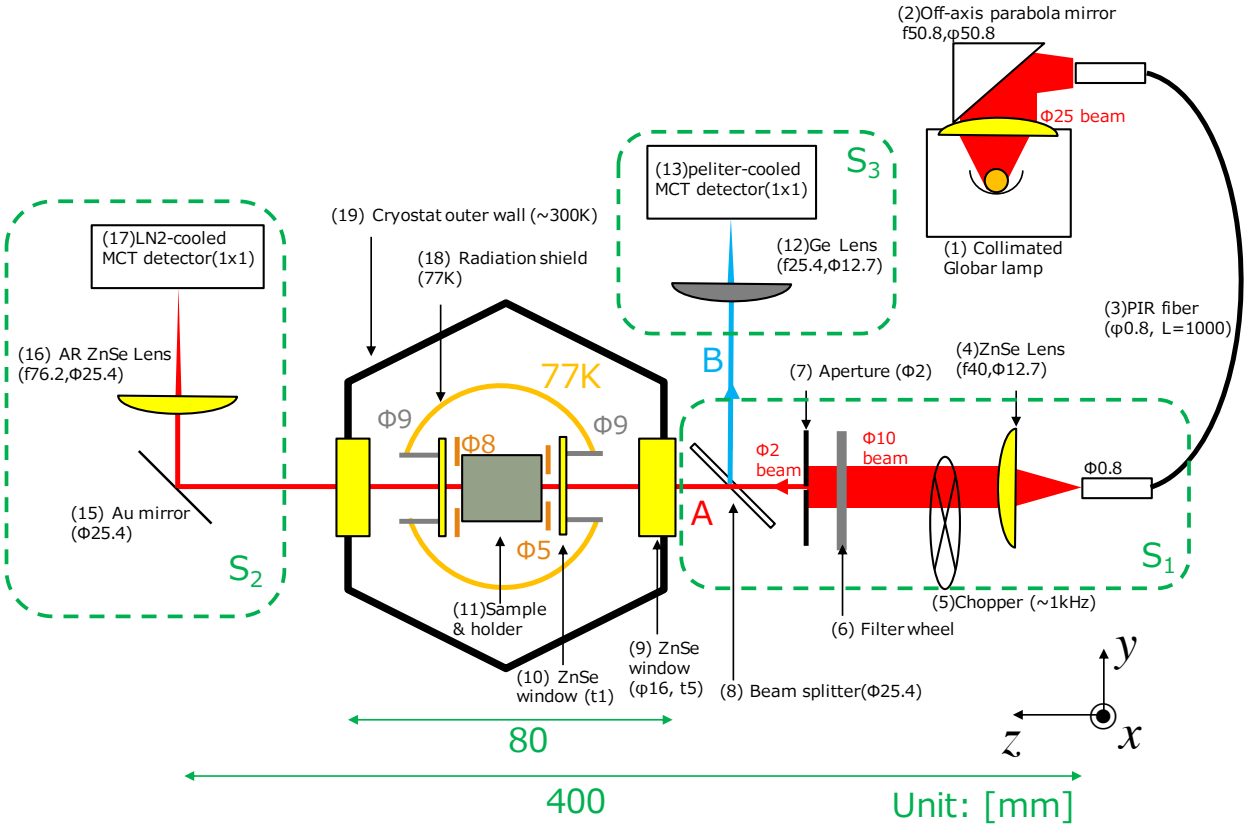

Figure. 4.1 Optical system overview. The stages S_1 and S_2 can move in the x, y direction. The stage S_3 can move in the x, z direction.

Next, we describe our measurement process. We measure the transmittance of all four samples (high/lowR-t10 and high/lowR-t1; Table 2.2) with the four filters shown in Table 4.2 at several temperatures between 4.8–300 K. We control the heater on the cold-head so that the cooling rate is lower than 6 K/min during the cooling and heating process to limit thermal stress on the sample. When we measure transmittance at a certain temperature, we fix the temperature of

Table. 4.2 Specifications of the bandpass filters

name	band center [μm]	FWHM [μm]	nominal transmittance	diameter [mm]	Blocking τ^a
band-6	6.45	0.1	0.80	25.4	$< 10^{-3}$
band-10	10.6	1.5	0.80	25.4	$< 10^{-3}$
band-11	11.6	0.8	0.75	6	$< 10^{-3}$
band-15	15.1	1.2	0.60	25.4	$< 10^{-3}$

a: specification transmittance at wavelength out of the band range.

the cold-head within ±0.1 K by the heater control. During the cooling and heating process, the position of the sample moves by ~ 1 mm due to thermal shrink of the cold head shaft, and the shaft affect the measurement by the aperture vignetting ($\sim 3\%$ of the beam power). Therefore, we realign the position of the stage -S_1, S_2, S_3 in two axis direction vertical to the optical axis at each temperature in order to allow the beam to pass through the center of the holder aperture.

We describe the way of transmittance estimation, including the correction of time variation of light source power. Relative transmitted power corrected for time-variation of light source power is expressed as $\frac{V_A}{V_B}$, where V_A and V_B show powers detected at the same time on (A) the LN_2-cooled MCT detector and on (B) the Peltier-cooled MCT detector. Therefore, the transmittance τ of a sample is calculated as

$$\tau(T) = \frac{V_{A,\mathrm{CZT}}(T)/V_{B,\mathrm{CZT}}(T)}{V_{A,\mathrm{ref}}(T)/V_{B,\mathrm{ref}}(T)}, \tag{4.1}$$

where $V_{X,\mathrm{CZT}}$ $(X = A, B)$ shows the power detected in the case with a sample and $V_{X,\mathrm{ref}}$ shows those without samples. We derive the transmittance from equation 4.1.

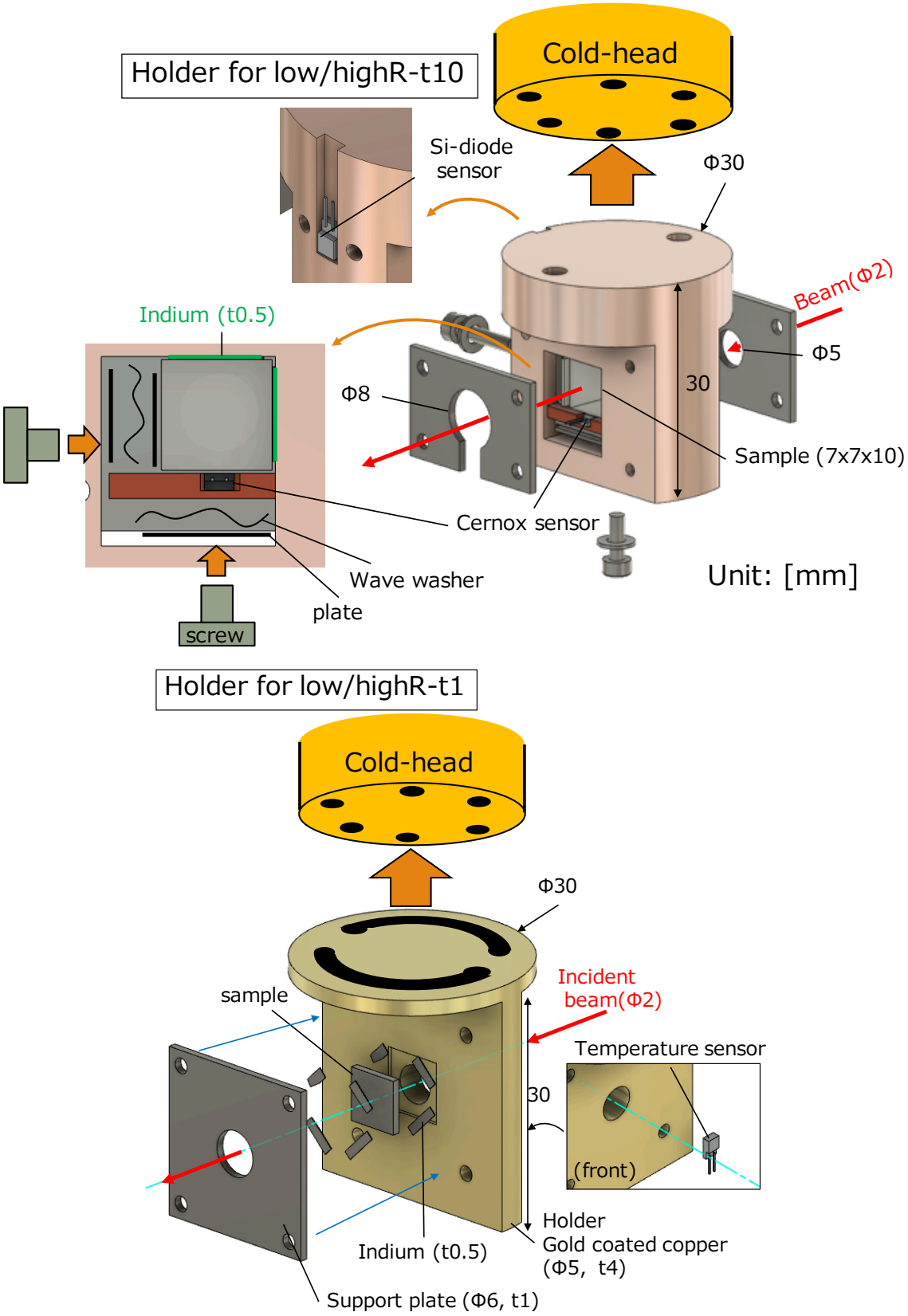

Figure. 4.2 Sample holders for experiment 2. Top: The holder for thick (low/highR-t10) sample. Bottom: The holder for thin (low/highR-t1) sample.

4.2 Results

In this section, we discuss the measurement results: cooling profiles, transmittance and absorption coefficient. Firstly, we compare the requirements and actual measurements. The comparisons of requirements and the actual results are summarized in table 4.3. The derivation of requirements is described in section 2.2.3. Details of the actual results are described in the following sections. Section 4.2.1 describes the cooling profile of this measurement system. In section 4.2.2, we describe the transmittance measurement results. Section 4.2.3 describes the absorption coefficient derived from the measured transmittances.

Table. 4.3 The requirement and actual result of experiment 2.

	requirement	actual result
short-term statistical uncertainty $\Delta\tau_{\mathrm{col,stat}}/\tau$	$< 10^{-3}$	$\leq 8 \times 10^{-4}$
statistical uncertainty due to reproducibility $\Delta\tau_{\mathrm{col,rep}}/\tau$	–	0.011
$\Delta\alpha$ [cm^{-1}]	$< 2.5 \times 10^{-3}$	0.016
minimum temperature T_{min}	< 4.8 K	8.6 ± 0.1 K

4.2.1 Cooling performance

Figure 4.3 shows the transition of temperatures at cold-head, side of the holder and highR-t10 sample. The lowest temperature achieved of the sample is 8.6 K. The current study achieved the measurements at temperatures lower than those of the previous study (Kaji et al. 2016), but the achieved temperatures did not meet the requirement of ≤ 4.8 K.

Then we discuss the temperature uncertainty of the sample. Possible factors of the uncertainty ΔT are the uncertainty of the sensor calibration, the accuracy of measurement by the temperature monitor, the uncertainty due to Seebeck effect, and the scattering of the measured value. The uncertainty of the sensor calibration is negligible because the sensor is well-calibrated ($\Delta T < 30$ mK). The standard deviation of the measured temperature is the largest at 300 K and it is < 0.4 K. Since each temperature is measured more than 100 times, we can ignore the uncertainty due to scattering of the measured value by averaging ($\Delta T < 0.4/\sqrt{100} = 0.04$ K). Therefore, the uncertainty ΔT is evaluated from the error due to the Seebeck effect $\Delta T_{\rm Se}$ and from the accuracy guaranteed by the temperature monitor $\Delta T_{\rm moni}$. We calculated the total temperature error $\Delta T_{\rm tot}$ as

$$\Delta T_{\rm tot} = \Delta T_{\rm moni} + \Delta T_{\rm Se}. \tag{4.2}$$

The error due to the Seebeck effect $\Delta T_{\rm Se}$ are dominant at cryogenic temperature and evaluated by the polarity switching method as $\Delta T_{\rm Se} = 0.1$ K at 8.6 K. The specification accuracy of resistance R_o measured by the temperature monitor is $\Delta R_{o,\rm moni} = \pm 0.8\ \Omega \pm 0.0004 R_o$ and the equivalent temperature accuracy is $\Delta T_{\rm moni} = 10$, 5, 2, 1, 0.3, 0.05 K at $T = 300$, 200, 100, 50, 8.6 K, respectively. Therefore, the temperature uncertainties are $\Delta T = 0.1$ K at cryogenic temperature and $\Delta T = 10$ K at room temperature.

Samples are cooled down to 8.6±0.1 K, which is a lower temperature than the previous study (29 K; Kaji et al. 2016). We can estimate the absorption coefficient of the low-resistivity CdZnTe at 4.8 K from that at 8.5 K, although the temperature does not meet the temperature requirement (4.8 K). This is because the temperature dependence of the absorption coefficient at < 50 K is negligibly small (see section 4.2.3).

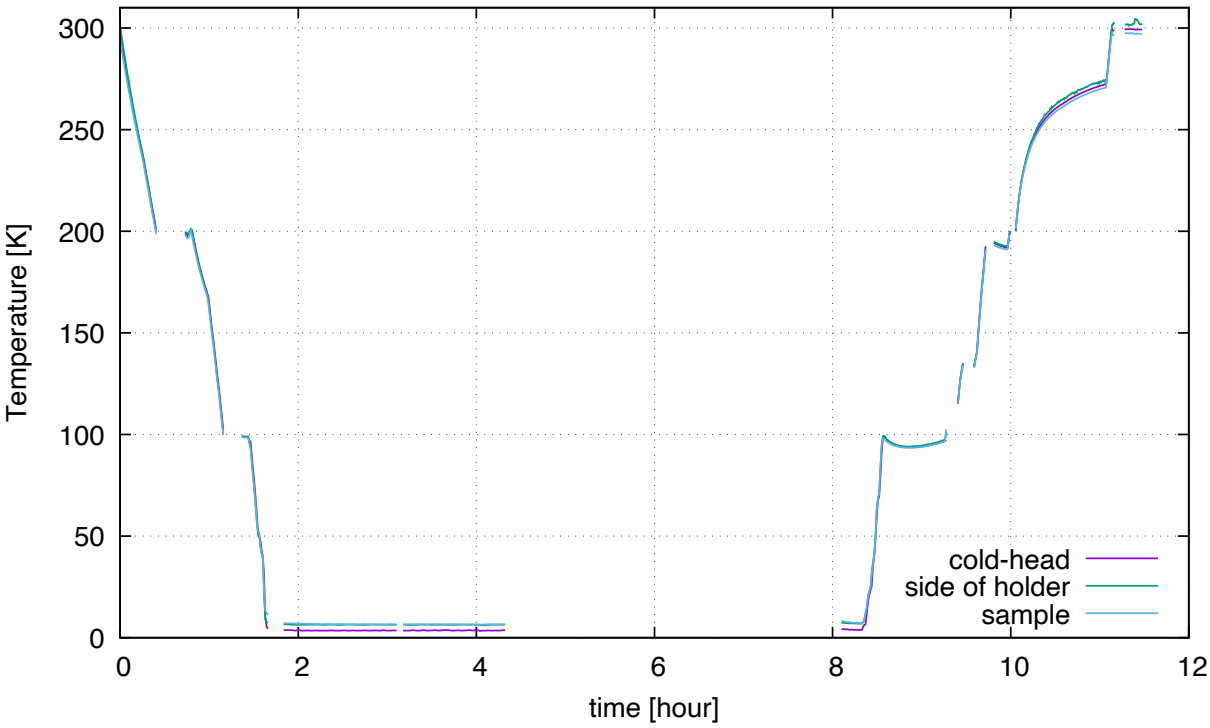

Figure. 4.3 Temperature profiles at cold-head, holder and highR-t10 sample. Temperature of the cold head cooled down to 3.9±0.1 K and those of holder and samples to 8.6±0.1 K.

4.2.2 Transmittance

Here we describe the transmittance measurement results. Transmittances are estimated with equation 4.1. We apply normalized reference $V_{A,\mathrm{ref}}(T)/V_{B,\mathrm{ref}}(T) = V_{A,\mathrm{ref}}(300\ K)/V_{B,\mathrm{ref}}(300\ K)$ to the case at all the measured temperatures, since the difference between the normalized references at 300 K and that at 8.5 K is $\sim 0.4\%$ of them and is within an uncertainty range due to reproducibility described below (1.1%) and there is no significant change in the normalized reference with temperature.

The upper view of Figure 4.4 shows the measured transmittance of lowR-t1 at 6.45, 10.6, 11.6 and 15.1 μm at 8.6–300 K. The transmittances of lowR-t1 are $\tau = 0.6 - 0.65$ and does not change with temperature and with wavelength.

The bottom view of Figure 4.4 shows the measured transmittance of lowR-t10 at 6.45, 10.6, 11.6 and 15.1 μm at 8.6–300 K. The transmittances are $\tau = 0.35 - 0.43$ at 300 K and $\tau = 0.26 - 0.40$ at 8.6 K. The τ is lower at the longer wavelength at all measured temperature ranges. The τ at 6.45 and 10.6 μm have their peaks at 100 K. At 50–100 K, the τ at the four wavelengths decrease with cooling. The temperature dependence of the τ is negligibly small at < 50 K. The transmittance becomes 4–10% lower at 8.6K than that at 300K at all four wavelengths.

We evaluate the uncertainty to check whether it meets the requirement. First, the short-term statistical uncertainty is smaller than the requirement ($\Delta\tau_{\mathrm{col,stat}}/\tau < 8 \times 10^{-4}$) with integration time of ~ 10 minutes.

Then, we discuss the statistical uncertainty due to reproducibility $\Delta\tau_{\mathrm{col,rep}}$. We measure the transmittance of lowR-t1 before and after cooling cycle at 300 K at each band $(\tau_{\mathrm{before}}(\lambda_i, 300K), \tau_{\mathrm{after}}(\lambda_i, 300K))$ to evaluate the reproducibility. Each measurement is performed once. To evaluate the reproducibility, we set parameter Q_i as follows:

$$Q_i = \frac{\tau_{\mathrm{before}}(\lambda_i, 300K) - \tau_{\mathrm{after}}(\lambda_i, 300K)}{(\tau_{\mathrm{before}}(\lambda_i, 300K) + \tau_{\mathrm{after}}(\lambda_i, 300K))/2} \tag{4.3}$$

$$\lambda_i = 6.45, 10.6, 11.6, 15.1\ \mu\mathrm{m} \quad (i = 1, 2, 3, 4). \tag{4.4}$$

The mean of the four $|Q_i|$ is $\overline{|Q|} = 0.012$ and the standard deviation of Q_i is 0.0075. If we assume that a measured transmittance follows the normal distribution of with the variance of $\Delta\tau^2_{\mathrm{col,rep}}$ and the mean μ_τ, the expected value of the $\overline{|Q|}$ is derived as follows:

$$\overline{|Q|}_{\mathrm{exp}} = \int_{-\infty}^{\infty} |x| \frac{1}{\sqrt{2\pi(\sigma_2/\mu_\tau)^2}} \exp\left(-\frac{x^2}{2(\sigma_2/\mu_\tau)^2}\right) dx = \frac{\sqrt{2}}{\sqrt{\pi}}\sigma_2/\mu_\tau. \tag{4.5}$$

Here, $\sigma_2^2 = 2\Delta\tau^2_{\mathrm{col,rep}}$ is the variance of the population of the $\tau_{\mathrm{before}} - \tau_{\mathrm{after}}$. We assume that the variance of the population of the Q_i is $(\sigma_2/\mu_\tau)^2$ for simplicity since the scattering of Q_i is dominantly caused by the numerator of the Q_i (equation 4.3). Therefore, the uncertainty due to reproducibility at 300 K is estimated as $\Delta\tau_{\mathrm{col,rep}}/\tau = \frac{\sqrt{\pi}}{2}\overline{|Q|} = 0.011$. This uncertainty due to reproducibility is considered to be caused by manual alignment precision. We realigned the

optical system manually at each temperature because the sample position moved by ~ 1 mm due to thermal shrink of the cold head shaft and the beam center shifts from the aperture center of the sample holder (ϕ 5 mm). The realignment procedure is needed because detected beam power decrease by $\sim 3\%$ from 300 K to 8.6 K by vignetting without the realignment. The detected power (I) changes depending on the S_2 stage displacement (x) as $(dI/dx)/I \sim 0.5\%/10$ μm around the peak position, and the manually possible minimum adjustment displacement of the S_2 position is the order of ~ 10 μm. Therefore, the reproducibility is considered to be due to the manual alignment precision. We assume that the reproducibility is common for all cases (temperatures, wavelength bands and samples), since we perform the alignment in the same way. Then, we apply the uncertainty due to the reproducibility $\Delta\tau_{\rm rep,col}/\tau = 0.011$ to all the measured cases.

The top view of Figure 4.5 shows the measured transmittance of highR-t1 at the four wavelengths at 8.6–300 K. The uncertainty is the same as the lowR-t10/t1 case. The transmittance range is $\tau = 0.61 - 0.69$. The transmittance at 15.1 μm increases from $\tau = 0.64$ to $\tau = 0.67$ with cooling and those at the other wavelength are roughly constant at all the measured temperatures.

The bottom view of Figure 4.5 shows the measured transmittance of highR-t10 at the four wavelengths at 8.6–300 K. The evaluation method of the uncertainty is the same as the lowR-t10/t1 case. The transmittance range is $\tau = 0.61 - 0.69$, which is the same as the highR-t1 case. The transmittance at 15.1 μm increase from $\tau = 0.64$ to $\tau = 0.67$ with cooling and that at 11.6 μm decrease from $\tau = 0.67$ to 0.61. The transmittances at 6.45 and 10.6 μm are roughly constant at all the measured temperatures.

Following the above discussion, the current result shows that the transmittance of lowR-t10 decreases with temperature and that the transmittance change of highR-t10 with temperature is smaller than that of lowR-t10.

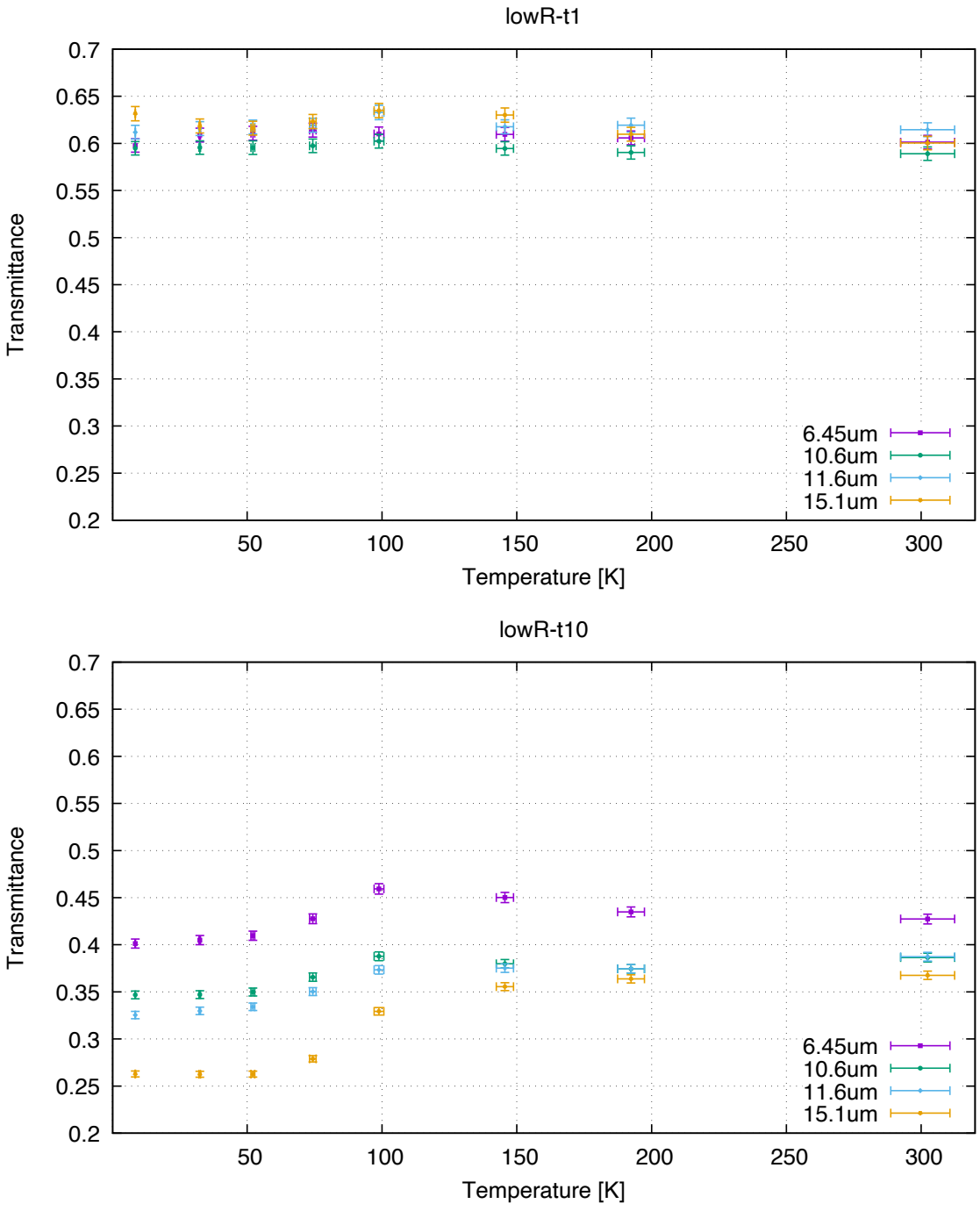

Figure. 4.4 The measured transmittance of lowR-t1 (top) and lowR-t10 (bottom). Vertical error bars denote the reproducibility $\Delta\tau_{\mathrm{col,rep}}$, and horizontal ones denote the temperature uncertainty ΔT.

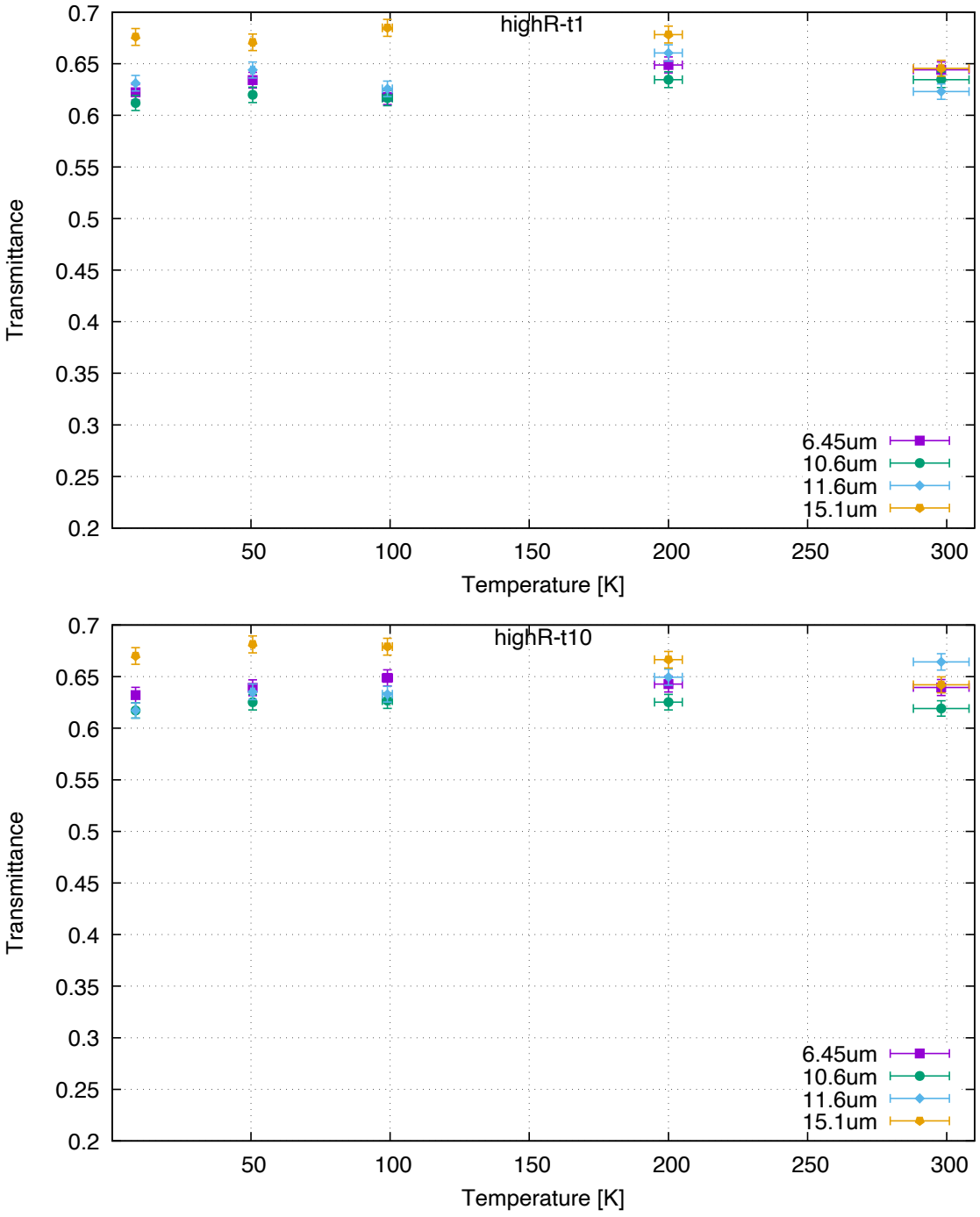

Figure. 4.5 The measured transmittance of highR-t1 (top) and highR-t10 (bottom). Vertical error bars denote the reproducibility $\Delta\tau_{\mathrm{col,rep}}$, and horizontal ones denote the temperature uncertainty ΔT.

4.2.3 Absorption coefficient

To correct relative wavenumber dependence of the absorption coefficient calculated in section 3.2.3, we derive the absorption coefficient from the transmittance (τ_1, τ_2) of samples with different thickness (t_1, t_2) measured with the collimated beam system as follows:

$$\alpha(\tilde{\nu}, T) = -\frac{\ln[\tau_1(\tilde{\nu}, T)/\tau_2(\tilde{\nu}, T)]}{t_1 - t_2}. \tag{4.6}$$

The statistical uncertainty $\Delta\alpha$ is evaluated by the error propagation of the transmittance uncertainty.

$$\Delta\alpha(\tilde{\nu}, T) = \frac{1}{t_1 - t_2}\sqrt{\frac{\Delta\tau^2_{\mathrm{col,rep}}}{\tau_1(\tilde{\nu}, T)^2} + \frac{\Delta\tau^2_{\mathrm{col,rep}}}{\tau_2(\tilde{\nu}, T)^2}}. \tag{4.7}$$

We ignored errors of the sample thickness because the thickness error is ~ 0.01 mm equivalent to $\Delta\alpha = 0.001\alpha$. The systematic uncertainty due to calculation method $\Delta\alpha_{\mathrm{calc}}$ is discussed in section 5.1.

Figure 4.6 shows the temperature dependence of absorption coefficient of the low-resistivity CdZnTe. The $\Delta\alpha$ is evaluated as $\Delta\alpha = 0.016$ cm^{-1} from the $\Delta\tau_{\mathrm{col,rep}}/\tau = 0.011$. The absorption coefficients are $\alpha = 0.35 - 0.5$ cm^{-1} at 300 K and $\alpha = 0.4 - 0.9$ cm^{-1} at 8.6 K. At 100-300 K, the absorption coefficient at 6.45 μm decreases and that at 15.1 μm increases at lower temperatures. The absorption coefficient increases at all four wavelengths at 50–100 K and becomes roughly constant at < 50 K. The absorption coefficient of low-resistivity CdZnTe is larger at the longer wavelength in all over the temperature range between 8.5 and 300 K.

Figure 4.7(b-1) shows the absorption coefficient of the high-resistivity CdZnTe derived with equation 4.6. The uncertainty $\Delta\alpha = 0.016$ cm^{-1} is the same as that of the low-resistivity one. We note that the true value of the absorption coefficient physically should not be negative. All the α except for $\alpha(11.6\ \mu\mathrm{m}, 300\ \mathrm{K})$ and $\alpha(6.45\ \mu\mathrm{m}, 100\ \mathrm{K})$ are within 3-σ range around 0 cm^{-1} and are neither significantly above zero nor significantly below zero at the 3-σ level. The $\alpha(11.6\ \mu\mathrm{m}, 300\ \mathrm{K}) = -0.070 \pm 0.016$ cm^{-1} and $\alpha(6.45\ \mu\mathrm{m}, 100\ \mathrm{K}) = -0.053 \pm 0.016$ cm^{-1} are out of the 3-σ range around 0 cm^{-1}, but they are within the 4.4-σ range. We assume that all the measured α are neither significantly above zero nor below zero, since they are within the 5-σ uncertainty range (± 0.08 cm^{-1}) around 0 cm^{-1}.

Figure 4.7(b-2) shows the 5-σ upper limit of the absorption coefficient of the high-resistivity CdZnTe. The upper limit of the α are estimated as $\alpha + 5\Delta\alpha = \alpha + 0.08$ cm^{-1} for $\alpha \geq 0$ cm^{-1} cases, and as $5\Delta\alpha = 0.08$ cm^{-1} for $\alpha < 0$ cm^{-1} cases, since the true value of the α is physically not negative. The absorption coefficients of the high-resistivity CdZnTe are $\alpha < 0.11$ cm^{-1} at all the measured temperatures. The α of the high-resistivity CdZnTe is lower than that of the low-resistivity one at all the measured wavelengths and temperatures.

Following the above discussion, our result shows that the low-resistivity CdZnTe has larger absorption coefficient ($\alpha = 0.4 - 0.9$ cm^{-1}) at 8.6 K than those at 300 K ($\alpha = 0.35 - 0.5$ cm^{-1}).

On the other hand, the high-resistivity CdZnTe has lower absorption coefficient than those of the low-resistivity one at all temperature and wavelength cases, and only the upper limit of the absorption coefficient can be obtained ($\alpha < 0.11$ cm^{-1}).

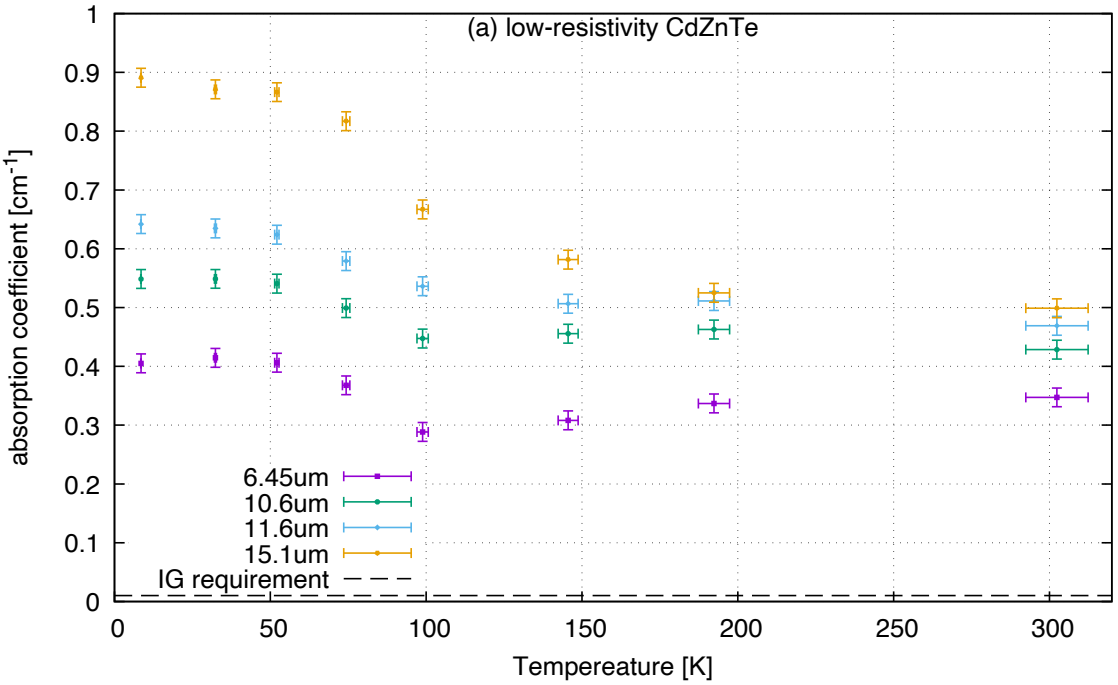

Figure. 4.6 The measured absorption coefficient of the low resistivity CdZnTe . Vertical error bars denote the statistical uncertainty derived from the reproducibility. Horizontal error bars denote the temperature uncertainty. A dashed line shows the absorption coefficient requirement for IG.

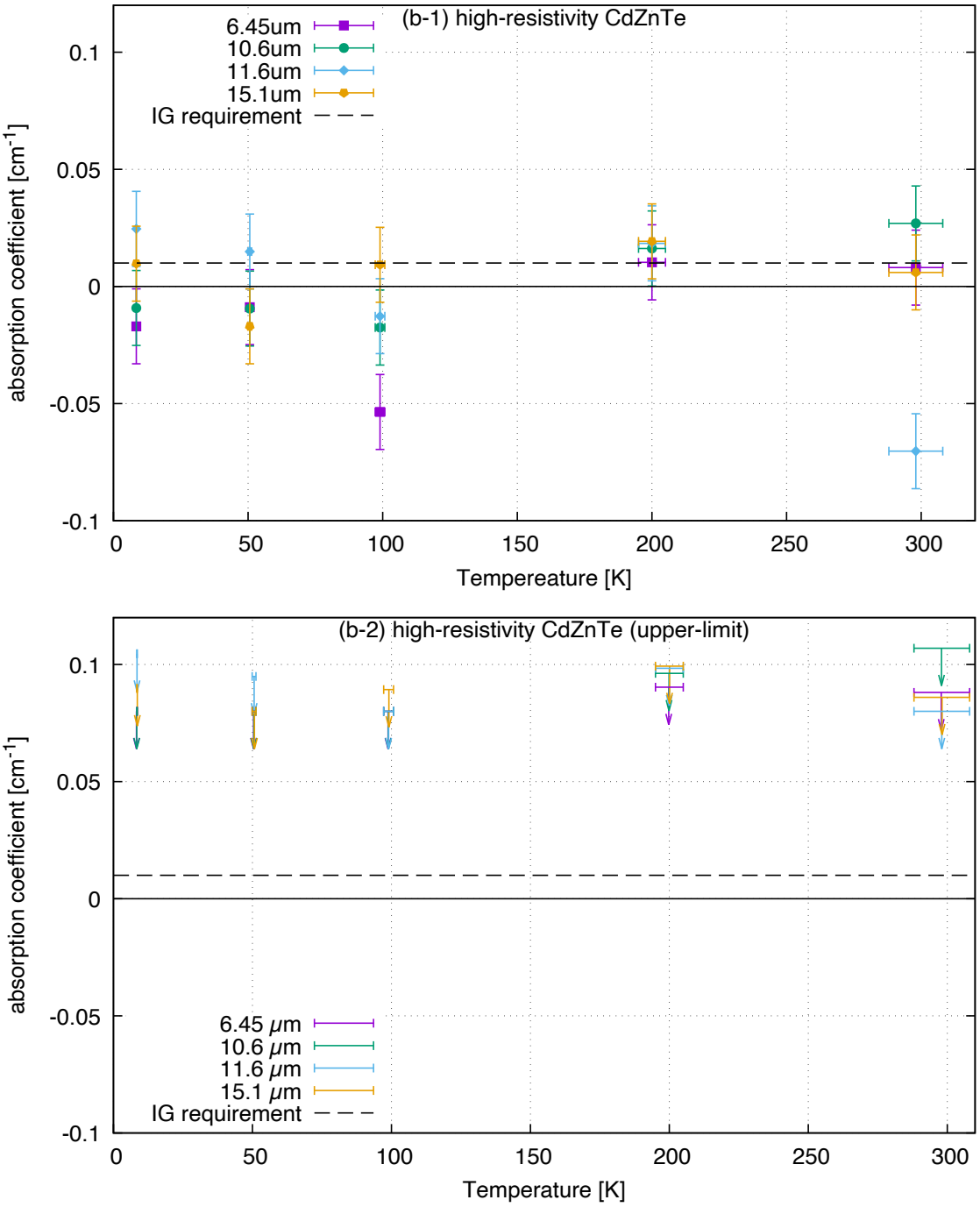

Figure. 4.7 The measured absorption coefficient of the high-resistivity CdZnTe. (b-1) the derived value of the α with equation 4.6. Vertical error bars denote the statistical uncertainty derived from the reproducibility. Horizontal error bars denote the temperature uncertainty. The dashed line shows the absorption coefficient requirement for IG. We note that the true value of the α should be zero or more physically. (b-2) The 5-σ upper limit of the α of the high-resistivity CdZnTe.

4.3 Summary of this chapter

In this chapter, we describe the method and the result of the absorption coefficient measurement with a collimated beam system.

To measure transmittance at several wavelengths without the defocus effect, we construct an original measurement system with a collimated globar lamp beam and four bandpass filters. We use four bandpass filters (6.45, 10.6, 11.6 and 15.1 μm) to limit the wavelength of the beam incident on a sample. Samples are cooled by a cryostat with a Gifford-Mcmahon cryocooler.

As a cooling result, the lowest temperature is 8.6 ± 0.1 K, which is lower than the previous study (29 K; Kaji et al. 2016). We can assume that the absorption coefficients of samples at 4.8 K are the same as those at 8.6 K since the temperature dependence of the α is small at < 50 K, although the temperature does not reach the requirement (4.8 K).

We derive the transmittance based on the ratio of transmitted light power with and without the sample with correction of the time variation of the incident beam power. The transmittances of lowR-t1 are $\tau = 0.6 - 0.65$ and roughly constant at all the measured temperatures. The transmittance of lowR-t10 is τ =0.35–0.43 at 300 K and τ =0.26–0.40 at 8.6 K at four wavelengths. On the other hand, the transmittance of highR-t10/t1 is $\tau = 0.61 - 0.69$ at all four wavelengths at all temperatures. We confirm that the transmittances of highR-t10 are higher than those of lowR-t10 at all four wavelengths.

From the thickness dependence of the transmittances, we derive the absorption coefficients of the low/high-resistivity CdZnTe. The absorption coefficients of the low-resistivity CdZnTe are $\alpha = 0.35 - 0.5$ cm^{-1} at 300 K and $\alpha = 0.4 - 0.9$ cm^{-1} at 8.6 K. On the other hand, we obtain the 5-σ upper limit of the absorption coefficient of the high-resistivity CdZnTe of $\alpha < 0.11$ cm^{-1} at all the measured temperatures.

The uncertainty of the absorption coefficient is $\Delta\alpha$ =0.016 cm^{-1}, which is caused by the reproducibility of the manual alignment. This uncertainty is small enough to discuss the absorption factors in the low-resistivity CdZnTe, although the uncertainty is larger than the requirement ($\Delta\alpha < 0.0025$ cm^{-1}).

To summarize the results, the low-resistivity CdZnTe has a larger absorption coefficient ($\alpha = 0.4 - 0.9$ cm^{-1}) at 8.6 K than those at 300 K ($\alpha = 0.35 - 0.5$ cm^{-1}). On the other hand, the high-resistivity CdZnTe has lower absorption coefficient than those of the low-resistivity one at all temperature and wavelength cases, and only the upper limit of the absorption coefficient can be obtained ($\alpha < 0.11$ cm^{-1}). By using the absorption coefficient measured with the collimated beam system, we can correct the wavenumber dependence of the absorption coefficient obtained with FTS measurements (See section 5.1).

§5

Discussion

This chapter describes discussions based on the results derived from the above two experiments. The results from the two experiments are combined to provide wavenumber dependence of absolute absorption coefficients without the defocus error in section 5.1. In section 5.2, we discuss factors causing infrared absorption in CdZnTe. Section 5.3 discusses the applicability of the low/high-resistivity CdZnTe and the requirement of the resistivity of CdZnTe for an IG material.

5.1 Combination of the two experiments

To obtain wavenumber dependence of absorption coefficients of the low/high-resistivity CdZnTe without the defocus error, we combine the result of the two experiments. The measurements with FTS (experiment 1; chapter 3) provides wavenumber dependence of relative absorption coefficients $\alpha_{\mathrm{FTS}}(\tilde{\nu})$ with systematic uncertainty due to defocus effect. The measurements with the collimated beam (experiment 2; chapter 4) provide absolute absorption coefficients α_{col} at limited wavelength bands. By correcting the systematic uncertainty of α_{FTS} with α_{col}, we obtain absolute absorption coefficient with over a broad wavenumber range (5–20 μm).

First, we evaluate light power loss at the detector as a function of the refractive index of a sample in order to estimate the correction factor due to the defocus of the beam. To compare the size of the detector and beam, we calculated the beam size D_1 at the detector position, considering the geometrical optics. Figure 5.1 shows an optical path after the sample compartment in the reference measurement case and in the sample measurement case. We set symbols as follows:

- n: the refractive index of the sample
- t: the thickness of a sample
- d_0: image size at sample incidence plane
- f: focal length of the ellipsoidal mirror
- d, d_1: image size at the focus position without and with a sample, respectivley

- p, p_1: the distance between the ellipsoidal mirror and image before the mirror without and with a sample, respectively
- q, q_1: the distance between the ellipsoidal mirror and image after the mirror without and with a sample, respectively
- F, F_1: F-number without and with a sample (=(p or p_1)/(beam size at the mirror)), respectively

The beam size D_1 is derived from the following equations:

$$D_1 = d_1 + \frac{|q - q_1|}{F_1} \tag{5.1}$$

$$d_1 = \frac{q_1}{p_1} d_0 \tag{5.2}$$

$$F_1 = \frac{q_1}{p_1} F_0 \tag{5.3}$$

$$p_1 = p - t + t/n \tag{5.4}$$

$$q_1 = \frac{p_1 f}{p_1 - f}. \tag{5.5}$$

Then, D_1 is derived as follows:

$$D_1 = \frac{f}{p_1 - f} d_0 + \frac{p_1(1 - q/f) + q}{F_0} \tag{5.6}$$

$$p_1 = p - t + t/n. \tag{5.7}$$

We assume that $p = 281$ mm, $q = 41$ mm, $f = 35.8$ mm, $F = 3.73$ and $d_0 = 2$ mm based on Figure 4.7 in the vertex 70v manual.

To evaluate the wavenumber dependence of $D_1(\tilde{\nu})$, we discuss the wavenumber dependence of the refractive index. The refractive index of CdZnTe at $\lambda > 6$ μm has not been measured. Thus, we assume wavenumber dependence of the refractive index of CdTe is the same as that of CdZnTe (DeBell et al. 1979), since the abundance ratio of Zn to Cd is only $\sim 4\%$ and the 4% Zn contribution to the refractive index is considered to be small. DeBell et al. (1979) measured the refractive index of CdTe at 300 K at 6–22 μm and obtained the coefficients of the Sellmeier equation, which is an empirical relation between refractive index and wavelength:

$$n(\mathrm{CdTe})^2 - 1 = \frac{A_1 \lambda^2}{\lambda^2 - \lambda_1^2} + \frac{A_2 \lambda^2}{\lambda^2 - \lambda_2^2} \tag{5.8}$$

$$A_1 = 6.197,\ A_2 = 3.224, \tag{5.9}$$

$$\lambda_1^2 = 0.1005\ \mu\mathrm{m}^2,\ \lambda_2^2 = 5279\ \mu\mathrm{m}^2 \quad (300\ \mathrm{K};\ \text{Debell et al. 1979}). \tag{5.10}$$

Here, we estimate the uncertainty of the refractive index caused by applying the CdTe value. The refractive index of CdZnTe is measured at 1–6 μm by Quijada & Henry (2007). We evaluate the uncertainty of the refractive index as $\Delta n = \pm 0.01$ at 300 K from the difference of refractive index at 6 μm between CdZnTe (2.67; Quijada & Henry 2007)and CdTe (2.68; DeBell et al. 1979).

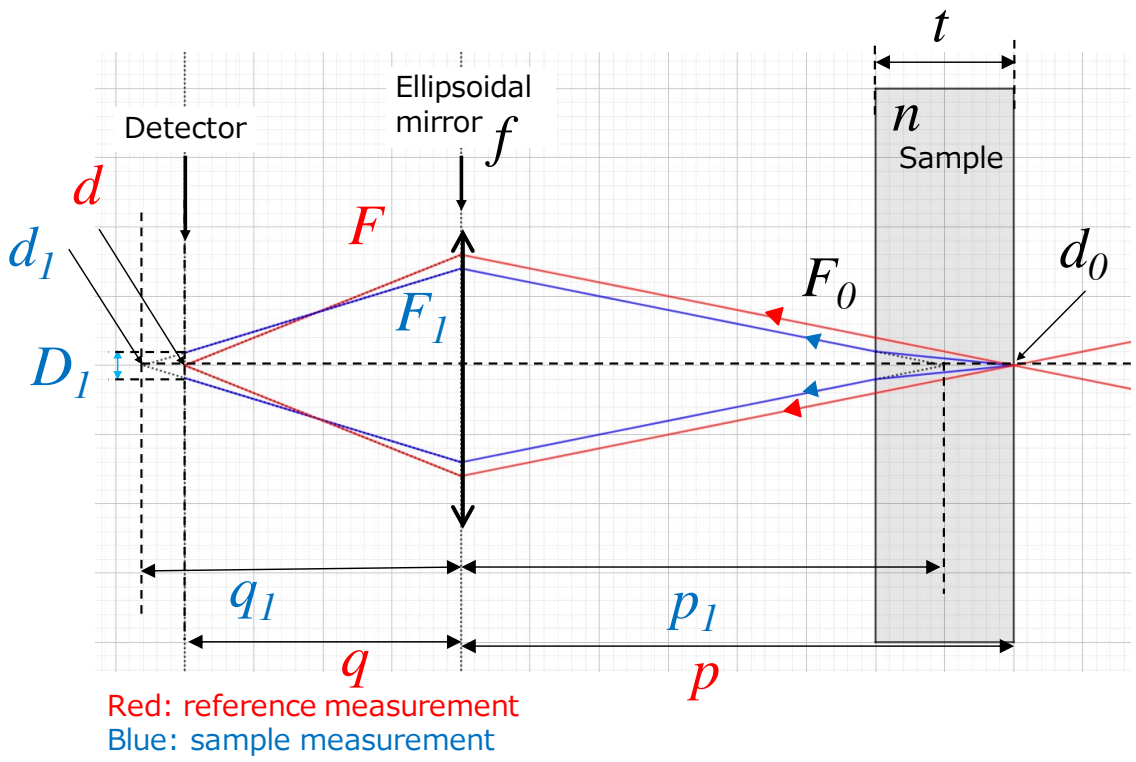

Figure. 5.1 Geometrical optics diagram after a sample position in the FTS. Red lines show the optical path without sample and the blue ones show that with the sample. The aspect ratio in the figure is different from the actual one.

From the estimated beam size $D_1(\tilde{\nu})$, we estimate the light power loss due to the defocus. We assume the beam shape is expressed as a Gaussian function with a beam diameter of D_1, that is $\sigma^2 = (D_1/2)^2$. The relative power P captured by the 1×1 mm^2 detector is expressed as

$$P = \int_{-1/2}^{1/2}\int_{-1/2}^{1/2} \exp\left(-\frac{x^2+y^2}{2\sigma^2}\right) dxdy \propto \left[\mathrm{erf}\left(\frac{1}{\sqrt{2}}\left[\frac{D_1}{1\ \mathrm{mm}}\right]^{-1}\right)\right]^2 \tag{5.11}$$

$$\mathrm{erf}(x) \equiv \frac{2}{\pi}\int_0^x \exp(-t^2)\, dt. \tag{5.12}$$

Therefore, correction factor $C_{1,2}$ can be assumed as

$$C_{1,2} = \frac{\ln(P_1/P_2)}{t_1 - t_2}, \tag{5.13}$$

where P_1 and P_2 are relative powers calculated for thick and thin samples. Figure 5.2 shows the simulation of the correction factor and fitted linear function. The difference between the simulated factor and the fitted linear function is within ± 0.002 cm^{-1}. Thus, the uncertainty due to the approximation of the correction factor is estimated as < 0.002 cm^{-1}.

Following the above discussion, we express the relation between the absorption coefficients from FTS measurement (α_{FTS}) and that from the collimated beam measurement (α_{col}) in the

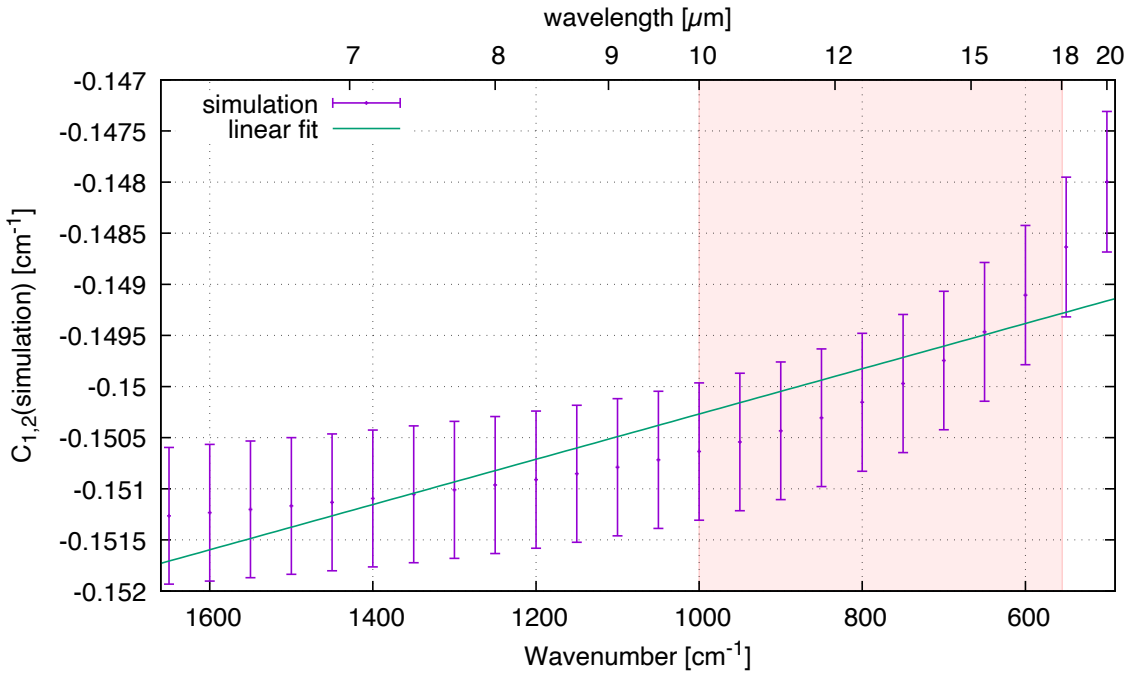

Figure. 5.2 Estimation of defocus loss. The uncertainty is evaluated from the 6 μm refractive index difference between CdTe and CdZnTe ($\Delta n = 0.01$).

following equation:

$$\overline{\alpha_{\mathrm{FTS}}(\tilde{\nu}_i)} = \alpha_{\mathrm{col}}(\tilde{\nu}_i) + a\tilde{\nu}_i + b \tag{5.14}$$

$$\tilde{\nu}_i = 1/\lambda_i \quad \lambda_i = 6.45,\ 10.6,\ 11.6,\ 15.1\ \mu\mathrm{m}\ (i = 1, 2, 3, 4), \tag{5.15}$$

where a and b are free parameters for each sample at each temperature. $\overline{\alpha_{\mathrm{FTS}}(\tilde{\nu}_i)}$ is the averaged value of α_{FTS} over the FWHM wavelength range of $\tilde{\nu}_i$ filter. The uncertainty of $\overline{\alpha_{\mathrm{FTS}}(\tilde{\nu}_i)}$ is derived from the error propagation law.

Using equation 5.14, we derive coefficients a and b for the low-resistivity CdZnTe case by the weighted least squares method. The fitted result is listed in Table 5.1 and shown in Figure 5.3. The ρ_{ab} in Table 5.1 is the correlation coefficient between a and b. The reduced-χ^2 of the low-resistivity CdZnTe are 0.9 at 300 K and 1.5 at 8.5 K. The factor $a\tilde{\nu} + b$ is between -0.25 and 0.08 cm^{-1} at 6–20 μm although that predicted from geometric optics $C_{1,2}$ is between -0.152 and -0.147 cm^{-1}. Since the range of the obtained correction factor is wider than that of the predicted value, the approximation to derive the predicted value may be too rough. We suspect that the difference between the obtained and predicted correction factor is probably caused by the change of the illumination pattern to the detector due to the interference beam or by spacial non-uniformity in the sensitivity of the single detector, although the cause is not clear. Although the correction factor by the defocus effect may be more complex, the general trend of the $\alpha_{\mathrm{FTS}} - \alpha_{\mathrm{col}}$ is fitted by a linear function. Therefore, we set the linear functions as the correction factor.

Then, we evaluate the upper limit of the correction factor for the high-resistivity case, since

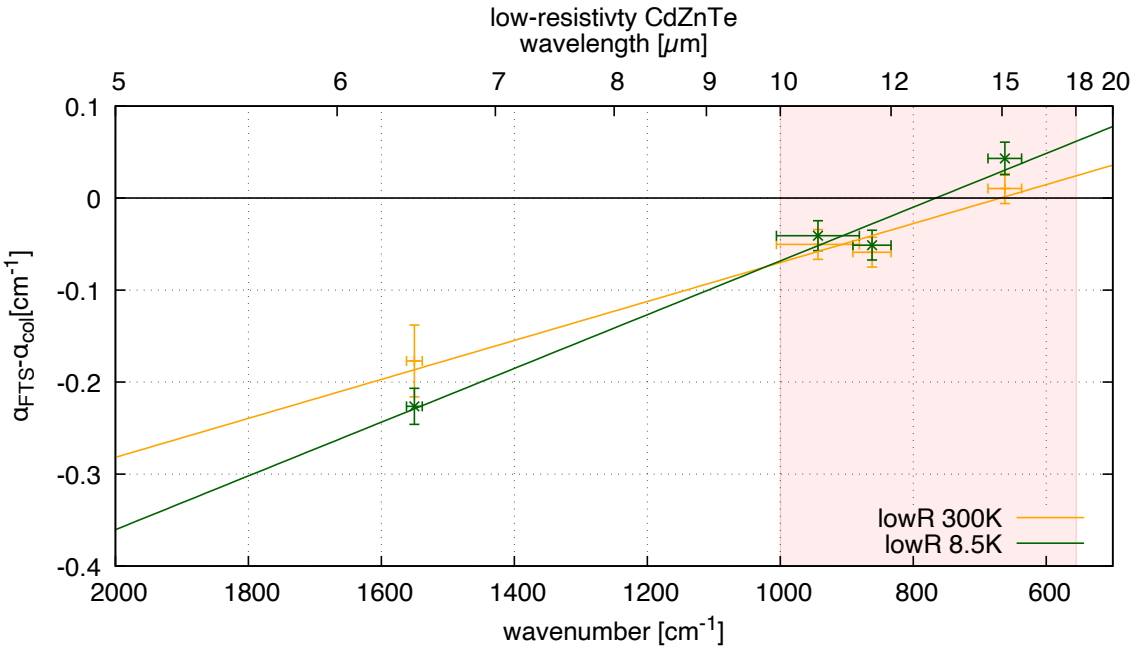

Figure. 5.3 The difference of the absorption coefficient derived from two experiments and fitting of the correction factor. Vertical error bars show the statistical uncertainty. Horizontal error bars show the bandwidth of the experiment 2.

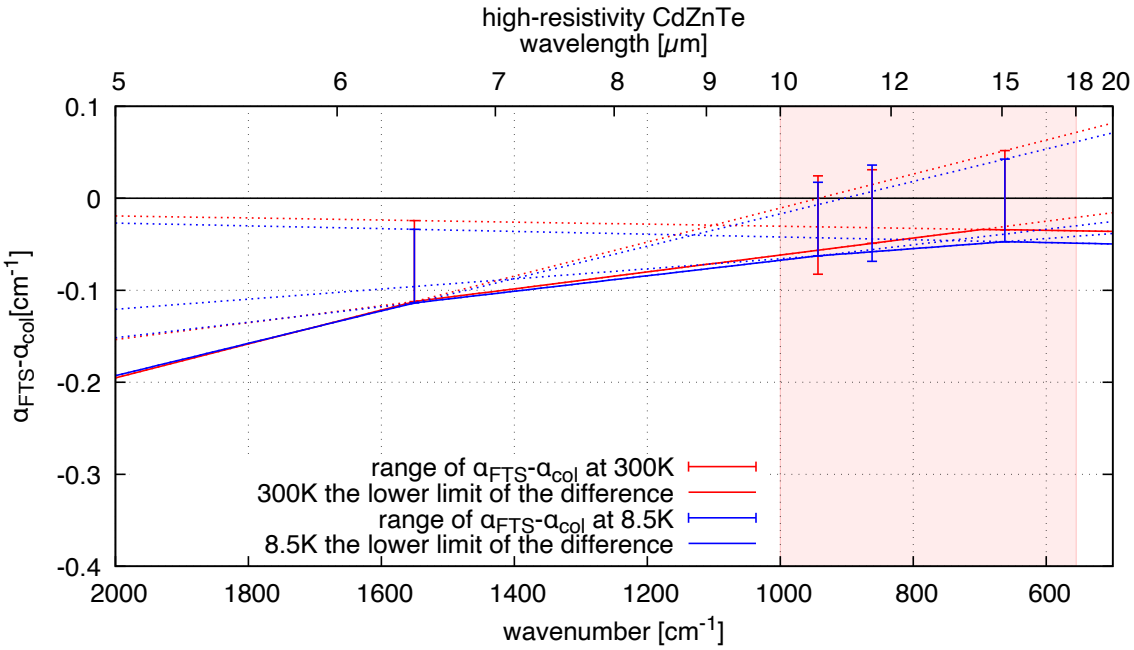

Figure. 5.4 Ranges of the difference of the absorption coefficient derived from two experiments and the lower limits of the $(a\tilde{\nu}+b)$. The dashed lines show linear functions of which the lower limits consist.

we obtain only the upper limit of the absorption coefficient of the high-resistivity CdZnTe in the collimated beam measurement. We can assume the true value of the absorption coefficient in the band $\tilde{\nu}_i$ $(i = 1, 2, 3, 4)$ is between 0 cm^{-1} and the upper limit of the $\alpha_{\mathrm{col}}(\tilde{\nu}_i)$ $(\alpha_{\mathrm{upper,col}}(\tilde{\nu}_i))$. Thus, the following inequalities are derived from equation 5.14:

$$\overline{\alpha_{\mathrm{FTS}}(\tilde{\nu}_i)} - \alpha_{\mathrm{upper,col}}(\tilde{\nu}_i) \leq a\tilde{\nu}_i + b \leq \overline{\alpha_{\mathrm{FTS}}(\tilde{\nu}_i)} \tag{5.16}$$

$$\tilde{\nu}_i = 1/\lambda_i \quad \lambda_i = 6.45,\ 10.6,\ 11.6,\ 15.1\ \mu\mathrm{m}\ (i = 1, 2, 3, 4). \tag{5.17}$$

We derive the lower limit of $a\tilde{\nu} + b$ to evaluate the upper limit of the corrected absorption coefficient. We set the lower limit of the $a\tilde{\nu} + b$ as the minimum value among linear functions which meet the four inequalities 5.16. Fig 5.4 shows the lower limit of the $a\tilde{\nu}+b$. Table 5.2 shows the lower limit of the $(a\tilde{\nu} + b)$ at each wavelength range. The general trend of the lower limit of the $(a\tilde{\nu} + b)$ increasing with wavelength is similar to the fitted $(a\tilde{\nu} + b)$ of the low-resistivity CdZnTe case and to that of the predicted value $C_{1,2}$, although slopes of them are different.

Table. 5.1 fitted-parameter a and b of the low-resistivity CdZnTe

	a $[10^{-3}\mathrm{cm}^{-2}]$	b $[\mathrm{cm}^{-1}]$	ρ_{ab}	reduced χ^2	NDF
lowR 300 K	-0.21 ± 0.04	0.14 ± 0.04	-0.974	0.9	2
lowR 8.5 K	-0.29 ± 0.04	0.22 ± 0.04	-0.955	1.5	2

Table. 5.2 The lower limit of $(a\tilde{\nu} + b)$ for the high-resistivity CdZnTe case

temperature	wavelength range $[\mu\mathrm{m}]$	a $[10^{-3}\mathrm{cm}^{-2}]$	b $[\mathrm{cm}^{-1}]$
highR 300 K	< 6.45	-0.184	0.174
	6.45–14.3	-0.091	0.030
	> 14.3	0.011	-0.041
highR 8.5 K	< 6.45	-0.175	0.159
	6.45–15.1	-0.084	0.016
	> 15.1	0.015	-0.057

Then, we estimate corrected absorption coefficients $\alpha_{\mathrm{corrected}}$ and their uncertainty $\Delta\alpha_{\mathrm{corrected}}$. We estimate the $\alpha_{\mathrm{corrected}}$ and $\Delta\alpha_{\mathrm{corrected}}$ of the low-resistivity CdZnTe as follows:

$$\alpha_{\mathrm{corrected}}(\tilde{\nu}) = \alpha_{\mathrm{FTS}}(\tilde{\nu}) - (a\tilde{\nu} + b) \tag{5.18}$$

$$\Delta\alpha_{\mathrm{corrected}}(\tilde{\nu}) = \sqrt{\Delta\alpha^2_{\mathrm{FTS,stat}} + ((\Delta a)\tilde{\nu})^2 + \Delta b^2 + 2\tilde{\nu}\rho_{ab}\Delta a\Delta b}. \tag{5.19}$$

Fig 5.5(a) shows the corrected absorption coefficient of the low-resistivity CdZnTe at room and cryogenic temperatures. The absorption coefficient at 10–18μm is α = 0.4–0.6 cm^{-1} at 300 K and α = 0.5–1.3 cm^{-1} at 8.5 K. The absorption coefficient at 8.5 K is 1.2–2.2 times larger than that at 300 K. If free-carrier absorption is dominant at cryogenic temperature, the absorption

coefficient should decrease due to carrier freeze-out. However, as shown in Figure 5.5(a), the low-resistivity CdZnTe has larger absorbance at cryogenic temperature than at room temperature. Therefore, this result suggests that there are other factors causing absorption in addition to free carrier absorption in the low-resistivity CdZnTe at cryogenic temperature. The absorption factors are discussed in section 5.2.

Then, we discuss the statistical uncertainty of the corrected absorption coefficient. Table 5.3 summarizes the uncertainties and the requirement of the absorption coefficient. The statistical uncertainties at both temperatures are more than 3 times larger than the required uncertainty ($\Delta\alpha < 0.003$ cm^{-1}).

We also evaluate the systematic uncertainty due to α-calculation method $\Delta\alpha_{\rm calc}$ for the low-resistivity CdZnTe case. We use equation 2.5, assuming that the refractive index is $n = 2.7$ (Ikeda et al. 2015). The systematic uncertainty is derived as $\Delta\alpha_{\rm calc} = 0.03$ cm^{-1} for the α range of the low-resistivity CdZnTe ($\alpha = 0.35 - 1.4$ cm^{-1}).

We compare the uncertainty of the corrected absorption coefficient and the uncertainty in the case of the FTS measurements. If we measure absorption coefficient only with FTS systems, the uncertainty is mainly the sum of the long-term statistical error $\Delta\alpha_{\rm stat,long}$, the systematic error due to the defocus $\Delta\alpha_{\rm defocus}$, and the systematic error due to calculation method $\Delta\alpha_{\rm calc}$. The long-term statistical error is $\Delta\tau_{\rm stat,long}/\tau = 0.03,\ 0.002$ for thick and thin sample cases, respectively (see section 3.2.3). The uncertainty of absorption coefficient due to the long-term statistical error is derived as $\Delta\alpha_{\rm stat,long} = 0.03$ cm^{-1} from equation 3.3 and 3.9. The 10–18 μm uncertainty due to the defocus effect is evaluated as $\Delta\alpha_{\rm defocus} = 0.06$cm^{-1} from the range of correction factor $-(a\tilde{\nu} + b)$. Therefore, the uncertainty of the corrected absorption coefficient (statistical uncertainty: $\Delta\alpha_{\rm corrected} = 0.01 - 0.02$ cm^{-1} + systematic uncertainty: $\Delta\alpha_{\rm calc} = 0.03$ cm^{-1}) is smaller than the uncertainty in the case of the FTS measurements (long-term statistical uncertainty: $\Delta\alpha_{\rm stat} = 0.03$ cm^{-1} + uncertainty due to the defocus: $\Delta\alpha_{\rm defoucs} = 0.06$ cm^{-1} + systematic uncertainty due to the calculation method: $\Delta\alpha_{\rm calc} = 0.03$ cm^{-1}).

We compare the current result with the previous study (Sarugaku et al. 2017). At room temperature, the absorption coefficient of the low-resistivity CdZnTe calculated in the current work is about 1.2 times higher than that by Sarugaku et al. (2017). The free carrier density is proportional to the resistivity. If the dominant absorber is the free carrier at room temperature, the absorption coefficient is considered to be proportional to the resistivity. The resistivity of our sample is $(0.5 - 1.3) \times 10^2$ Ωcm and that of Sarugaku et al. (2017) is $\sim 1 \times 10^2$ Ωcm. Since the resistivity of our sample has large uncertainty ($\Delta\rho/\rho \sim 44\%$), it is unclear whether the difference of absorption coefficient is significant regardless of the difference of the resistivity.

Next, we estimate the upper limit of $\alpha_{\rm corrected}$ of the high-resistivity CdZnTe. The upper limit of the $\alpha_{\rm corrected}$ is derived as the sum of the upper limit of the correction factor and $\alpha_{\rm FTS} + 5\Delta\alpha_{\rm FTS,stat}$. Fig 5.5(b) shows the corrected absorption coefficient of high-resistivity CdZnTe at room and cryogenic temperature. We obtain 5-σ upper limit of the absorption coefficient of the high-resistivity CdZnTe ($\alpha < 0.11$ cm^{-1} at 300 K and $\alpha < 0.16$ cm^{-1} at 8.5 K).

Table. 5.3 The statistical uncertainty of the corrected α

	T [K]	$\Delta\alpha_{\rm corrected}$ [cm^{-1}] (5–20 μm)	$\Delta\alpha_{\rm corrected}$ [cm^{-1}] (10–18 μm)
requirement		< 0.003	< 0.003
low-resistivity CdZnTe	300K	0.01–0.06	0.01–0.02
	8.5 K	0.01–0.04	0.01–0.02

The systematic uncertainty due to the calculation method is estimated as $\Delta\alpha_{\rm calc} < 0.011$ cm^{-1} at 300 K and $\Delta\alpha_{\rm calc} < 0.016$ cm^{-1} at 8.5 K in a similar way for the low-resistivity case. The absorption coefficients of the high-resistivity CdZnTe is lower than those of the low-resistivity CdZnTe both at 300 K and at 8.5 K. We discuss the suitability of the high-resistivity CdZnTe as an IG material in section 5.3.

We obtain the corrected 5–20 μm absorption coefficient free from the defocus error at 300 K and at 8.5 K by combining the results of the two types of experiments. The 10–18 μm absorption coefficient of the low-resistivity CdZnTe becomes larger at 8.5 K ($\alpha = 0.5$–1.3 cm^{-1}) than that at 300 K ($\alpha = 0.4$–0.6 cm^{-1}). This result suggests that there are other absorption factors in addition to free carrier absorption in the low-resistivity CdZnTe at cryogenic temperature. The uncertainty of the corrected α is improved from the uncertainty in the FTS measurements. Also, we obtain 5-σ upper limit of the 10–18 μm absorption coefficient of the high-resistivity CdZnTe: $\alpha < 0.11$ cm^{-1} at 300 K and $\alpha < 0.16$ cm^{-1} at 8.5 K.

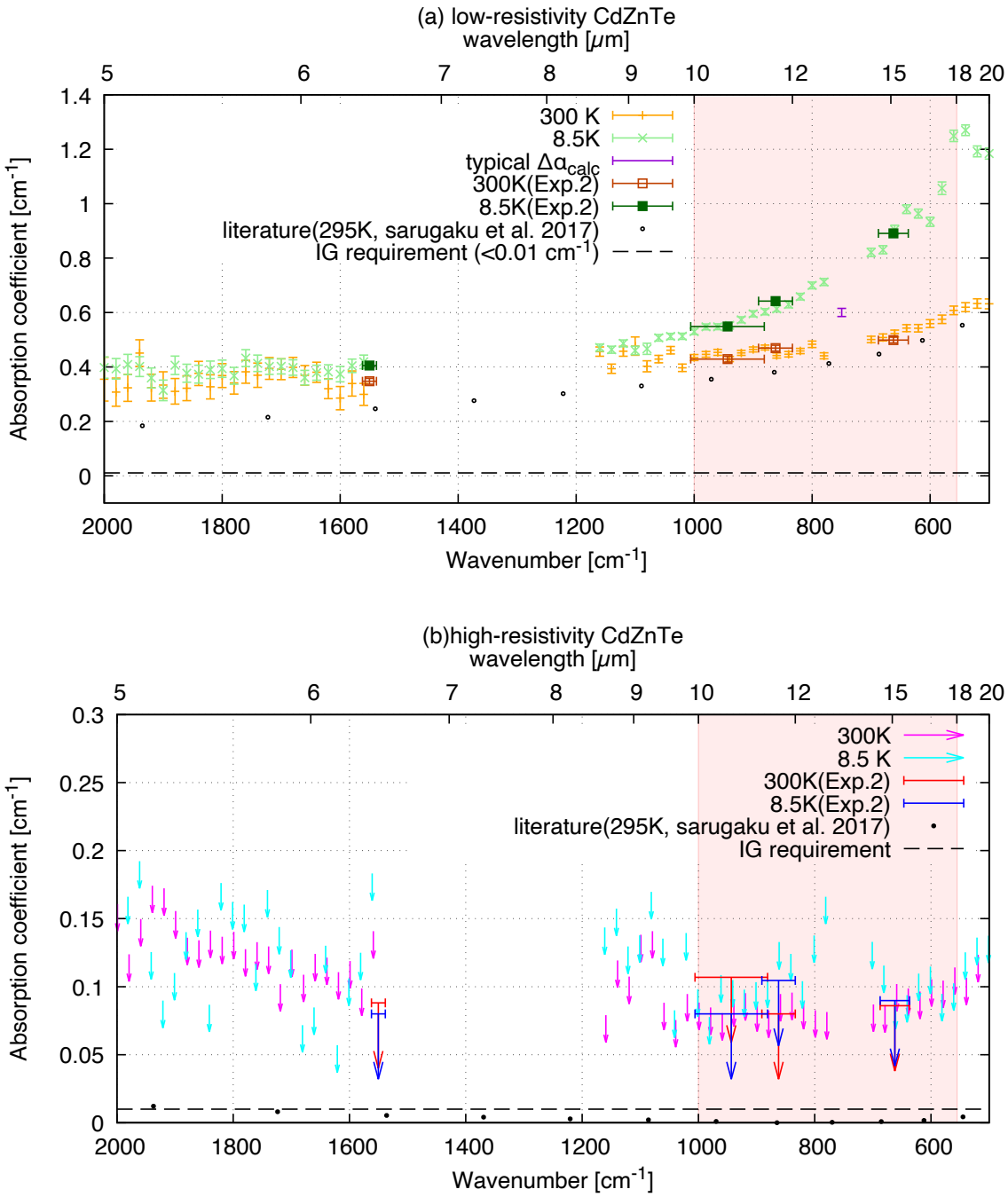

Figure. 5.5 The corrected absorption coefficient at room and cryogenic temperature. The area painted in light pink is the SPICA SMI/HR wavelength range (10–18 μm). The result of previous research at 295 K (black points) are plotted based on Figure 2 of Sarugaku et al. (2017). (a) The low-resistivity CdZnTe case. (b) The high-resistivity CdZnTe case. Vertical error bars of data points show statistical uncertainties $\Delta\alpha_{\rm corrected}$. The purple error bar shows the typical systematic uncertainty $\Delta\alpha_{\rm calc}$. Horizontal error bars show the bandwidth. The dashed line shows the requirement value of IG material($< 0.01{\rm cm}^{-1}$).

5.2 Causes of absorption of low-resistivity CdZnTe

We here discuss the absorption sources in the low-resistivity CdZnTe. In previous studies (Kaji et al. 2014; Sarugaku et al. 2017), the absorption of the low-resistivity CdZnTe is considered to be due to free carriers. The absorption coefficient due to free carriers is proportional to the free-carrier density. If the absorption is solely due to free carriers, the free carriers are frozen and the absorption coefficient should decrease at cryogenic temperature. In the case of CdTe, the free-hole density of a low-resistivity CdTe ($\sim$ 30 Ωcm; Ahmad 2015) decreases from 2×10^{15} cm^{-3} to $< 10^{7}$ cm^{-3} during cooling from 300 K to $<$ 25 K. If the free hole density of the low-resistivity CdZnTe has the same temperature dependence as that of the CdTe ($\sim$ 30 Ωcm), free-carrier absorption at $<$ 25 K becomes negligible ($< 10^{-9}$ cm^{-1}). However, our result shows that the α of the low-resistivity CdZnTe increased at cryogenic temperature. Therefore, there are other sources of absorption in addition to free carrier absorption.

5.2.1 Temperature dependences of absorption coefficient at 6.45, 10.6, 11.6 and 15.1 μm

To discuss dominant factors causing the absorption of the low-resistivity CdZnTe at 8.6–300 K, we list possible causes of absorption. As described in section 2.3, the low-resistivity CdZnTe is a p-type semiconductor. From absorption factors described by Sarugaku et al. (2017) and Čápek et al. (1973), we consider the following five factors as those which cause absorption in the p-type low-resistivity CdZnTe at 5–20 μm:

- $\alpha_{\rm intra}$: (A: see Figure 5.6) Absorption due to hole transition in the same valence subband with different wave vector k (Sarugaku et al. 2017). The absorption is proportional to free-hole density.
- $\alpha_{\rm inter}$: (B) Absorption due to the direct transition of holes from heavy hole subband to light hole subband (Čápek et al. 1973; Basu 2003). The absorption is proportional to free-hole density.
- $\alpha_{\rm trapped}$: (C) Absorption due to hole transition from the acceptor level to the valence band (Čápek et al. 1973). the absorption is proportional to trapped-hole density.
- $\alpha_{\rm Te}$: Attenuation due to Rayleigh scattering by $<$ 2 μm-size Te precipitates (Sarugaku et al. 2017).
- $\alpha_{\rm lattice}$: Absorption due to lattice vibrations (Sarugaku et al. 2017).

Figure 5.6 shows schematic view of the band structure of CdZnTe and the transition (A), (B) and (C).

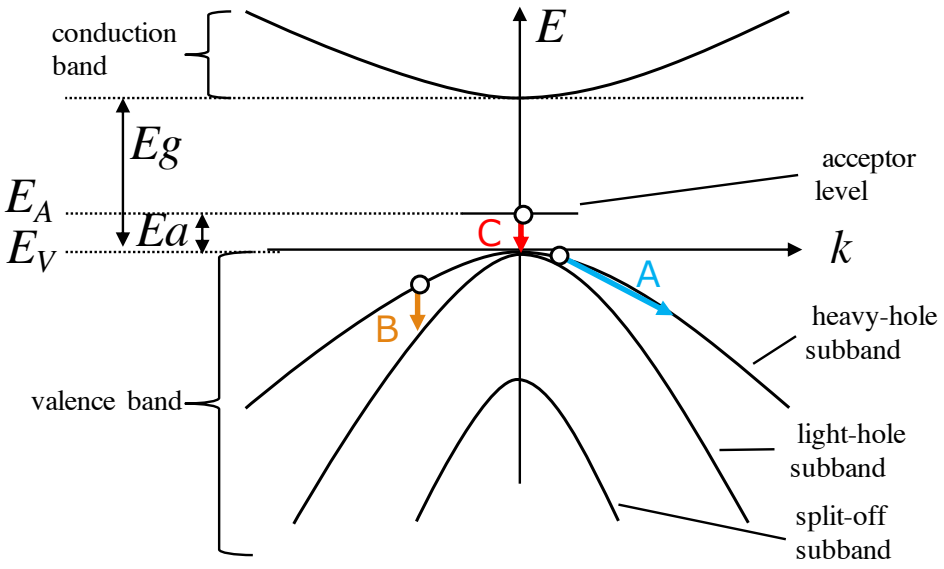

Figure. 5.6 Schematic view of the band structure of CdZnTe. Three types of hole transitions are shown: (A) intra-valence band transition (B) inter-valence band transition and (C) acceptor level transition.

The total α is expressed as

$$\alpha = \alpha_{\text{intra}} + \alpha_{\text{inter}} + \alpha_{\text{trapped}} + \alpha_{\text{Te}} + \alpha_{\text{lattice}} \tag{5.20}$$

$$= \sigma_{\text{intra}} N_{\text{free}} + \sigma_{\text{inter}} N_{\text{free}} + \sigma_{\text{trapped}} N_{\text{trapped}} + \alpha_{\text{Te}} + \alpha_{\text{lattice}}, \tag{5.21}$$

where σ_{intra},σ_{inter} and σ_{trapped} are absorption cross-section of (A) intra-valence band, (B) inter-valence band, and (C) acceptor level to valence band transition, respectively. The density of free holes is denoted as N_{free} and that of holes trapped at the acceptor level is denoted as N_{trapped}.

To determine N_{free} and N_{trapped} as a function of temperature, we derive free-hole density as the similar way of the appendix of Ahmad (2015). First, we assume a single acceptor level of E_A for simplicity. Ashcroft & Mermin 1976 (page. 581) describes the trapped hole density in the acceptor level N_{trapped} as

$$N_{\text{trapped}} = \frac{N_A}{\frac{1}{2}\exp(\frac{\mu_c - E_A}{k_B T}) + 1}, \tag{5.22}$$

where N_A is the density of acceptors, μ_c is the chemical potential, and k_B is the Boltzman constant. Since the sum of free hole density N_{free} and trapped hole density N_{trapped} is equal to the acceptor density N_A, free hole density N_{free} is expressed as

$$N_{\text{free}} = N_A - N_{\text{trapped}} = \frac{N_A}{2\exp(\frac{E_A - \mu_c}{k_B T}) + 1}. \tag{5.23}$$

Also, free hole density N_{free} is related to the effective density of states in the valence band N_V as

$$N_{\text{free}} = N_V \exp\left(-\frac{\mu_c - E_V}{k_B T}\right), \tag{5.24}$$

where E_V shows the top level of the valence band. By eliminating the common $\exp(\mu_c/k_BT)$ term in equations 5.23 and 5.24, we obtain the following equation:

$$N_{\rm free}^2 + \frac{N_V}{2}\exp(-E_a/k_BT)N_{\rm free} - \frac{N_V N_A}{2}\exp(-E_a/k_BT) = 0 \tag{5.25}$$

$$E_a \equiv E_A - E_V. \tag{5.26}$$

Therefore, $N_{\rm free}$ and $N_{\rm trapped}$ are expressed as

$$N_{\rm free} = N_A \frac{2}{\sqrt{1 + 8N_A/N_V \exp(E_a/k_BT)} + 1} \tag{5.27}$$

$$N_{\rm trapped} = N_A - N_{\rm free}. \tag{5.28}$$

According to Kittel (2005), the effective density of states N_V is given by

$$N_V = 2(2\pi m_* k_B T/h^2)^{3/2} = 4.12 \times 10^{18} \left(\frac{m_*}{0.30 m_e}\right)^{3/2} \left(\frac{T}{300\ {\rm K}}\right)^{3/2}\ {\rm cm}^{-3}, \tag{5.29}$$

where m_* shows the effective hole mass ($m_*/m_e = 0.30$ for CdTe; Wakaki et al. 2007) and h is the Planck constant. We obtain the free/trapped-hole density model of equation 5.27 and 5.28.

Next, we discuss the absorption cross-section of (A) intra-band absorption. Holes in the valence band transfer to a different k-space in the same band and cause intra-valence band absorption. The absorption cross-section is derived from the Drude model (e.g., Kudo 1996) as

$$\sigma_{\rm intra} = \frac{q^2}{\pi n c^5 m^* \tau_R(T) \tilde{\nu}^2} = b_0 \left(\frac{\tilde{\nu}}{943\ {\rm cm}^{-1}}\right)^{-2} \left(\frac{T}{300{\rm K}}\right)^{-1.5}, \tag{5.30}$$

where q is effective charge, n is the refractive index, c is the light speed, m^* is the effective mass, and τ_R is the relaxation time. The relaxation time τ_R is the mean time interval of the collision of a free-hole with atomic nuclei. The relaxation time τ_R is proportional to hole mobility μ. According to Ahmad (2015), we assume that the mobility μ is proportional to $T^{-1.5}$, which means that holes are dominantly scattered by lattice vibrations.

Then, (B) inter-valence band absorption is caused by the hole transition between heavy-hole and light-hole subbands. According to Basu (2003), the absorption cross-section is described as

$$\sigma_{\rm inter} = a_0 \left(\frac{\tilde{\nu}}{943\ {\rm cm}^{-1}}\right)^{0.5} \left(\frac{T}{300\ {\rm K}}\right)^{-1.5} \times \left[1 - \exp\left(-\frac{hc\tilde{\nu}}{k_BT}\right)\right] \exp\left(-\left(\frac{m_h}{m_l} - 1\right)^{-1} \frac{hc\tilde{\nu}}{k_BT}\right), \tag{5.31}$$

where m_h/m_l is the effective mass ratio of heavy and light holes. The temperature dependence of this cross-section is mainly caused by the difference between the occupational probability of the initial state and that of the final state.

Next, we discuss (C) the cross-section of trapped-hole absorption. We assume the temperature dependence of the cross-section of trapped-hole absorption $\sigma_{\rm trapped}$ is negligible. This is because that the temperature dependence of the absorption cross-section is mainly due to the

temperature dependence of occupational probability difference of initial acceptor state-i and final state-j in the valence band ($f_i - f_j$) (Basu 2003). At low temperatures, most of the holes will be trapped at the acceptor state and free holes will be exhausted. Since the trapped-hole absorption will be dominant at cryogenic temperature, we assume that $f_i \sim 1$, $f_j \sim 0$ and that the cross-section of trapped-hole is independent of temperature.

Now we estimate the scattering attenuation due to Te particles. From Cox et al. (2002), the attenuation cross-section of Rayleigh scattering σ_{Te} is expressed as

$$\sigma_{\mathrm{Te}} = \frac{8\pi}{3} \frac{2\pi n(\mathrm{CdZnTe})}{\lambda^4} \left(\frac{(m^2-1)}{(m^2+2)} \right)^2, \tag{5.32}$$

where d is the size of precipitate and $m = n(\mathrm{Te})/n(\mathrm{CdZnTe})$ is the refractive index ratio. At 300K, Rayleigh scattering attenuation by Te precipitates is evaluated by Sarugaku et al. (2017) and $\alpha_{\mathrm{Te}} \leq 0.01$ cm^{-1} at 5–20 μm. If we apply the literature value of the coefficient of thermal expansion of Te (1.68×10^{-5} /K; Wakaki et al. 2007), the scattering attenuation at cryogenic temperature is $\sim 98\%$ of that at room temperature. In the low-resistivity CdZnTe, this attenuation is negligible due to little contribution to the total absorption.

Next, we estimate the absorption due to lattice vibration. According to Deutsch (1975), the lattice absorption at a longer wavelength is empirically expressed as

$$\alpha_{\mathrm{lattice}}(\tilde{\nu}) = B_1 \exp(-B_2 \tilde{\nu}/\tilde{\nu}_0). \tag{5.33}$$

The room temperature parameters fitted by Sarugaku et al. (2017) are used in the current study ($B_1 = 1.46 \times 10^5$ cm^{-1}, $B_2 = 5.38$, $\tilde{\nu}_0 = 167$ cm^{-1}). We evaluate $\alpha_{\mathrm{lattice}}(\tilde{\nu}) \leq \alpha_{\mathrm{lattice}}(500\ \mathrm{cm}^{-1}) = 0.015$ cm^{-1} at 5–20 μm at room temperature. The lattice absorption strength is proportional to the difference of phonon creation and annihilation probability. The strength of lattice absorption with the multi phonon process decreases with temperature (Kudo 1996). Therefore, the absorption coefficient due to the lattice vibration is $\alpha_{\mathrm{lattice}} < 0.015$ cm^{-1}at 5–20 μm, which is much smaller than the absorption coefficient of the low-resistivity CdZnTe.

Following the above discussions, we ignore the factors of the $\alpha_{\mathrm{Te}}(< 0.01\mathrm{cm}^{-1})$ and the $\alpha_{\mathrm{lattice}}(< 0.015$ cm$^{-1})$ for the low-resistivity CdZnTe, because they are negligibly smaller than the total absorption ($\alpha > 0.3$ cm^{-1}). The model of the temperature dependence of absorption coefficient of the low-resistivity CdZnTe at $\tilde{\nu}$ cm^{-1} is now described as

$$\alpha_{\tilde{\nu}}(T) = N_{\mathrm{free}}(T)(\sigma_{\mathrm{intra},\tilde{\nu}}(T) + \sigma_{\mathrm{inter},\tilde{\nu}}(T)) + N_{\mathrm{trapped}}(T)\sigma_{\mathrm{trapped}}. \tag{5.34}$$

We fit the absorption coefficient of the low-resistivity CdZnTe obtained in experiment 2 with the $\alpha_{\tilde{\nu}}(T)$ model of equation 5.34 in order to determine what causes absorption in the low-resistivity CdZnTe.

First, we fit the 10.6 μm absorption coefficient of the low-resistivity CdZnTe measured in experiment 2 with the $\alpha_{\tilde{\nu}}(T)$ model of equation 5.34. The free parameters of this fitting is the N_A, E_a, b_0, a_0, m_h/m_l and $\sigma_{\mathrm{trapped}}$.

Figure 5.7 shows the model fitting result at 10.6 μm. Each fitted-parameters are listed in Table 5.4: the acceptor density $N_A = (4.1 \pm 0.7) \times 10^{14}$ cm^{-3}, the acceptor energy $E_a = 63 \pm 1$

meV, the effective mass ratio $m_h/m_l = 6.53 \pm 0.06$, and the proportional coefficients ($a_0 = (1.8 \pm 0.03) \times 10^{-15}$ cm^2, $b_0 = (0.243 \pm 0.008) \times 10^{-15}$ cm^2 and $\sigma_{\text{trapped}} = (1.337 \pm 0.0008) \times 10^{-15}$ cm^2).

As shown in Figure 5.7, (A) intra-band absorption and (B) inter-band absorption are dominant at 300 K. These two absorption is due to free-holes. The intra-band absorption (A) becomes smaller with cooling and becomes negligible at $T < 100$ K. The inter-band absorption coefficient (B) has a peak at ~ 180 K, gradually decays at $T < 150$ K and becomes negligible at $T < 50$ K. On the other hand, the absorption due to trapped hole (3) gradually increases with temperature at < 150 K, and becomes roughly constant ($\alpha = 0.55$ cm^{-1}) at $T < 50$ K.

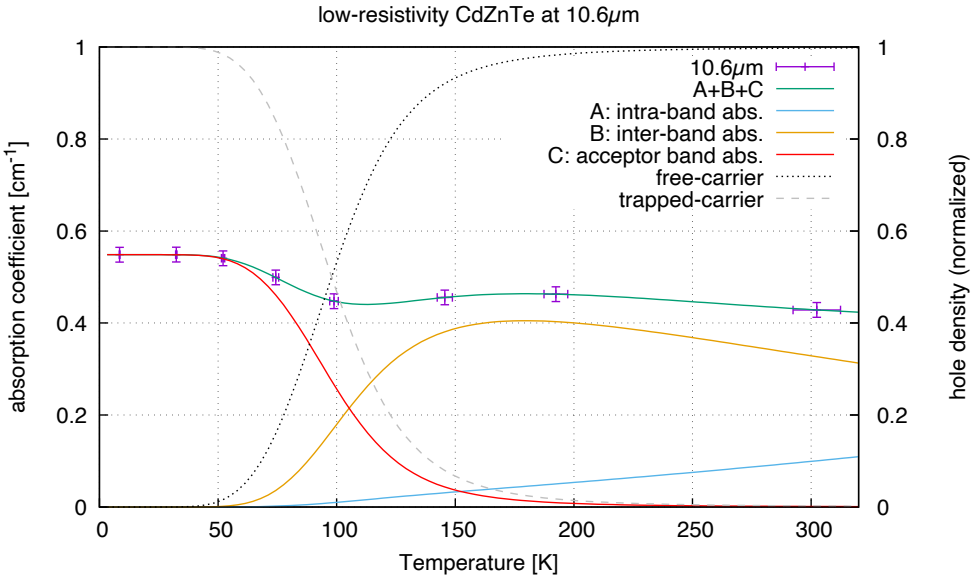

Figure. 5.7 Temperature dependence of the 10.6μm absorption coefficient of the low-resistivity CdZnTe and the fitted-model. The purple points show the measured absorption coefficient in experiment 2. The green line shows the fitted-model. The blue, orange and red lines show the contribution of (A) the intra-band absorption, (B) the inter-band absorption, (C) the acceptor level absorption, respectively. The dotted line shows the normalized free-hole density. The dashed line shows the normalized trapped-hole density.

We discuss how each parameter affects the temperature dependence of the 10.6 μm absorption coefficient. N_A and E_a determine the free- and trapped-hole densities (N_{free}, n_{trapped}). According to equation 5.27, the free hole density starts to decrease by $\exp(-E_a/2k_BT)$ when the effective density of states $N_V(T)$ smaller than the acceptor density N_A. Therefore, N_A determines the switching temperature between saturation regime, where free hole density is independent on temperature, and ionization regime, where the density decreases by $\exp(-E_a/2k_BT)$. Also, E_a determines temperature dependence of free-hole density among the ionization regime. The effective mass ratio of heavy and light holes m_h/m_l determines the temperature dependence of inter-band absorption at moderate temperature (150–300 K). Effective mass affects the occupation probability in the band at a certain temperature. Therefore the effective mass ratio m_h/m_l affects the occupation probability difference between the initial state of the heavy hole band

and final state of the light hole band. The other parameters (b_0, a_0, $\sigma_{\rm trapped}$) are proportional coefficients of absorption factors.

Then, we evaluate the effect of the systematic uncertainty $\Delta\alpha_{\rm calc}$ to the model-fitting. If we assume the α shifts systematically by $\Delta\alpha_{\rm calc}$ derived from equation 2.5, the α is corrected by $+0.03\ {\rm cm}^{-1}$ shifting. When we fit the model with this corrected α, the obtained fitted parameters are $N_A = (4.2 \pm 0.7) \times 10^{14}\ {\rm cm}^{-3}$, $E_a = 63 \pm 1$ meV, $m_h/m_l = 6.55 \pm 0.06$, $a_0 = (1.90 \pm 0.03) \times 10^{-15}\ {\rm cm}^2$, $b_0 = (0.260 \pm 0.008) \times 10^{-15}\ {\rm cm}^2$, and $\sigma_{\rm trapped} = (1.408 \pm 0.001) \times 10^{-15}\ {\rm cm}^2$. The reduced-$\chi^2 = 0.002$ and the degree of freedom NDF$= 2$ is the same as those before the correction. The proportional coefficients a_0, b_0 and $\sigma_{\rm trapped}$ increase by 5–7% compared to those before the correction. The physical parameters N_A, E_a and m_h/m_l are consistent with those before correction within the 1-σ uncertainty range. Therefore, the systematic uncertainty $\Delta\alpha_{\rm calc}$ affect only the proportional coefficient, and does not affect the obtained physical parameters and discussion about absorption factors.

Next, we fit the absorption coefficient at other bands (6.45, 11.6 and 15.1 μm) with the $\alpha_{\tilde{\nu}}(T)$ model of equation 5.34. The $\alpha_{\tilde{\nu}}(T)$ model have E_a, b_0, a_0, m_h/m_l and $\sigma_{\rm trapped}$ as free parameters. The acceptor density N_A is fixed as $(4.1 \pm 0.7) \times 10^{14}\ {\rm cm}^{-3}$, because only the results at 10.6 μm have good quality to allow N_A fit as a free parameter. Figure 5.8 shows the fitting results at 6.45, 11.6 and 15.1 μm, respectively. The fitting results are summarized in Table 5.4. The physical parameters and two proportional factors ($E_a, m_h/m_l, a_0, b_0$) fitted at each band are consistent within 2-σ uncertainty range. At all of the bands, the (A) intra-band and (B) inter-band absorptions are dominant at room temperature and the (C) trapped-hole absorption is dominant at cryogenic temperature (< 50 K) as with the case of the 10.6 μm fitting.

We now compare our derived physical parameters with those in past studies. First, we discuss the acceptor energy gap E_a. The parameter of the acceptor energy gap E_a is common for all our fitting results (E_a=63 meV). and consistent with a Hall effect measurement of CdTe by Ahmad (2015) ($\sim$ 60 meV) and a photoluminescence measurement of CdTe by Molva et al. (1984) ($\sim$ 58.7meV). Ahmad (2015) measured acceptor energy gap E_a of Na-doped p-type CdTe by van der Pauw Hall effect method. When a magnetic field is applied in the direction perpendicular to the applied electric current, a Hall voltage is generated in the direction perpendicular to the current and magnetic field directions (van der Pauw 1958). Ahmad (2015) derived the hole density from the Hall voltage since the Hall voltage is inverse proportional to the hole density. On the other hand, (Molva et al. 1984) irradiated laser light to p-type CdTe and measured spectra of re-emission lines by photoluminescence. We assume the acceptor gap of the p-type low-resistivity CdZnTe is the same as that of p-type CdTe since the abundance ratio of Zn to Cd is only $\sim 4\%$. The acceptor energy gaps fitted in the current study are consistent at $< 10\%$ with these past studies, although these values are obtained in different ways.

The mass ratio in this current work m_h/m_l is about 5–8 and consistent with previous studies ($\sim$ 7; Čápek et al. 1973, $\sim$ 5; Becker et al. 1989). These previous studies determined the effective mass ratio by fitting the infrared absorption coefficient (Becker et al. 1989; Čápek et al. 1973).

Then we estimate the acceptor density N_A from the resistivity to compare with the fitted acceptor density. The hole density at 300 K ($N_{\rm free}$(300 K)) can be derived from the resistivity ρ as

$$N_{\rm free}(300\ {\rm K}) = \frac{1}{q\rho\mu} = (9 \pm 5) \times 10^{14} \left(\frac{\rho(300\ {\rm K})}{90 \pm 40 \Omega{\rm cm}} \right)^{-1} \left(\frac{\mu(300\ {\rm K})}{80{\rm cm}^2/{\rm Vsec}} \right)^{-1} \ [{\rm cm}^{-3}], \quad (5.35)$$

where q is a charge of a single hole (1.602×10^{-19} C) and μ is mobility ($\sim 80{\rm cm}^2/{\rm Vsec}$, CdTe case; Ahmad 2015). We assume the mobility of CdZnTe is the same as that of CdTe. Since the crystal at the room temperature is in the saturation regime (see Figure 5.7), the $N_{\rm free}$(300 K) is roughly the same as the acceptor density N_A. The acceptor density N_A derived from the α-fitting ($N_A = (4.1 \pm 0.7) \times 10^{14}$ cm^{-3}) is consistent with the value derived from the resistivity ($N_A = N_{\rm free}(300\ {\rm K}) = (9 \pm 5) \times 10^{14}$ cm^{-3}).

Following the above discussion, the measured absorption coefficient is well-fitted with the model of absorption by free/trapped holes and reasonable physical parameters (E_a,m_h/m_l and N_A). Our results suggest that the dominant factors causing absorption in CdZnTe change with temperature: inter-valence band absorption is dominant at $T = 150$–300 K and absorption due to trapped-hole is dominant at $T < 50$ K. The absorption coefficient due to free holes become lower and negligible at $T < 50$ K as we initially predicted. However, it is not enough. The absorption coefficient due to trapped holes increase with cooling and become dominant at $T < 50$ K.

Table. 5.4 Parameters fitted at each wavelength band. (NDF:degrees of freedom)

	6.45 μm	10.6 μm	11.6 μ m	15.1 μm
N_A [cm^{-3}]	4.1×10^{14}(fixed)	$(4.1 \pm 0.7) \times 10^{14}$	4.1×10^{14}(fixed)	4.1×10^{14}(fixed)
E_a [meV]	63 ± 3	63 ± 1	63 ± 4	62 ± 7
m_h/m_l	7.9 ± 0.6	6.53 ± 0.06	6.7 ± 0.6	6.1 ± 1.2
a_0 [10^{-15} cm^2]	1.6 ± 0.4	1.8 ± 0.03	1.7 ± 0.3	1.7 ± 0.6
b_0[10^{-15} cm^2]	0.4 ± 0.3	0.243 ± 0.008	0.30 ± 0.07	0.24 ± 0.08
$\sigma_{\rm trapped}$[10^{-15} cm^2]	1.00 ± 0.01	1.337 ± 0.0008	1.55 ± 0.01	2.15 ± 0.03
reduced-χ^2	0.21	0.001	0.29	1.1
NDF	3	2	3	3

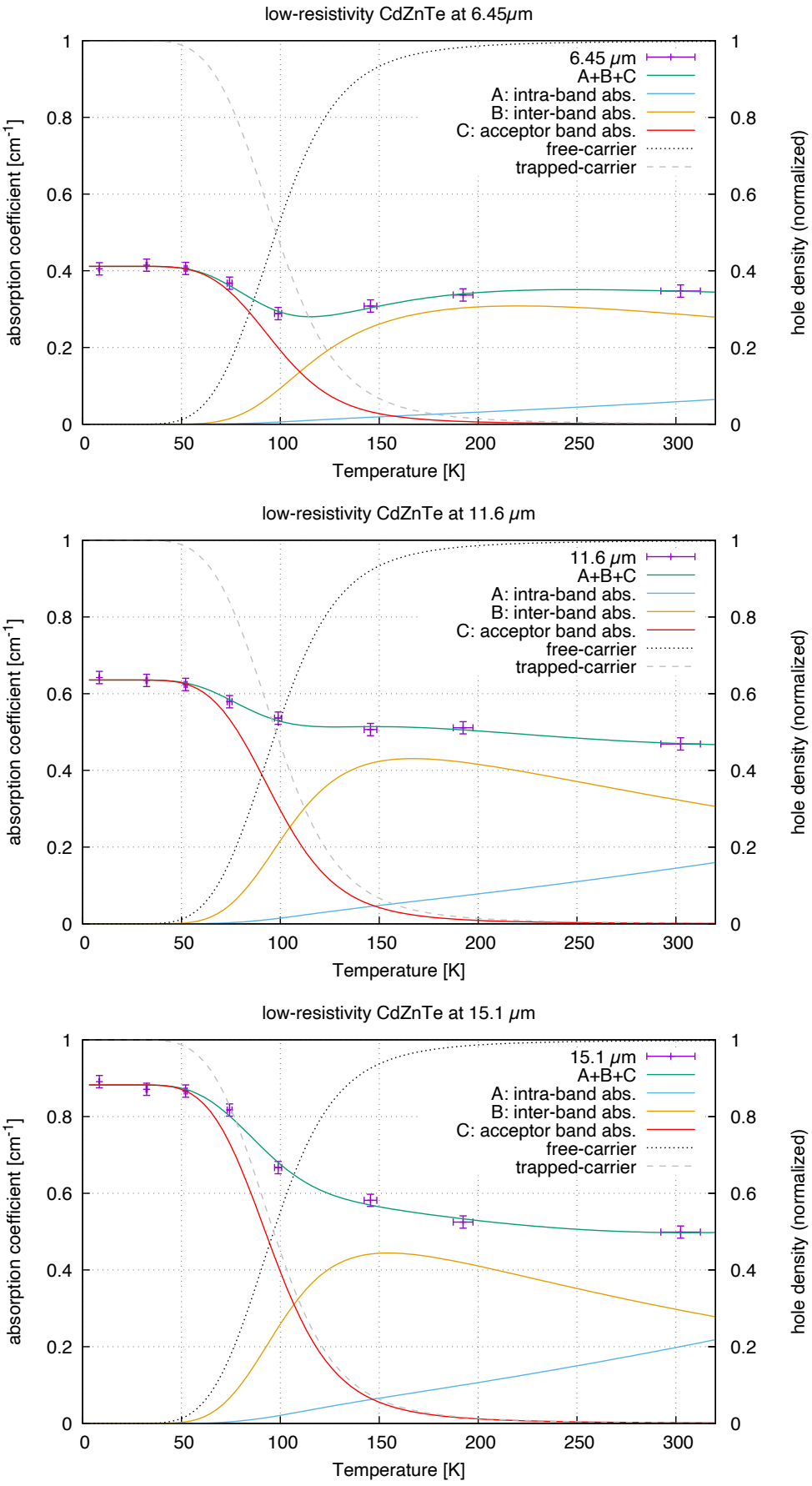

Figure. 5.8 Temperature dependences of the 6.45, 11.6 and 15.1 μm absorption coefficients of the low-resistivity CdZnTe and the fitted-models.

5.2.2 Wavenumber dependences of absorption coefficient at 300 K and at 8.5 K

In the previous subsection, we discuss the temperature dependence of the α at four measured wavelengths and suggest that the temperature dependence of the model is consistent with the current results. In this subsection, we discuss the wavenumber dependence of the α using the FTS data corrected by the beam measurements. To research the consistency between the wavenumber dependence of the model described in section 5.2.1 and the current results, we fit the model with the corrected α spectra of the low-resistivity CdZnTe and compare the fitted-values with those in section 5.2.1.

First, we fit the model described in section 5.2.1 with the corrected α of the low-resistivity CdZnTe at 300 K. From the discussion in section 5.2.1, the fitted model is expressed as

$$\alpha(\tilde{\nu}, 300\ \mathrm{K}) = N_{\mathrm{free}}(300\ \mathrm{K})(\sigma_{\mathrm{intra}}(\tilde{\nu}, 300\ \mathrm{K}) + \sigma_{\mathrm{inter}}(\tilde{\nu}, 300\ \mathrm{K})). \tag{5.36}$$

We ignore the absorption due to trapped-holes because we can assume almost all of the holes are free holes at 300 K (See section 5.2.1). Fitting parameters are m_h/m_l, a_0, b_0. We fix $E_a = 63$ meV and $N_A = 4.1 \times 10^{14}$ cm^{-3} since these parameters affect only trapped/free-hole density and does not affect wavenumber dependence of absorption coefficient.

We first perform the fitting at 6.45–15.1 μm to compare with the result in section 5.2.1 by fitting the same wavelength range. Figure 5.9 shows the wavenumber dependence of the corrected α of the low-resistivity CdZnTe at 300 K and the fitted absorption model in equation 5.36 (green in Figure 5.9). The fitted parameters are effective mass ratio $m_h/m_l = 13 \pm 8$, $a_0 = (1.2 \pm 0.5) \times 10^{-15}$ cm^2, $b_0 = (0.24 \pm 0.07) \times 10^{-15}$ cm^2, the reduced-$\chi^2 = 2.8$, and the degree of freedom $NDF = 21$. The fitted parameters are consistent with the results in section 5.2.1 within the range of $2 - \sigma$, although the fitting uncertainty is relatively large.

Next, we perform the fitting at 5–20 μm wavelength range (dashed green in Figure 5.9) to check the wavelength dependence in the broad wavelength range. The fitted parameters are $a_0 = (1.19 \pm 0.08) \times 10^{-15}$ cm^2, $b_0 = (0.26 \pm 0.01) \times 10^{-15}$ cm^2, $m_h/m_l = 13 \pm 1$, the reduced-$\chi^2 = 1.6$, and the degree of freedom $NDF = 51$. The proportional coefficient b_0 is consistent with the results in section 5.2.1 within the range of $1 - \sigma$ uncertainty. The fitted a_0 is $\sim 60\%$ of the fitted value derived in section 5.2.1. The effective mass ratio m_h/m_l is $3 - \sigma$ difference between the result in the current work and the results in section 5.2.1. We suspect that the k-vector dependence of the effective mass may provide the difference between the fitted value in the current work and that in section 5.2.1. The effective mass depends on the curvature of the band and we assume that the band structure $E(k)$ is a parabolic shape. Since the inter-band absorption is a direct transition, the absorption wavelength is related to the k-vector of the hole. The parabolic shape band structure is only an assumption, and derived effective masses may depend on the wavelength. We note that the wavelength dependence of the fitted effective mass is just a supposition. We need to improve the wavelength dependence of the absorption model to be fitted to the α at the wavelength range of 5–20 μm.

As discussed above, the general trend of the model that the α increases with longer wavelength is similar to the corrected absorption coefficient, although the wavelength dependence of the model is needed to be improved.

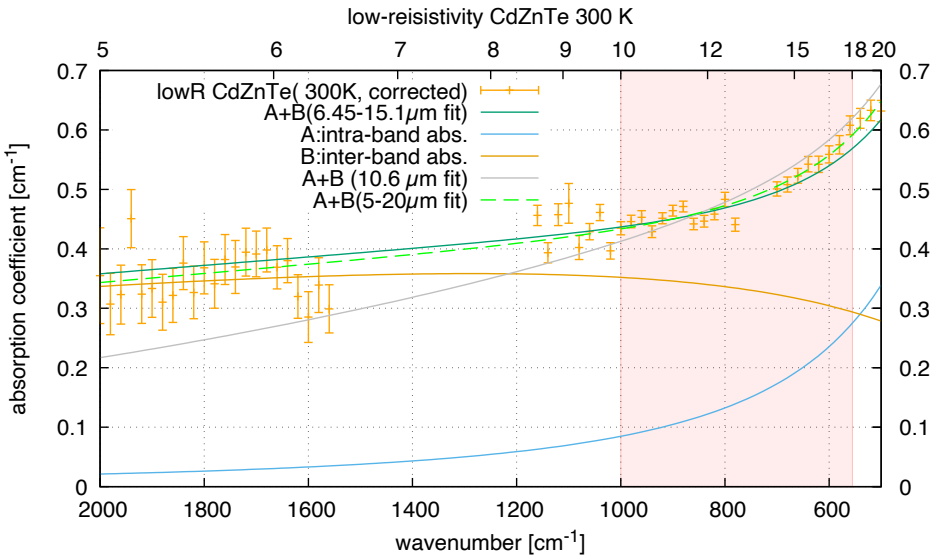

Figure. 5.9 Wavenumber dependence of the corrected α of low-resistivity CdZnTe (orange points) at 300 K and fitted curves. The dark green line shows the curve fitted at 6.45–15.1 μm. The dashed green line shows the curve fitted at 5–20 μm. The grey line shows the curve fitted at 10.6 μm (section 5.2.1).

Next, we discuss the corrected α at 8.5 K. The dominant absorption at 8.5K is (C) the absorption due to trapped-holes $\alpha_{\rm trapped}$. However, the wavenumber dependence of $\alpha_{\rm trapped}$ has not been studied. Then we assume that the wavenumber dependence of the absorption cross-section of the transition between the acceptor level and the light/heavy-hole valence subbands is the same that between acceptor level and split-off band, which is used as an approximated curve of the trapped-hole absorption due to transition from an acceptor level to light/heavy-hole band (Čápek et al. 1973). The absorption model and the cross-section at 8.5 K is expressed as

$$\alpha(\tilde{\nu}, T_c) = \sigma_{\rm trapped}(\tilde{\nu}) N_{\rm trapped}(T_c) \tag{5.37}$$

$$\sigma_{\rm trapped}(\tilde{\nu}) = c_0 \frac{\sqrt{\tilde{\nu} - E_a/hc}}{\tilde{\nu}(\tilde{\nu} - E_a/hc + c_1)^4} \tag{5.38}$$

$$T_c = 8.5 \text{ K}. \tag{5.39}$$

We set c_0 and c_1 as fitting parameters and fixed $E_a = 63$ meV, because $E_a(> 0)$ cannot be determined by the fitting with c_0, c_1 and E_a as free parameters.

Figure 5.10 shows the fitting result of wavenumber dependence of the corrected α of the low-resistivity CdZnTe at 8.5K. The fitted parameters are $c_0 = 0.6 \pm 0.3$ cm$^{-5/2}$ and $c_1 = (1.3 \pm 0.2) \times 10^3$ cm^{-1}, and reduced-$\chi^2 = 162$. The parameter c_0 is a proportional coefficient and c_1 determines the width of the asymmetric peak. The acceptor energy E_a determines the cut off wavelength $E_a/h\tilde{\nu} \sim 20$ μm. The trend of the model that the absorption coefficient increases at a longer wavelength is similar to the corrected absorption coefficient measured with the FTS at < 15 μm, although there are large differences of 0.1–0.6 cm^{-1} between the measured value and the model value at < 6 μm and at > 15 μm.

To summarize the discussions in sections 5.2.1 and 5.2.2, the temperature dependence of the α at four bandpass wavelength is well fitted by the model of free-carrier and trapped carrier absorption (section 5.2.1). This suggests the absorption in the low-resistivity CdZnTe is dominated by (A)(B) the absorption due to free-holes at 300 K and by (C) the absorption due to trapped-holes at $T < 50$ K. On the other hand, the wavenumber dependence should be improved (section 5.2.2.).

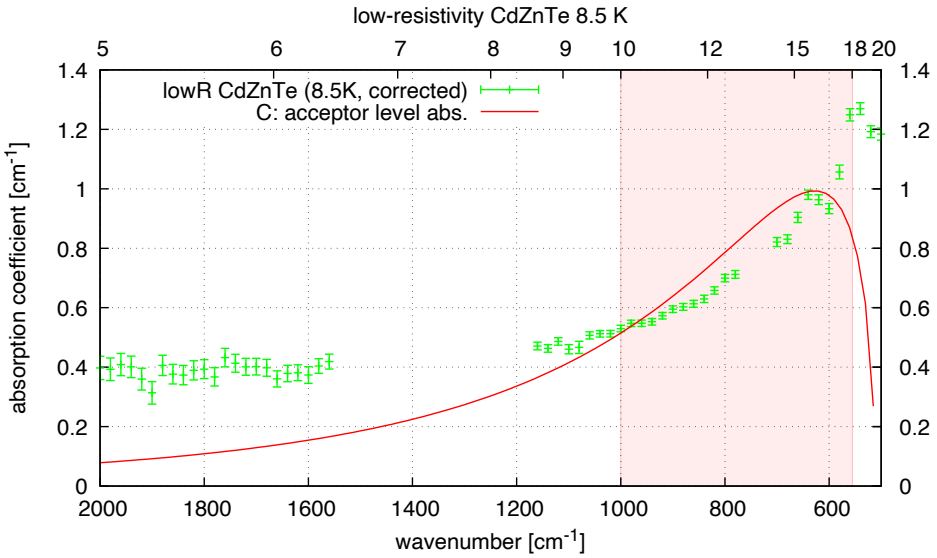

Figure. 5.10 Wavenumber dependence of the corrected α of the the low-resistivity CdZnTe at 8.5K (green points) and the fitted curve (red).

5.3 Applicability to an Immersion grating

In this section, we discuss the suitability of CdZnTe as a material for the 10–18 μm IG at 4.8 K. The absorption coefficient requirement as an IG material is $\alpha < 0.01$ cm^{-1}.

First, we discuss the suitability of the low-resistivity CdZnTe. The 10–18 μm absorption coefficient of the low-resistivity CdZnTe is larger than the required value at all measured temperatures (8.5–300 K). We assume that the α at 4.8 K is the same as that at 8.5 K, although we cannot measure the absorption coefficient α at the required temperature (4.8 K). This is because the temperature dependence of the measured absorption coefficient is negligibly small at < 50 K. Therefore, the low-resistivity CdZnTe is not suitable for the IG material even at cryogenic temperature.

Next, we discuss the suitability of the high-resistivity CdZnTe. The α of the high-resistivity CdZnTe is $\alpha < 0.11$ cm^{-1} at cryogenic temperature, but we cannot show that the α meets the requirement directly.

Here, we predict the requirement resistivity of CdZnTe at 300 K to meet the IG absorption coefficient requirement to determine whether the high-resistivity CdZnTe meets the requirement. At 10–18 μm, there are three possible absorption factors at cryogenic temperature: absorption due to trapped-carriers $\alpha_{\rm trapped}$, absorption due to lattice vibration $\alpha_{\rm lattice}$, and Rayleigh scattering due to < 2 μm-size Te precipitates $\alpha_{\rm Te}$ (see section 5.2.1).

First, we discuss the trapped-carrier absorption. Because carriers trapped in an impurity band at cryogenic temperature are released to the valence band or the conduction band at room temperature, cryogenic trapped-carrier density is roughly the same as the free-carrier density at room temperature. Also, the free-carrier density is inverse proportional to the resistivity ρ and the mobility μ:

$$N_{\rm free} = \frac{1}{q\rho\mu}, \tag{5.40}$$

where q is the charge of a single electron. Therefore, we derive the relation between the 8.5 K trapped-carrier absorption and the 300 K resistivity as follows:

$$\begin{aligned} \alpha_{\rm trapped}(8.5K) &= \sigma_{\rm trapped} N_{\rm trapped}(8.5K) \\ &\simeq \sigma_{\rm trapped} N_{\rm free}(300K) = \frac{\sigma_{\rm trapped}}{q\rho(300\ {\rm K})\mu(300\ {\rm K})}. \end{aligned} \tag{5.41}$$

Next, we discuss the Rayleigh scattering by < 2 μm-size Te precipitates. At room temperature, the 10–18 μm attenuation due to Rayleigh scattering by < 2 μm-size Te precipitates is evaluated by Sarugaku et al. (2017) and $\alpha_{\rm Te} \leq 10^{-3}$ cm^{-1}. As discussed in section 5.2.1, the attenuation due to Te scattering is $\leq 10^{-3}$ cm^{-1} even at cryogenic temperature due to its little temperature dependence.

Then, we discuss the lattice absorption. As discussed in section 5.2.1, lattice absorption is

expressed as

$$\alpha_{\rm lattice} = B_1 \exp(-B_2 \tilde{\nu}/\tilde{\nu}_0) \tag{5.42}$$

$$B_1 = 1.46 \times 10^5 \text{ cm}^{-1},\ B = 5.38,\ \tilde{\nu}_0 = 167 \text{ cm}^{-1}. \tag{5.43}$$

Since the lattice absorption with multi-phonon process decreases with temperature (Kudo 1996), we apply the $\alpha_{\rm lattice}$ at room temperature as the worst absorption case.

Considering the above three absorption factors, we expect that the absorption coefficient at 18 μm is the largest among 10–18 μm range. The resistivity dependence of absorption coefficient at 18 μm at 8.5 K is predicted as

$$\begin{aligned}\alpha_{\rm predict}(18\ \mu\text{m},\ 8.5\ \text{K}) &= \alpha_{\rm trapped} + \alpha_{\rm lattice} + \alpha_{\rm Te} \\ &= (120 \pm 50) \times \left(\frac{\rho}{\Omega\text{cm}}\right)^{-1} \left(\frac{\mu}{80\ \text{cm}^2/\text{Vsec}}\right)^{-1} + 0.0025\ \text{cm}^{-1}.\end{aligned} \tag{5.44}$$

Figure 5.11 shows the predicted resistivity dependence of the absorption coefficient. To meet the IG requirement ($\alpha < 0.01\text{cm}^{-1}$), the resistivity at 300 K should be $\rho \geq 3 \times 10^4$ Ωcm.

We compare the resistivity requirement and the high-resistivity CdZnTe. As described in section 2.3, the high-resistivity CdZnTe is n-type. We assume the electron mobility is the same as that of CdTe (700 cm^2/Vsec; Wakaki et al. 2007) and that the absorption cross-section of trapped electrons is the same order as that of (C) trapped-holes. Then the estimated absorption coefficient due to the trapped electrons of the high-resistivity CdZnTe is $\alpha_{\rm trapped} \lesssim 10^{-9}$ cm^{-1}, which is much lower than the required value. The total absorption coefficient of the high-resistivity at cryogenic temperature is estimated as $\alpha_{\rm predict}(18\ \mu\text{m}, 8.5\ \text{K}) \leq 0.0025$ cm^{-1}. Therefore, the high-resistivity CdZnTe is expected to meet the absorption coefficient requirement for IG at cryogenic temperature.

From the discussion in this section, we evaluate the suitability of CdZnTe for the cryogenic IG. The low-resistivity CdZnTe has large absorption coefficient ($\alpha > 0.4$ cm^{-1}) and does not meet the requirement ($\alpha < 0.01\text{cm}^{-1}$). We evaluate the room temperature resistivity requirement to meet the absorption coefficient at cryogenic temperature. From this evaluated the resistivity requirement, we suggest that the high-resistivity CdZnTe is a suitable material for the cryogenic IG.

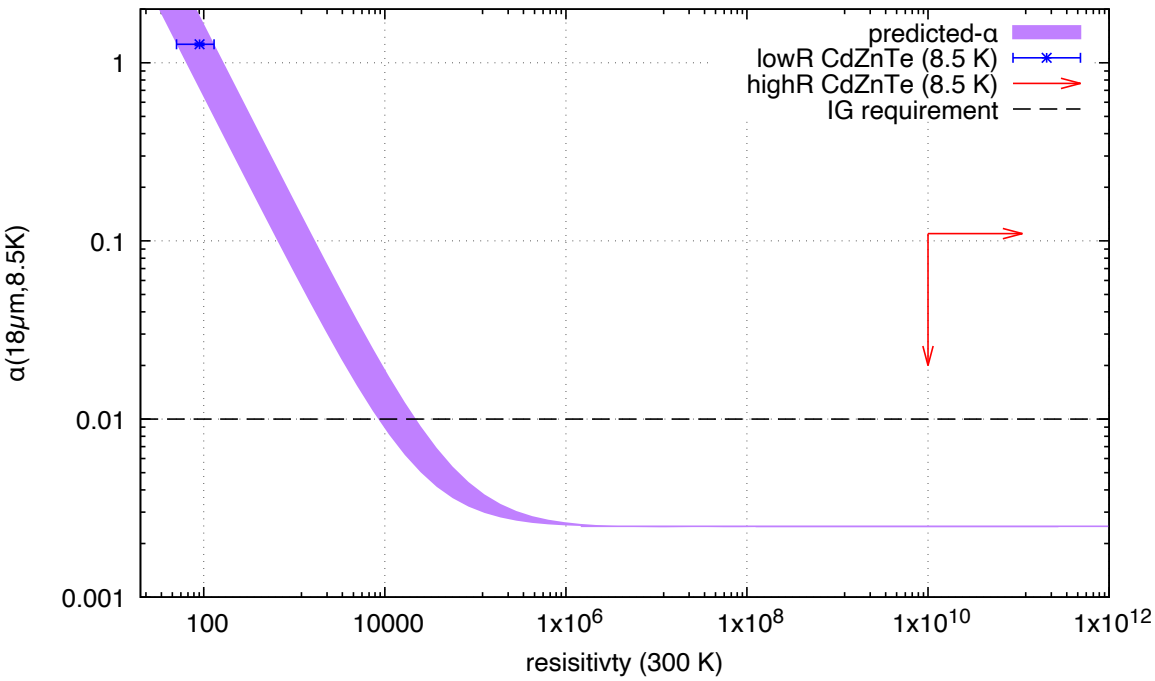

Figure. 5.11 Predicted resistivity dependence of absorption coefficient of CdZnTe at 8.5 K (purple). The blue dot and the red upper limit denote the measured absorption coefficient of the low and high-resistivity CdZnTe, respectively. The dashed line shows the IG requirement.

§6

Conclusion

In order to study the factors causing absorption in CdZnTe and to reveal if CdZnTe is suitable for the cryogenic IG, we measured the absorption coefficient of CdZnTe with different resistivity ($\sim 10^2, > 10^{10}$ Ωcm) at 5–20 μm at 8.5–300 K

To measure the absorption coefficient with high precision, we performed two experiments. One is the measurement of the transmittance of samples with (1) Fourier transform spectrometer (FTS) with an uncollimated beam. This measurement provides wavenumber dependence of absorption coefficient, although the measurement yields systematic uncertainty due to the defocus effect. To correct the defocus effect, we carried out other measurements; the transmittance measurement with (2) an originally developed collimated lamp beam system. This system provides absorption coefficient free from the defocus effect, although we can measure the transmittance at a limited set of wavelengths.

These two measurements show the following results:

- The samples were cooled down to $T = 8.5 \pm 0.5$ K and $T = 8.6 \pm 0.1$ K with the measurement systems of the experiment (1) and (2), respectively. The lowest temperature ($T = 8.5$ K) is lower than that of the high-precision FTS system developed by Kaji et al. 2016 (T =29 K). Our achieved temperature is low enough that the temperature dependence of the absorption coefficient becomes negligible, and the absorption coefficient at the required temperature (< 4.8 K) can be predicted reliably. This insensitivity of the absorption coefficient at the cryogenic temperature is more clearly demonstrated in this work by cooling samples down to $T = 8.5$ K compared to the cooling down to 29 K by Kaji et al. (2016).
- We measured the absorption coefficient with (1) an uncollimated FTS systems at 8.5 K and at 300 K. The measured 10–18 μm absorption coefficients of the low-resistivity CdZnTe is α =0.4–0.6 cm^{-1} at 300 K and become larger (α =0.5–1.4 cm^{-1}) at 8.5 K. On the other hand, the absorption coefficients of the high-resistivity CdZnTe ($\alpha < 0.1$ cm^{-1}) are lower than those of the low-resistivity one both at 300 K and at 8.5 K. The obtained statistical uncertainty of absorption coefficient ($\Delta\alpha < 0.02$ cm^{-1}) is small enough to discuss what causes absorption in CdZnTe. The obtained absorption coefficients include

systematic uncertainties due to the defocus effect.

- We measured the absorption coefficient with (2) an originally developed collimated beam system. The absorption coefficient of the low-resistivity CdZnTe is α =0.35–0.6 cm^{-1} at 300 K and becomes larger (α =0.4–0.9 cm^{-1}) at 8.6 K. On the other hand, the absorption coefficients of the high-resistivity CdZnTe ($\alpha < 0.11$ cm^{-1}) are lower than those of the low-resistivity at all measured temperatures (8.6–300 K). The obtained statistical uncertainty ($\Delta\alpha$ =0.016 cm^{-1}) is small enough to discuss absorption factors in CdZnTe.

By correcting the measurements of (1) with those of (2), we obtained the following results:

- We obtained the absorption coefficients of the low-resistivity CdZnTe without the defocus error at 8.5 K and at 300 K. The absorption coefficient at 10–18 μm is α = 0.4–0.6 cm^{-1} at 300 K and α = 0.5–1.3 cm^{-1} at 8.5 K. The absorption coefficient at 8.5 K is 1.2–2.2 times larger than that at 300 K. The absorption coefficient at 300 K in the current work is consistent with that by Sarugaku et al. (2017).
- We derived the upper limit of the 10–18 μm absorption coefficient of the high-resistivity CdZnTe as $\alpha < 0.11$ cm^{-1} at 300 K and $\alpha < 0.16$ cm^{-1} at 8.5 K. The obtained absorption coefficient at 300 K is consistent with that by Sarugaku et al. (2017) at 300 K.
- The achieved statistical uncertainty of the 10–18 μm absorption coefficient of the low-resistivity CdZnTe is $\Delta\alpha_{\rm corrected} = 0.01 - 0.02$ cm^{-1} and the systematic uncertainty is $\Delta\alpha_{\rm calc} = 0.03$ cm^{-1}. The uncertainty is improved from the uncertainty in the FTS measurements. (statistical uncertainty: $\Delta\alpha_{\rm stat} = 0.03$ cm^{-1} + uncertainty due to the defocus: $\Delta\alpha_{\rm def} \sim 0.06$ cm^{-1} + uncertainty due to calculation method: $\Delta\alpha_{\rm calc} = 0.03$ cm^{-1}). This uncertainty is small enough to discuss the absorption factors of CdZnTe, although the uncertainty is larger than the requirement ($\Delta\alpha_{\rm required} = 0.003$ cm^{-1}).

On the basis of the above results, we have the following discussions:

- Our results suggest that there are other absorption factors in addition to free carrier absorption in CdZnTe. We assume that the low-resistivity CdZnTe has three dominant absorption factors: (A) free hole absorption by inter-valence band transition, (B) free-hole absorption by intra-valence band transition, and (C) trapped-hole absorption by acceptor to valence band transition. Fitting the absorption coefficient at the four wavelengths in experiment 2 with the model, we obtain fitted parameters: acceptor band energy E_a = 63±1 meV, effective mass ratio of heavy and light-holes m_h/m_l =6–8, and acceptor density $N_A = (4.1 \pm 0.7) \times 10^{14}$ cm^{-1}. The E_a and m_h/m_l are consistent with those reported in previous studies of CdTe, and the N_A is consistent with the acceptor density independently derived from the resistivity. This result suggests that the dominant absorption in the low-resistivity CdZnTe is inter-valence band absorption at 300 K and absorption due to trapped-hole at $T < 50$ K. Also, the absorption factors are not unique to CdZnTe but can occur in semiconductors in general. Therefore, this model can be applied to the evaluation

of the cryogenic performance of other infrared semiconductor materials (e.g., other-type IG materials).

- The low-resistivity CdZnTe is not suitable as an IG material, since its absorption coefficient ($\alpha > 0.4$ cm^{-1}) is larger than the IG requirement ($\alpha < 0.01$ cm^{-1}) at any measured temperature.
- The absorption coefficient α of the high-resistivity CdZnTe is relatively low ($\alpha < 0.16$ cm^{-1}) and promising as a cryogenic IG material, although only the upper limit of the absorption coefficient is obtained directly. We estimate the required resistivity of CdZnTe at 300 K to meet the absorption requirement at 8.5 K. The trapped hole density at 8.5 K, which is the dominant absorption source at < 50 K, is roughly the same as the free hole density at 300 K. Also, free hole density is inverse proportional to resistivity. From the above relations, we estimate the resistivity requirement as $\rho \geq 3 \times 10^4$ Ωcm. The high-resistivity CdZnTe ($\rho > 10^{10}$ Ωcm) is expected to be suitable for the cryogenic IG material since it meets this resistivity requirement ($\rho \geq 3 \times 10^4$ Ωcm).

We reveal that the high-resistivity CdZnTe is suitable for the material of the cryogenic 10–18 μm IG. By developing the cryogenic IG with this material, high-resolution spectroscopic observation at 10–18 μm will be realized. This high-resolution spectroscopy will provide us valuable chemical and kinematical information on astronomical objects (e.g., snowlines).

Acknowledgments

My deepest appreciation goes to Prof. Takao Nakagawa, who provided helpful comments and suggestions. I would like to thank Associate Prof. Yasuhiro Hirahara and Kosei Matsumoto for their large contributions to the experiments and useful comments. SPICA is an international mission. I owe my gratitude to SPICA/SMI team for providing such a valuable opportunity and great support of this joint research. I am grateful to Uir-Lab members and Hirahara Lab members at Nagoya University for technical support with these experiments. I would also like to take this opportunity to thank members of the Laboratory of Infrared High-resolution spectroscopy (LIH) in Kyoto Sangyo University for technical support and valuable prior studies for the development of the IG. I thank Mr. Akira. Noda and Dr. Ryuichi. Hirano of JX Nippon Mining & Metals Corporation for valuable comments about the physical properties of CdZnTe. I also thank Prof. Itsuki Sakon for his support in Hall effect measurements at Cryogenic Research Center in the University of Tokyo. I appreciate the production of some parts of the measurement system and technical support by Instrument Development Center in Nagoya University and Advanced Machining Technology Group in ISAS. I am supported by ALPS (the Advanced Leading Graduate Course for Photon Science) of the University of Tokyo. My appreciation also goes out to my wife. Without her understanding and encouragement, it would be impossible for me to complete this thesis.

Finally, I would like to express my sincere gratitude to my parents, the members of the infrared group, and many other people who have supported my research life.

References

Ahmad, F. R. 2015, Appl. Phys Lett., 106, 012109

Archer, J., Doyle, D., Boyadjian, J., et al. 2020, Proc. SPIE., 11443, 1144327

Ashcroft, N. W., & Mermin, N. D. 1976, Solid State Physics, ed. D. G. Crane (Harcourt College Publishers)

Basu, P. K. 2003, in Theory of Optical Processes in Semiconductors (Oxford University Press), 583–605

Becker, U., Zimmermann, H., Rudolph, P., & Boyn, R. 1989, Phys. Stat. Sol. (a), 112, 569

Čápek, V., Zimmerman, K., Koňák, Č., Popova, M., & Polivka, P. 1973, Phys. Stat. Sol. (b), 56, 739

Cox, A. J., DeWeerd, A. J., & Linden, J. 2002, Am. J. Phys., 70, 620

DeBell, A. G., Dereniak, E. L., Harvey, J., et al. 1979, Appl. Opt., 18, 3114

Deutsch, T. F. 1975, J. Electron. Mater., 4, 663

Ebizuka, N., Morita, S.-y., Shimizu, T., et al. 2003, Proc. SPIE, 4842, 293

Gardner, J. P., Mather, J. C., Clampin, M., et al. 2006, Space Sci. Rev, 123, 485

Hayashi, C., Nakazawa, K., & Nakagawa, Y. 1985, in Protostars and Planets II, ed. D. Black & M. Matthews, 1100–1153

Hirahara, Y., Aoki, K., Ohta, K., et al. 2012, Proc. SPIE, 8446, 84463Y

Honda, M., Kudo, T., Takatsuki, S., et al. 2016, ApJ, 821, 2

Houck, J. R., Roellig, T. L., van Cleve, J., et al. 2004, ApJS, 154, 18

Ikeda, Y., Kobayashi, N., Sarugaku, Y., et al. 2015, Appl. Opt., 54, 5193

Kaji, S., Sarugaku, Y., Ikeda, Y., et al. 2014, Proc. SPIE, 9147, 914738

—. 2016, Proc. SPIE, 9912, 99125Z

Kaneda, H., Ishihara, D., Oyabu, S., et al. 2018, Proc. SPIE, 10698, 106980C

Kittel, C. 2005, Introduction to solid state physics (Kittel Kotai butsurigaku nyumon) (Maruzen)

Kudo, K. 1996, PhotoPhysical Basics (Hikari bussei kiso) (Ohmusha)

Lord, S. D. 1992, A New Software Tool for Computing Earth's Atmospheric Transmission of Near- and Far-Infrared Radiation, Tech. Rep. December

Marsh, J. P., Mar, D. J., & Jaffe, D. T. 2007, Appl. Opt., 46, 3400

Molva, E., Pautrat, J. L., Saminadayar, K., Milchberg, G., & Magnea, N. 1984, Phys. Rev. B, 30, 3344

Murakami, H., Baba, H., Barthel, P., et al. 2007, PASJ, 59, S369

Noda, A., Kurita, H., & Hirano, R. 2011, in Mercury Cadmium Telluride: Growth, Properties and Applications, ed. P. Capper & J. Garland (John Wiley & Sons, Ltd.), 21

Nomura, H., Wei, C.-E., Walsh, C., & Millar, T. J. 2019, in AAS/Division for Extreme Solar Systems Abstracts, Vol. 51, 324.12

Notsu, S., Nomura, H., Ishimoto, D., et al. 2016, ApJ, 827, 1

Pilbratt, G. L., Riedinger, J. R., Passvogel, T., et al. 2010, A&A, 518, L1

Quijada, M. A., & Henry, R. 2007, Proc.SPIE, 6692, 669206

Roelfsema, P. R., Shibai, H., Armus, L., et al. 2018, PASA, 35, 17

Roelfsema, P. R., Shibai, H., Kaneda, H., et al. 2020, Proc. SPIE, 11443, 1144325

Rothman, L. S., Gordon, I. E., Barbe, A., et al. 2009, JQSRA, 110, 533

Sarugaku, Y., Ikeda, Y., Kobayashi, N., et al. 2012, in Proc. SPIE, Vol. 8442, Proc. SPIE, 844257

Sarugaku, Y., Ikeda, Y., Kaji, S., et al. 2016, Proc. SPIE, 9906, 990637

Sarugaku, Y., Kaji, S., Ikeda, Y., et al. 2017, J. Electron. Mater., 46, 282

Sukegawa, T. 2018, JSIR, 27, 27

Sukegawa, T., & Okura, Y. 2017, Proc. SPIE., 10100, 101000M

Sukegawa, T., Suzuki, T., & Kitamura, T. 2016, Proc. SPIE., 9912, 99122V

van der Pauw, L. 1958, Philips Research Reports, 13, 1

Wada, T., Kaneda, H., Kokusho, T., et al. 2020, Proc. SPIE, 11443, 114436G

Wakaki, M., Takeshita, S., & Eikei, K. 2007, in Physical Properties and Data of Optical Materials, 1st edn. (CRC Press), 82

Young, E. T., Becklin, E. E., Marcum, P. M., et al. 2012, ApJ, 749, L17